

Host-Guest Chemistry of Cu²⁺/Histidine Complexes in Molecular Sieves

ISBN 90-393-3767-5

The cover picture shows the Bryce Canyon in Utah, USA. The picture was taken in 2003 and shows the results of the host-guest interaction between different kinds of rock (host), water (guest) and environmental parameters (pH, temperature).

Cover lay-out by Jan den Boesterd, AV-dienst, Faculteit Scheikunde, UU

Drukkerij Ponsen & Looijen, Wageningen

Host-Guest Chemistry of Cu²⁺/Histidine Complexes in Molecular Sieves

Gast-Gastheer Chemie van Cu²⁺/Histidine
Complexen in Moleculaire Zeven

(met een samenvatting in het Nederlands)

Proefschrift

ter verkrijging van de graad van doctor aan de Universiteit Utrecht op
gezag van de Rector Magnificus, Prof. Dr. W. H. Gispen, ingevolge het
besluit van het College voor Promoties in het openbaar te verdedigen op
maandag 30 mei 2005 des middags te 14:30 uur

door

Jan Gijsbert Mesu

Geboren op 23 mei 1975 te Spakenburg

Promotor: Prof. Dr. Ir. B.M. Weckhuysen
Department of Inorganic Chemistry and Catalysis, Debye
Institute, Utrecht University, Utrecht, The Netherlands

Co-promotor: Dr. T. Visser
Department of Inorganic Chemistry and Catalysis, Debye
Institute, Utrecht University, Utrecht, The Netherlands

The work described in this thesis was financially supported by NWO/CW - Van der Leeuw and by the National Research School Combination – Catalysis (NRSC-C).

Contents

Chapter 1:	General Introduction	1
Chapter 2:	Synchrotron Radiation Effects as Studied in a Combined UV-Vis/XAFS Setup	21
Chapter 3:	Infrared and Raman Spectroscopic Study of pH-induced Structural Changes of L-histidine in Aqueous Environment	41
Chapter 4:	Unravelling the Coordination Chemistry and Molecular Structure of Cu ²⁺ /Histidine Complexes in Aqueous Solution	67
Chapter 5:	On the Molecular Structure of Aqueous Cu ²⁺ /Histidine Complexes as Studied with XANES Spectroscopy	105
Chapter 6:	Host-Guest Chemistry of Zeolite-encaged Cu ²⁺ /Histidine Complexes	121
Chapter 7:	Summary and Concluding Remarks	145
	Samenvatting	151
	List of Publications	155
	Dankwoord	157
	Curriculum Vitae	161

Chapter 1

General Introduction

1.1 Introduction

Enzymes, metal complexes and solids are known to display intriguing catalytic activity, often with high (enantio-) selectivity and/or stability. However, the related fields of biocatalysis, homogeneous catalysis and heterogeneous catalysis, although heavily researched, have developed over the last century almost independently and most practitioners of these areas only occasionally interact and cooperate with each other. Nevertheless, much knowledge can be obtained from such cooperation simply because the basic principles of catalysis in these three areas are very similar. The specificity and high reactivity characteristics of enzymes and homogeneous catalysts make their comparison rather straightforward. This seems at first sight not to be the case for enzymes and solids, although the similarities, as will be discussed below, are at least as important as in the case of homogeneous catalysis and biocatalysis.

It should be obvious that the way of thinking developed in each of these fields of catalysis has the potential to impact the other fields to a large extent. Therefore it is not surprising that many efforts in the field of heterogeneous catalysis have been devoted to (1)

reduce the complexity of the surfaces of these materials in an attempt to create single-site heterogeneous catalysts and (2) to heterogenise homogeneous catalysts and enzymes in order to benefit from their advantages. In what follows, we will discuss in more detail various relationships between biocatalysis and heterogeneous catalysis, introduce some concepts of host-guest chemistry of transition metal ion complexes in zeolites and discuss the development of biomimetic materials with potential for catalysis based on known concepts from nature. In this respect, special emphasis will be placed on Cu-based enzymes, since these systems have inspired our research work to a large extent. The general introduction will end with a brief overview of the motivation, scope and outline of the research described in this thesis.

1.2 Relationships between biocatalysts and heterogeneous catalysts

The main similarities between enzymes and heterogeneous catalysts are related to (1) the concept of the active site, (2) the analogies between metal-protein and metal-support oxide interactions in a matrix, (3) the introduction of size and shape selectivity and (4) kinetics.¹

1.2.1 Active sites

The concept of active site is well accepted in the field of biocatalysis since it only represents a small portion of the large protein molecule, which is responsible for the activation of the substrate molecule. The active site may lie at or near the surface, but it may also be buried in a cavity that limits access of all but the desired substrate molecule.² In heterogeneous catalysis the term active site is used similarly and the density of active sites per unit of surface area of the catalyst material is an important characteristic of a catalytic solid.³ It is also the reason that people in this field strive to obtain materials with a high surface area as well as a high site dispersion in order to create a large number of active sites per gram of catalyst material. Although the surface area is relatively easy to measure, the determination of the number of active sites in a heterogeneous catalyst is far from trivial. It is possible for acid catalysts, but often problematic for redox and metal catalysts. Therefore, although both fields

make use of the concept of turnover number (TON), defined as the number of substrate molecules converted per time unit per active site, only in the field of biocatalysis one can be sure that TONs can be determined with rather high precision.

1.2.2 Catalyst matrix

Both for heterogeneous catalysts and biocatalysts the active site is located in a matrix that is not an integral part of the active site. Solid catalysts convert substrate molecules, which are present in the gas or solution phase and should be first adsorbed before the reaction can take place. In a very similar manner specific substrate molecules are trapped near the active site in enzymes, according to a key-lock principle. In this respect, it is important to stress that the term substrate in the field of heterogeneous catalysis is often used to describe the support onto which the catalyst is mounted. The analog of the enzymatic substrate for scientists working in the field of heterogeneous catalysis is the feed or reactant molecule. This is illustrated in Figure 1.

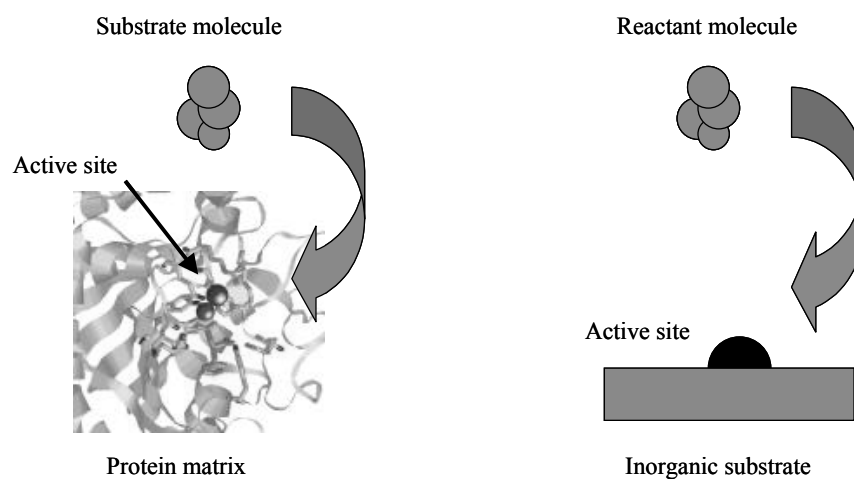


Figure 1. Structural resemblance between the protein matrix (left) and an inorganic substrate (right), carrying the active site. The first one is converting a substrate molecule and the second one a reactant molecule into the desired reaction product.

Although metals and bulk oxides are in use in many important industrial processes, most modern heterogeneous catalysts are supported systems in which the catalytically active

component is diluted by a material that prevents the active sites from agglomeration or deactivation. In the classical view, protection of the active site is the main function of the support oxide, but there is currently sufficient experimental evidence to state that the support oxide often has also a more active role in a catalytic process. Indeed, it has been shown for many reactions that the catalytic activity is a function of the properties of the support oxide. As an example, one can refer to the work of Wachs *et al.*, which shows that the TON for the selective oxidation of methanol to formaldehyde over supported vanadium oxide catalysts can be altered by a factor of 3 simply by changing the type of support oxide, while keeping the molecular structure of the active site almost unaltered.^{4, 5} Moreover, the phenomenon of strong metal-support interaction has been shown to have a profound effect on the reactivity and chemical nature of certain reactive metal sites.⁶ This is especially true for titania-supported metal catalysts, as is the case for certain Fischer-Tropsch catalysts.

In redox enzymes scientists view the protein matrix in an analogous manner, in the sense that it is responsible for the isolation of the metal ions in order to prevent aggregation and deactivation. However, as in the case of heterogeneous catalysis, the protein often plays a very specific role as an acid, base, ligand or nucleophilic species. Furthermore, there is now a general consensus that the protein residues in the vicinity of the active site are influencing the catalytic properties of the metal center to a large extent. Thus, the matrix that binds the active site has a profound influence on the overall catalytic performances of both supported metal (oxide) catalysts and metallo-enzymes.

1.2.3 Size and shape selectivity

Another function of the matrix is to introduce size and shape selectivity in the catalytic processes. Enzymes are known for their excellent shape selectivity and regio- and stereoselectivity with respect to their substrates. For example, different versions of the cytochrome P-450 enzyme family catalyze the hydroxylation of substrates ranging from vitamin D to naphthylamine.⁷ A similar example of the introduction of shape selectivity in the field of heterogeneous catalysis is the use of zeolites, which by means of their structure and porous nature allow access of only those molecules, which are not exceeding the size and shape of the zeolite pore system. Thus, the size and shape selectivity of both zeolites and enzymes

derives from a structure in the catalyst material that is complementary to that of the substrate/reactant, the transition state and/or the product formed. A major difference, however, is the degree of rigidity, with the enzyme being far more flexible and more dynamic during the course of the catalytic reaction than the zeolite material.

1.2.4 Kinetics

Michaelis and Menten were the first to establish the concept of enzyme kinetics and the simplest interpretation of the equation involves the saturation of the active sites with the substrate, which makes the Michaelis constant K_m an effective dissociation constant.⁸ The smaller K_m , the larger the affinity of the substrate for the enzyme. This famous Michaelis-Menten equation is, however, very similar to the one used to describe the kinetics of a reaction of a single reactant in a heterogeneous catalytic process, as described by Langmuir and Hinshelwood.⁹ Both heterogeneous and biocatalysis involve the adsorption of a reactant to achieve saturation of the limited number of available active sites and the adsorption isotherm of a heterogeneously catalyzed reaction is analogous to the substrate binding curve for an enzymatic catalyzed reaction.¹⁰

1.3 Host-Guest chemistry of transition metal ion complexes in zeolites

1.3.1 Transition metal ion complexes

A transition metal ion (TMI) complex (also called a coordination compound) is a compound in which a TMI is surrounded by one or more coordinating molecules.¹¹ The transition metal elements comprise groups 3 to 12 in the periodic table. They are called transition elements because their position in the periodic table is 'transitional' between the metallic elements of groups 1 and 2 and the predominantly non-metallic elements of the groups 13-18.¹² The coordinating molecules in the TMI complexes are called ligands. The ligands are coordinating directly to the TMI *via* one or more donor atom within the ligand

molecule. The bond between the TMI and the ligand is called a coordination bond, rather than an ionic or a covalent bond.

The TMI complexes are characterized by a variable oxidation state. The oxidation state of a TMI depends on the filling of the TMI d-orbitals.^{13, 14} Depending on the TMI, some oxidation states occur more often than others and these oxidation states readily interconvert. The TMI complexes are very well-known for their colors and can be regarded as chameleon elements. This has to do with electronic transitions in the d-orbitals of the TMI, since the energy separation between the different d-orbitals is in the energy range of visible light. Depending on the oxidation state of the TMI in a complex, one or more unpaired electrons may be present. Nevertheless, these complexes can be described as paramagnetic ions rather than radicals and can be detected by techniques such as electron spin resonance (ESR) spectroscopy. In contrast to the very high reactivity of organic radicals, the TMI complexes with unpaired electrons are quite stable. The long-term stability of coordination compounds with unpaired electrons is another characteristic of TMI complexes.

All these properties make that TMI complexes have been selected by nature to be part of a variety of redox enzymes and transport proteins present in *e.g.* plants, animals and humans. In other words, they are essential to life. Furthermore, TMI complexes can be used for a lot of different industrial applications. For example, TMIs can often be found as the active center in homogeneous and heterogeneous catalysts. One can alter the catalytic properties by changing the type of transition metal ion, the properties of the ligand and by adjusting the environment around the TMI complex. This offers tremendous opportunities for the deliberate design of novel catalytic systems. One way to do this is by immobilizing a specific TMI complex, a guest molecule, in the matrix of inorganic hosts, such as zeolites. As a consequence, a functional host-guest molecular system can be created. It should already be clear to the reader that the host matrix will alter the properties of the guest, but also *vice versa* will the host matrix be influenced by the introduction of the guest molecule.

1.3.2 Zeolites

Zeolites are an important class of crystalline materials that have widespread applications as catalysts, absorbents and ion exchange materials.¹⁵ Nowadays, 161 different

kinds of zeotype frameworks have been reported in the Atlas of Zeolite Framework Types, as issued by the International Zeolite Association (IZA).¹⁶ Except for the traditional aluminosilicate zeolites, many other systems, such as metallosilicates, metallogermanates and metallophosphates are included. As a consequence, the framework elements of the more classical zeolites have been extended to most of the transition metal and main group elements.

The traditional aluminosilicate zeolites are microporous and the framework structure consists of lattice cations (T), which are tetrahedrally coordinated to four oxygen anions (TO₄) and each oxygen anion shares two lattice cations. The TO₄-tetrahedra can be linked in many ways, giving rise to different zeolite structures, with a wide variety of pore and channel systems and properties. The presence of pores of molecular dimensions has led to the alternative name of molecular sieves for zeolitic materials. It is this property, which has given zeolite materials their wide applications in shape selective catalysis and nowadays acidic zeolites comprise the heart of the crude oil cracking units in petrochemical industry.

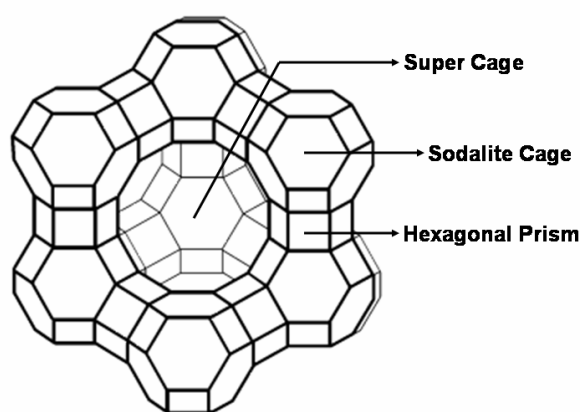


Figure 2. Schematic overview of the structure of zeolite Y. The lines represent oxygen atoms that connect the tetrahedral cation sites in the zeolite structure.

The charge of the zeolite lattice is neutral when the T site is occupied by a four-valent cation, usually a Si⁴⁺ cation. Isomorphous substitution of Si⁴⁺ by a trivalent Al³⁺ cation results in a negative lattice charge. This negative charge is compensated by the presence of cations, such as for instance Na⁺, in the micropores of the zeolite. It is important to stress that these extra-framework cations are not an integral part of the zeolite material. In hydrated zeolites the extra-framework cations are relatively mobile and can be replaced by other cations, using ion exchange procedures. In this way transition metal ions, such as Cu²⁺ and Fe^{2+/3+}, can be

introduced into the zeolite matrix. If an H^+ is exchanged into the material (*via* NH_4^+ and subsequent calcinations), the material will obtain acidity and the corresponding sites are called Brønsted acid sites.

The zeolite that is used in this thesis is zeolite Y. It exhibits the faujasite structure with the IZA-code FAU. It usually possesses a Si/Al ratio of about 2.5 and has a three-dimensional micropore system, built up from sodalite cages that are connected *via* hexagonal prisms (Figure 2). Supercages characterize the pore structure and are approximately 13 Å in diameter. They are interconnected *via* 12-membered rings with a diameter of 7.4 Å.

1.3.3 Transition metal ion complexes in zeolites

Several synthesis routes have been devised to synthesize zeolite-immobilized TMI complexes and Figure 3 summarizes the different strategies reported in literature.¹⁷ Two main routes can be followed: (1) synthesis starting from a preformed TMI complex and (2) assembly of the TMI complex inside the zeolite. The choice of the route depends on the zeolite type, the TMI and on the ligands forming the TMI complex.

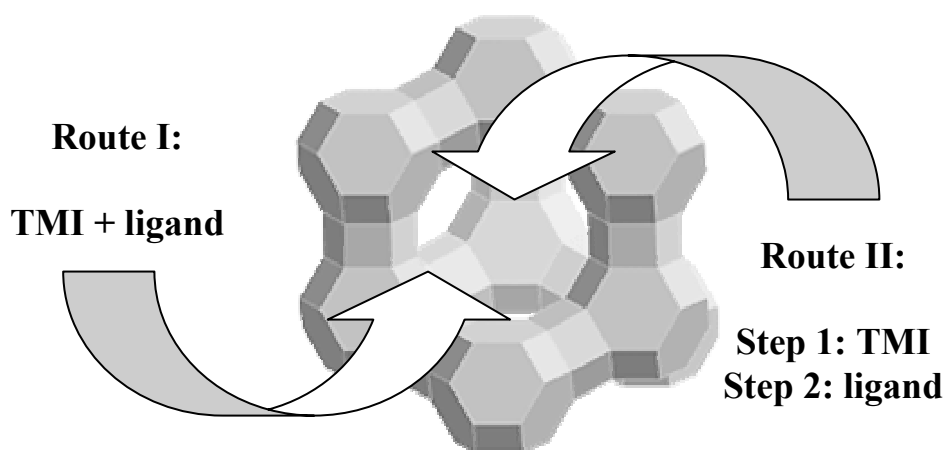


Figure 3. Overview of the synthesis routes for immobilizing transition metal ion complexes in zeolites.

Since TMI complexes often have a positive charge, the ion exchange method is the most straightforward strategy making use of preformed TMI complexes. The effectiveness of this method depends on the resistance of the zeolite against acid or base present in the ion

exchange solution and on the dimensions of the rings of oxygen atoms defining the zeolite windows and channels. Therefore, this method is only applicable if: (a) the TMI complexes are stable, (b) the ion exchange solutions containing the TMI complexes have no extreme pH values and (c) the TMI complexes are small enough to enter the zeolite. Thus, only (octahedral) complexes with flexible ligands, such as H_2O , NH_3 and some aliphatic amines, may be exchanged into zeolite Y without steric limitation, while for acidic ion exchange solutions the contact time must be short to avoid zeolite lattice destruction.

Once the TMI complex is introduced in the zeolite *via* ion exchange, the zeolite matrix itself may start to coordinate to the TMI, thus influencing the properties of the immobilized TMI complex. So in that way the zeolite becomes a uni-dentate and sometimes even a multi-dentate ligand, which is in competition with the extra-lattice ligands for complexation with the TMI. This may lead, depending on the relative coordination strength of the zeolite oxygens and the extra-lattice ligands, to the synthesis of unusual TMI complexes, giving rise to special catalytic properties.

TMI complexes unable to undergo ion exchange conditions, can be synthesized *via* direct assembly within the zeolite matrix. This method usually starts with ion exchange of the zeolite material with the desired TMI. The procedure is then continued with the introduction of the ligand. This can be done either with or without a solvent. A condition for TMI complex formation within the zeolite cages or channels is that the complexation constant of the TMI with the zeolite lattice oxygen atoms is lower than that with the added ligand.

An advantage of the immobilization of TMI complexes in the pore system of the zeolite is that the micropores and the cages of the zeolite structures have molecular dimensions. This makes that the pore geometry of the zeolite induces shape selectivity in catalytic reactions and allows for intra-particle transport of reactants and products. This property makes that only certain molecules are allowed to react with the TMI complex, whereas the approach of other molecules is prevented. This shape selectivity of course also holds for the size and shape of the complexes, which can be synthesized within the cages and channels of the zeolite material. Finally, zeolite-occluded TMI complexes have strongly reduced mobility with respect to their solution mobility and deactivation as a result of aggregation can be largely avoided. Due to the excellent chemical, mechanical and thermal

stability of zeolites as host materials, the obtained host-guest system may possess superior catalytic properties compared to its homogeneous counterpart.¹⁸

1.4 Biomimetic materials

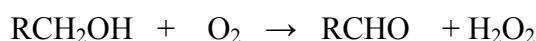
One of the key properties of biological systems is their ability to change important properties in response to their environment. The molecular mechanisms that biological molecules utilize to sense and respond provide interesting paradigms for the development of bio-inspired materials that display “smart” properties.¹⁹ There are numerous technologies in which responsive material properties have proved useful applications or have important potential for implementation. Examples of areas of interest are the controlled release and delivery of drugs, the engineering of tissue, diagnostics, affinity separations, sensing elements and catalysis.

Biomimetic materials science has evolved significantly since its birth about three decades ago and it would be impossible to discuss this field in great detail. In what follows, we will limit ourselves to a discussion of a biological system, which has inspired the work described in this thesis. Since our work aims to construct and characterize a structural mimic of galactose oxidase making use of zeolites as host materials, we will discuss the main characteristics of this enzyme known until now. In addition, we will summarize the existing literature on zeolite-based galactose oxidase mimics.

1.4.1 Galactose oxidase

The copper enzyme galactose oxidase (GOase), which is an extracellular enzyme produced by fungi of the *Fusarium* genera, has been the subject of intense research interest due to its intriguing structure and reactivity.²⁰ GOase is a single polypeptide chain of 639 amino acids, whose structure has been determined to 1.7 Å resolution for GOase isolated from *Fusarium*.^{21, 22} A similar structure has also been obtained for *Aspergillus nidulans* with a resolution of 2.0 Å.²³ GOase is a mononuclear type 2 Cu-containing enzyme that catalyzes the oxidation of primary alcohols to their corresponding aldehydes. The enzyme has a wide range of substrates, but is strictly stereo-specific.²⁴ More specifically, it was found that D-galactose

is a good substrate molecule, whereas GOase shows no activity with L-galactose or D-glucose. The two-electron oxidation of the primary alcohol molecule to its corresponding aldehyde is coupled with the reduction of dioxygen to hydrogen peroxide and can be written as follows:



However, this two-electron process requires, besides the Cu site, a second redox-active center, which is provided by a radical situated at a tyrosine (Tyr) residue. All this became clear after the crystal structure of the mature enzyme was discovered in 1991. Crystallography revealed that Cu has an NNOO coordination in the equatorial plane and coordinates to two N^r atoms from the imidazole rings of two different histidine (His) residues, whereas one exogenous ligand and two Tyr residues complete the approximately square pyramidal geometry around Cu. A schematic representation of the structure of GOase is shown in Figure 4. The equatorially coordinating Tyr is covalently linked to a neighbouring cysteine (Cys) by a C-S bond at the position *ortho* to the hydroxyl group. GOase is an unusual enzyme since the number of metal ions present in the active site does not match the number of electrons transferred for catalyzing the chemical reaction and it has been found that the Tyr free radical participates in the redox chemistry as an additional redox site. Due to this behaviour Cu does not have to attain a Cu(III) oxidation state during catalysis. The radical is located on the equatorial cysteine-substituted Tyr.

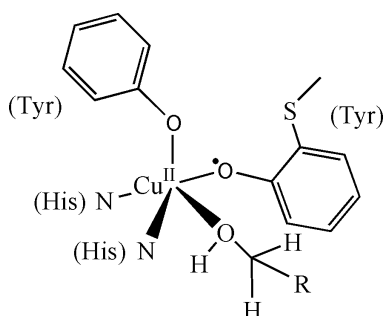


Figure 4. Active site of the enzyme Galactose Oxidase.

The X-ray crystal structure of GOase has been confirmed making use of Raman²⁵ and ESR/Electron-Nuclear Double Resonance (ENDOR) spectroscopy.²⁶ Other elegant

spectroscopic work, in particular done by the group of Whittaker,^{27, 28} indicates that there is a change in the geometry of the active site between the resting (inactive) form and the oxidatively activated form, although the Extended X-ray Absorption Fine Structure (EXAFS) spectra of both states are virtually identical, indicating that there is no change in copper-to-ligand distances.²⁹ The proposed catalytic mechanism for GOase is shown in Figure 5.³⁰ After the substrate molecule binds to the equatorial Cu position (occupied by water or acetate in the crystal structures, the latter because the cultures were grown in an acetate buffer at a pH of 4.5), the first step is a proton transfer from the alcohol to the axial tyrosinate (Tyr₄₉₅). Next, a hydrogen atom is transferred from the substrate to the modified Tyr radical. The resulting substrate-derived ketyl radical is then oxidized *via* electron transfer to the Cu center, yielding Cu(I) and the aldehyde product. The two latter steps have been suggested to occur simultaneously in a concerted manner. The Cu(I) and the Tyr are in the last step re-oxidized by O₂, regenerating Cu(II) and tyrosyl and yielding H₂O₂ as reaction product. This mechanism has been studied in more detail using DFT calculations. For this purpose, the two His ligands were modelled using imidazoles, the equatorial Tyr using SH-substituted phenol, whereas the somewhat smaller, but fully adequate, vinyl alcohol served as a model for the axial Tyr. Methanol was used as a substrate. It was found that the first step, proton transfer from the substrate to Tyr₄₉₅, occurs with a very low barrier (less than 3 kcal/mol). The exothermicity was calculated to be 3.2 kcal/mol.

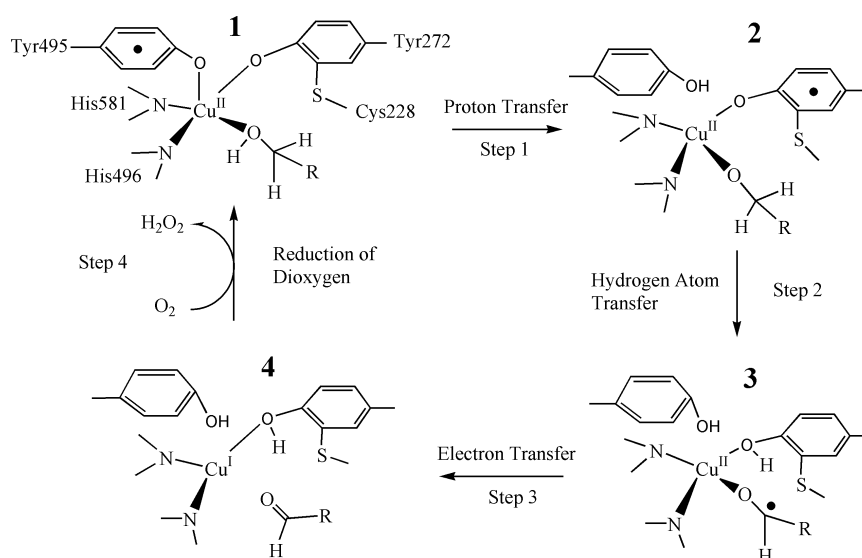


Figure 5. Proposed catalytic mechanism for the enzyme galactose oxidase.

An important result from the calculations was that the radical site, prior to the proton transfer step, is not the equatorial cysteine-substituted Tyr residue, but rather the axial Tyr. The axial position is the weakest one in the square pyramidal coordination of Cu and thus the most natural place for the radical to be in. This finding was contrary to the commonly accepted working mechanism of the enzyme, but not in conflict with any experiment. In fact, model complex experiments show that the radical is most likely located axially in a non-square planar coordination of Cu. After proton transfer the radical is located at the equatorial Tyr, implying that, simultaneously with the proton transfer, an electron is moved from the equatorial Tyr to the axial one.

The second step in the proposed mechanism of GOase is a hydrogen atom transfer from the substrate to the Tyr₂₇₂ radical. The barrier was calculated to be 13.6 kcal/mol, which compares well with the known TON of the enzyme. Hence, the calculations give very strong support to the proposed mechanism. The hydrogen atom transfer is proposed to result in a substrate-derived ketyl radical, which then would be oxidized *via* electron transfer to the Cu center, yielding Cu(I) and the aldehyde product. This proposed radical intermediate was located at an energy 4.9 kcal/mol lower than the transition state, making the hydrogen atom transfer step endothermic by 8.7 kcal/mol. The intermediate is very unstable, with the barrier for its collapse to a closed shell Cu(I) species and aldehyde product being very small. In practice, this radical intermediate is therefore probably impossible to detect. The ketyl radical intermediate will readily reduce the copper center, yielding Cu(I) and aldehyde. The electron transfer step was estimated from the calculations to be exothermic by *ca.* 5 kcal/mol. Energy is gained by the binding and one-electron reduction of O₂.

1.4.2 Zeolite-based structural mimics of galactose oxidase

Nature has always been an inspiration source for mankind. This holds equally well for catalyst scientists, who dream of designing a material that catalyzes reactions with the elegance of enzymes; *i.e.* operating at ambient conditions (room temperature and low pressure) and catalyzing in an enantio-selective manner a complex series of reactions without the formation of hazardous by-products. One potential way to achieve this ambitious goal is by building a synthetic analogue of the active site of an enzyme within a robust matrix, in that

way creating a kind of enzyme mimic. The advantage of the robust matrix is that enzymes are sometimes too fragile for industrial uses, where extreme conditions can make their protein framework to collapse.

An example of such an approach has been found to be successful for GOase. Weckhuysen *et al.* have immobilized Cu-His complexes in the supercages of zeolite Y *via* an ion exchange procedure of pre-formed Cu-His complexes in aqueous solutions.³¹ The aim was to construct a structural mimic of GOase by designing a similar first coordination sphere around Cu, with the zeolite matrix replacing the protein mantle of GOase. Admission of NH₃ to the zeolite materials led to a distortion of the occluded Cu-His complex and vacuum treatment regenerated the free coordination site in the engaged complex. The presence of such a coordination site gives catalytic potential to these materials and it was indeed found that Cu-His/Y materials showed promising catalytic activity for the epoxidation of alkenes (*e.g.* cyclohexene) and the oxidation of primary alcohols, such as pentanol and benzylalcohol, in the presence of *tert*-butyl hydroperoxide at 60°C. An overview of the catalytic performances of zeolite-engaged Cu(amino acid) complexes is given in Table 1. Unfortunately, no catalytic activity was found when O₂ was added as the oxidant. Furthermore, the catalyst material was not very active in the oxidation of cyclohexane.

Table 1. Catalytic performances of zeolite-engaged and clay-intercalated Cu(amino acid) complexes. The reactions have been performed at 60°C making use of *t*-butylhydroperoxide as oxidant.^{31, 33, 34}

Catalyst	Substrate	Products	Time (h)	Conversion (TON)
Cu-His/Y	1-Pentanol	Pentanoic acid	24	1425
	Benzylalcohol	Benzoic acid; benzaldehyde	24	2421
	Cyclohexene	Cyclohexeneoxide; cyclohexanediol; cyclohex-2-ene-1-ol; cyclohex-2-ene-1-one	24	3230
	Cyclohexane	Cyclohexanol; cyclohexanone	24	450
Cu-His/saponite	1-Pentanol	Pentanoic acid	24	243
	Benzylalcohol	Benzoic acid; benzaldehyde	24	302
	Cyclohexene	Cyclohexeneoxide; cyclohexanediol; cyclohex-2-ene-1-ol; cyclohex-2-en-1-one	24	1008
Cu-Lys/Y	Cyclohexene	Cyclohexeneoxide; cyclohexanediol; cyclohex-2-ene-1-ol; cyclohex-2-en-1-one	24	735
Cu-Arg/Y	Cyclohexene	Cyclohexeneoxide; cyclohexanediol; cyclohex-2-en-1-ol; cyclohex-2-en-1-one	24	669

Another important observation was that the activity was dependent on the Cu loading of the zeolite material; highly loaded Cu-His zeolite Y materials were clearly less active than

low loaded Cu-His systems.³³ Furthermore, Cu-His zeolite Y catalysts were superior in catalytic performances compared to Cu-lysine(Lys)/Y and Cu-arginine(Arg)/Y materials for the same type of chemical reactions and tested under identical conditions (Table 1). In addition, zeolite materials first loaded with Cu and later on ion exchanged with His or other amino acids, including proline (Pro), Lys and Arg, gave rise to inferior catalytic materials due to the presence of uncomplexed Cu. In the case of Cu-His, a pH of 7.3 and for Cu-Arg and Cu-Lys complexes, a pH of 10 of the ion exchange solutions was optimal for immobilizing the Cu complexes in the supercages of the zeolite matrix. Clearly, it was found that the preparation method and catalyst composition are crucial for obtaining excellent catalytic performances.

In a continuation of this work, Fu *et al.* have immobilized Cu-His and Cu-Lys complexes between the layers of saponite clays.³⁴ The intercalated complexes were again accessible to NH₃, turning the Cu complexes into a distorted octahedral coordination and suggesting the presence of a free coordination site available for catalysis. Accordingly, the obtained materials are active in the oxidation of pentanol, benzylalcohol and cyclohexene at low temperature with peroxides as oxidants. However, their activity is always much lower than for zeolite-occluded complexes (Table 1) and this lower activity was explained in part by a limited accessibility and by swelling of the clay minerals by the reaction products formed.

In order to be able to develop structure-activity relationships for these catalyst materials, the immobilized Cu-His complexes have been characterized by different characterization techniques, including UV/Vis, X- and Q-band ESR and pulsed ESR spectroscopies, more specifically Electron Spin Echo Envelop Modulation (ESEEM) and high-field (W-band) pulsed ENDOR. Based on a detailed ESR investigation of the above mentioned catalyst systems it was concluded that two different Cu-His complexes, labeled as species A and B, are present within the zeolite material, the relative amount of these two complexes being dependent on the experimental conditions used during the ion exchange procedure. The higher the Cu-His loading in the zeolite matrix, the higher the relative amount of complex B in the zeolite. The catalytic activity of the material increases in the opposite direction. Besides that, X-band ESR also provided information on the molecular structure of complex B, since in the spectrum of the sample with the highest relative amount of complex B a 7-line ¹⁴N (I = 1) superhyperfine splitting pattern was present. This indicates the presence of

three N atoms coordinating to Cu. The fact that more N atoms are coordinating to Cu in complex B is also supported by UV/Vis measurements, as the maximum of the d-d transition of Cu is shifting to higher energy for systems with a higher relative amount of complex B. This is indicative for a higher ligand field splitting for complex B with respect to complex A. Table 2 summarizes the UV/Vis and ESR parameters for Cu-His complexes ion exchanged in the supercages of zeolite Y. For reference purposes the spectroscopic fingerprints of clay-intercalated Cu-His complexes and ion exchanged Cu/zeolite Y and Cu/saponite materials are also included.

Table 2. ESR and UV/Vis parameters of Cu-His complexes occluded in zeolite Y, together with some reference compounds.^{31, 33, 34}

Material	Species	UV-Vis (cm ⁻¹)	g//	A//	SHFS	A _{L,N} (number of lines)
Cu-His/Y	A	15200	2.31	158	No	-
	B	15600	2.25	183	Yes	13 (7)
Cu-His/saponite	C	16700	2.23	192	No	-
Cu/Y	D	12500	2.40	134	No	-
Cu/saponite	D'	13100	2.34	138	No	-

More detailed information about species A was obtained with ESEEM. This technique showed that only complex A exhibits an intense ²⁷Al modulation, which indicates that complex A (I_{Cu} = 3/2) binds to the zeolite framework, giving rise to a magnetic interaction with the Al (I = 5/2) of the structure.³⁵ The technique also provides proof for the coordination of the imidazole N in both complexes A and B, via the ESEEM frequencies of the remote N. Recently, advanced pulsed EPR and ENDOR techniques were used to check whether the carboxyl groups of the His ligands are participating in coordination to Cu in the equatorial plane, or not. It was indeed found that complex A possesses a carboxylate group in an equatorial position to Cu.³⁶

Summarizing, based on the outcome of the-above mentioned characterization techniques, the molecular structures shown in Figure 6 are proposed for complexes A and B. Complex A is a bis-His complex, in which the amino and imidazole nitrogen of one His ligand are coordinating in the equatorial plane to Cu, in combination with a carboxyl oxygen of a second His and an oxygen from the zeolite framework. In other words, this complex has an NNOO coordination environment, very similar to the one of GOase. Instead, complex B is

a bis-His complex, which is situated in the supercage of the zeolite Y structure with all the equatorial coordination sites of Cu occupied by functional groups of His, *viz.* the amino and the imidazole groups of one His ligand, together with the imidazole and carboxyl groups of a second His ligand.

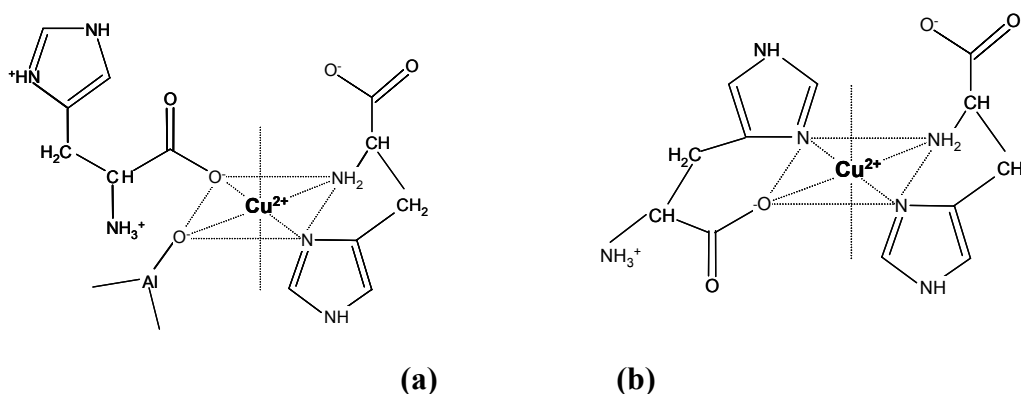


Figure 6. Molecular structure of complex A (a) and complex B (b) occluded in the supercages of zeolite Y.

1.5 Motivation, scope and outline of thesis

The goal of this study is to elucidate the molecular structure of the Cu-His complexes that have been occluded in zeolite Y *via* an ion exchange procedure with an aqueous solution of the complex. More specifically, we aim to describe in a rigorous manner the host-guest chemistry in zeolites and make the comparison with enzymatic systems. For this purpose, the influence of the zeolite matrix on the coordination chemistry of the introduced Cu-His complex should be explored. This will be achieved in a three-pronged approach making use of a multitude of spectroscopic techniques. As the properties of the ligand in the TMI complexes are very important, the molecular structure of His as function of the solution pH is studied in great detail as a first step. In a second step the focus is on the determination of the molecular structure of Cu-His complexes in the ion exchange solution as a function of a wide pH range. With this knowledge it is possible to fingerprint the coordination geometry of Cu-His complexes in the pore system of zeolite Y.

In chapter 2 one of the advantages of the multi-technique approach is illustrated. A Cu complex catalyzed oxidation reaction was studied in a combined *in-situ* UV/Vis-ED-XAS setup. The analysis of the UV/Vis results provided evidence for a reducing influence on the

sample of the X-rays used for the collection of the X-ray absorption data. Differences were observed between different synchrotron radiation sources as well as between Cu-containing solutions possessing different types of counter anions. The study gives valuable information on the conditions in which Cu complexes are reduced under influence of the X-ray beam and what other parameters are important for beam damage to occur. It will be shown in the following chapters that similar effects may also occur for Cu-His complexes both in aqueous solutions and in the supercages of zeolite Y.

The quest for the molecular structure of the zeolite-occluded Cu-His complex starts in chapter 3 with a spectroscopic study of pH-induced structural changes of the His ligand, making use of IR and Raman spectroscopy. The information obtained in this chapter is important for the next step, which is discussed in Chapter 4. In this chapter a combined IR, Raman, UV/Vis, EPR and EXAFS study on the pH-induced structural changes of the Cu-His complex in aqueous solutions is presented. Based on the outcomes of chapter 4, chapter 5 elaborates on the molecular structure of the Cu-His complex in aqueous solution by a careful analysis of the XANES and UV/Vis spectra. By making use of the reducing properties of the X-ray beam, as discussed in chapter 2, interesting information on the molecular structure of the Cu-His complex can be obtained. Chapter 6 describes the last step in the three-pronged approach: the discussion of the molecular structure of the zeolite Y immobilized Cu-His complexes. It will be demonstrated that the zeolite has multiple effects on the coordination and redox chemistry of zeolite-encaged Cu-His complexes. As a result, a discussion on the influence of the zeolite matrix on the molecular structure and redox chemistry of the Cu-His complex is presented. Furthermore, it allows comparing the molecular structure of the occluded complexes with the active site in GOase.

Finally, in chapter 7 a summary of the results of the preceding chapters is given. Besides that, also the use of the multi-technique approach to solve the molecular structure of the Cu-His complex within the pore system of zeolite Y is evaluated and conclusions on the influence of the zeolite on the molecular structure of TMI complexes in general will be drawn. It will be shown that – similar to the field of bioinorganic chemistry³⁷ – a large variety of powerful spectroscopic techniques are needed in order to determine with high accuracy the local coordination geometry of transition metal ion complexes. Only then it will be possible to draw firm conclusions on the structural similarities between man-made and natural enzymes.

References

- [1] E. I. Stiefel, *Bioinorganic Catalysis*, Marcel Dekker Inc., New York, 1999.
- [2] A. S. Bommarius and B. R. Riebel, *Biocatalysis: Fundamentals and Applications*, Wiley-VCH, Weinheim, 2004.
- [3] J. M. Thomas and W. J. Thomas, *Principles and Practice of Heterogeneous Catalysis*, VCH, Weinheim, 1997.
- [4] I. E. Wachs and B. M. Weckhuysen, *Appl. Catal. A: General* **157** (1997) 67.
- [5] B. M. Weckhuysen and D. E. Keller, *Catal. Today* **78** (2003) 25.
- [6] B. Cornils, W. A. Herrmann, R. Schlogl and C. H. Wong, *Catalysis from A to Z: A Concise Encyclopedia*, Wiley-VCH, Weinheim, 2000.
- [7] P. R. O. de Montellano (Ed.), *Cytochrome P450 Structure, Mechanism and Bio-chemistry*, Plenum, New York, 1995.
- [8] I. H. Siegel, *Enzyme Kinetics*, John Wiley & Sons, New York, 1975.
- [9] G. Ertl, H. Knözinger and J. Weitkamp, *Handbook of Heterogeneous Catalysis*, Wiley-VCH, Weinheim, 1997.
- [10] M. Baerns (Ed.), *Basic Principles in Applied Catalysis*, Springer, Berlin, 2004.
- [11] M. Gerloch and E. C. Constable, *Transition Metal Chemistry*, VCH, Weinheim, 1994.
- [12] S. S. Zumdahl and S. A. Zumdahl, *Chemistry*, Houghton Mifflin Company, Boston, 2003.
- [13] N. N. Greenwood and A. Earnshaw, *Chemistry of the Elements*, Pergamon Press, Oxford, 1984.
- [14] D. F. Shriver, P. W. Atkins and C. H. Langford, *Inorganic Chemistry*, Oxford University Press, Oxford, 1990.
- [15] H. G. Karge and J. Weitkamp, *Molecular Sieves: Science and Technology*, Springer, Berlin, 2004.
- [16] C. Baerlocher, W. M. Meier and D. H. Olson, *Atlas of Zeolite Framework Types*, Elsevier Science B.V., Amsterdam, 2001.
- [17] D. E. de Vos, P. P. Knops-Gerrits, R. F. Parton, B. M. Weckhuysen, P. A. Jacobs and R. A. Schoonheydt, *J. Inclus. Phen. Mol. Rec. Chem.* **2** (1995) 185.
- [18] D. E. de Vos, M. Dams, B. F. Sels and P. A. Jacobs, *Chem. Rev.* **102** (2002) 3615.
- [19] A. K. Dillow and A. M. Lowman (Eds), *Biomimetic Materials and Design, Biointerfacial Strategies, Tissue Engineering and Targeted Drug Delivery*, Marcel Dekker Inc., New York, 2002.

- [20] M. A. Halcrow, P. F. Knowles and S. E. V. Phillips, *Handbook of Metalloproteins*, Marcel Dekker Inc., New York, 2001.
- [21] N. Ito, S. E. V. Phillips, C. Stevens, Z. B. Orgel, M. J. McPherson, J. N. Keen, K. D. S. Yadav and P. F. Knowles, *Nature* **350** (1991) 87.
- [22] N. Ito, S. E. V. Phillips, K. D. S. Yadav and P. F. Knowles, *J. Mol. Biol.* **238** (1994) 794.
- [23] A. J. Baron, C. Stevens, C. Wilmot, K. D. Seneviratne, V. Blakeley, D. M. Dooley, S. E. V. Phillips, P. F. Knowles and M. J. McPherson, *Biochemistry* **33** (1994) 25095.
- [24] K. D. Karlin and A. D. Zuberbuhler, *Bioinorganic Catalysis*, Marcel Dekker Inc., New York, 1999.
- [25] M. M. Whittaker, V. L. DeVito, S. A. Asher and J. W. Whittaker, *J. Biol. Chem.* **264** (1989) 7104.
- [26] G. T. Babcock, M. K. El-Deeb, P. O. Sandusky, M. M. Whittaker and J. W. Whittaker, *J. Am. Chem. Soc.* **114** (1992) 3727.
- [27] J. W. Whittaker, *Met. Ions. Biol. Syst.* **30** (1994) 315.
- [28] M. M. Whittaker and J. W. Whittaker, *J. Biol. Chem.* **263** (1988) 6074.
- [29] P. F. Knowles, R. D. Brown, S. H. Koenig, S. Wang, R. A. Scott, M. A. McGuirl, D. E. Brown and D. M. Dooley, *Inorg. Chem.* **34** (1995) 3895.
- [30] S. J. Firbank, M. S. Rogers, C. M. Wilmot, D. M. Dooley, M. A. Halcrow, P. F. Knowles, M. J. McPherson and S. E. V. Phillips, *Proc. Nat. Acad. Sci.* **98** (2001) 12932.
- [31] B. M. Weckhuysen, A. A. Verberckmoes, I. P. Vannijvel, J. A. Pelgrims, P. L. Buskens, P. A. Jacobs and R. A. Schoonheydt, *Angew. Chem. Int. Ed. Engl.* **34** (1995) 2652.
- [32] J. F. Andersen, A. Weichsel, C. A. Balfour, D. E. Champagne and W. R. Montfort, *Structure* **6** (1998) 1315.
- [33] B. M. Weckhuysen, A. A. Verberckmoes, L. Fu and R. A. Schoonheydt, *J. Phys. Chem.* **100** (1996) 9456.
- [34] L. Fu, B. M. Weckhuysen, A. A. Verberckmoes and R. A. Schoonheydt, *Clay Miner.* **31** (1996) 491.
- [35] R. Grommen, P. Manikandan, Y. Gao, T. Shane, J. J. Shane, R. A. Schoonheydt, B. M. Weckhuysen and D. Goldfarb, *J. Am. Chem. Soc.* **122** (2000) 11488.
- [36] D. Baute, D. Arieli, F. Neese, H. Zimmermann, B. M. Weckhuysen and D. Goldfarb, *J. Am. Chem. Soc.* **126** (2004) 11733.
- [37] L. Que (Ed.), *Physical Methods in Bioinorganic Chemistry: Spectroscopy and Magnetism*, University Science Books, Sausalito, 2000.

Chapter 2

Synchrotron Radiation Effects as Studied in a Combined UV-Vis/XAFS Setup

Abstract

UV-Vis spectroscopy was used in a combined *in-situ* UV-Vis/XAFS spectroscopic set-up to study the synchrotron radiation effects on aqueous homogeneous copper solutions. Two different systems were studied. In the first study the focus was on the copper 2,2'-bipyridine (1:1) catalyzed oxidation of benzyl alcohol to benzaldehyde with 2,2,6,6-tetramethylpiperidiny-1-oxyl and base as co-catalysts. In the second study the same reaction was studied with a copper 1,10-phenanthroline (1:2) catalyst. It was found that when the reaction mixture is exposed to the X-ray beam, the features present in the *in-situ* UV-Vis spectrum develop differently compared to the situation when the reaction mixture is not exposed to the X-ray beam. Besides a heating effect of the X-ray beam both the UV-Vis analysis and the XAFS analysis showed a reducing influence of the X-ray beam on the sample. In order to investigate this phenomenon in more detail a series of dilute aqueous copper solutions from different precursor salts, *viz.* $\text{Cu}(\text{NO}_3)_2 \cdot 3\text{H}_2\text{O}$, $\text{CuSO}_4 \cdot 5\text{H}_2\text{O}$, CuCl_2 and CuBr_2 were studied at different beamlines, both with high and low photon flux. It was found that different aqueous copper solutions have different stabilities when they are exposed to an X-ray beam. Especially the solutions from the halogen containing precursor salts were found to be unstable and subject to reduction. The work illustrates the advantage of a second technique (UV-Vis spectroscopy) to evaluate the effect of synchrotron radiation used to measure *in-situ* XAFS on catalytic systems.

2.1 Introduction

In catalysis there is an increasing trend in using *in-situ* spectroscopic techniques to elucidate the reaction mechanism of a catalytic process as well as to attempt to identify the active site and the associated reaction intermediates.¹⁻⁵ Since each species has a specific spectroscopic fingerprint it has been shown that such reaction mechanisms can only be elucidated by making use of multiple characterization techniques. Because of the need for a multi-technique approach, it may not wonder that scientists in recent years have tried to combine two characterization techniques in one reaction set-up. Examples are XRD/XAFS,⁶⁻⁹ XAFS/UV-Vis,^{10,11} UV-Vis/Raman¹²⁻¹⁵ and UV-Vis/EPR.¹⁶⁻¹⁸ Thus, complementary information about the catalytic system can be obtained at the same time and measured under identical process conditions guaranteeing the validity of the measured species for building up the reaction scheme.¹⁹

In this work it will be shown that there is an additional advantage of performing combined *in-situ* spectroscopy on catalytic systems. It is known that high-intensity light sources, such as laser light, UV-light and synchrotron radiation, may influence the state of the catalyst and its reaction medium, ranging from sample heating, changing oxidation-reduction behavior, up to even the destruction of the active site.²⁰⁻²² One way to track such changes is by making use of a second spectroscopic technique attached to the reaction vessel. In this work, we will show the advantages of an *in-situ* UV-Vis/ED-XAFS set-up for probing the state of the catalyst material in the presence and absence of a synchrotron X-ray beam. For this purpose different experiments were performed. In the first experiment the oxidation of benzyl alcohol using a copper bipyridine complex in a water/NMP mixture (1:1), with 2,2,6,6-tetramethylpiperidinyl-1-oxyl (TEMPO) and base as co-catalysts, was studied. The same reaction was also studied by using a copper 1,10-phenanthroline complex (1:2) as a catalyst. In the last part the focus was on the study of aqueous copper solutions from different copper precursor salts. Although sometimes ignored in the field of catalysis, it will be shown that, depending on the reaction mixture composition as well as on the catalyst system under investigation, unexpected effects may occur, which otherwise would have remained unnoticed when only the *in-situ* XAFS technique would have been applied.

2.2 Experimental

2.2.1 Solutions and reactions

The oxidation of benzyl alcohol was carried out in an NMP/H₂O (1:1) solvent mixture at room temperature. NMP (N-Methylpyrrolidone) was used as a co-solvent to increase the solubility of the copper complexes. Two different copper complex containing solutions were used in the oxidation reaction: a 0.06 M CuBr₂/bipyridine (1:1) solution and a 0.045 M CuBr₂/1,10-phenanthroline (1:2) solution. To start the reaction four different solutions were mixed: the copper complex containing solution, a benzyl alcohol solution, a 2,2,6,6-tetramethylpiperidiny-1-oxyl (TEMPO) solution and a tetraethylammoniumhydroxide (TEAOH) solution, the concentration in the last three solutions being equimolar to the copper concentration of the first solution. The four solutions were mixed in a 1:1:1:1 ratio, resulting in an 0.015 M copper concentration in the cuvette for the Cu-bipyridine catalyzed system and 0.01125 M for the Cu-1,10-phenanthroline catalyzed system. The NMP solvent (Biosolve), CuBr₂ (Acros, 99%+), 2,2'-bipyridine (Acros, 99%+), 1,10-phenanthroline (Acros, 99%+), benzyl alcohol (Aldrich, 99%+), TEMPO (Acros, 98%) and 20 wt% TEAOH in H₂O (Acros) were used without further purification. The concentration of the copper-bipyridine (1:1) complex in NMP/H₂O (1:1) for the stability experiments was 0.06 M. The UV-Vis/ED-XAFS experiments on the aqueous copper solutions were performed with both 0.01 and 0.06 M solutions from different copper precursor salts: Cu(NO₃)₂·3H₂O, CuSO₄·5H₂O, CuCl₂ (all from Merck, *p.a.*) and CuBr₂ (Acros, 99%+).

2.2.2 Characterization and UV-Vis/ED-XAFS set-up

The UV-Vis/ED-XAFS data were collected at the undulator beam line ID24 of the European Synchrotron Radiation Facility (ESRF, Grenoble, France). A specially designed set-up was used (see for a schematic overview Figure 1).^{10, 11} The solutions were brought into a specially designed black quartz cuvette using the commercially available Bio-logic stopped flow module (SFM-400). The cuvette has a path length of 5 mm in both the X-ray and the UV-Vis direction and a total sample volume of 80 μ l. The transparent quartz windows in the

X-ray direction have a thickness of 100 μm in order to minimize X-ray absorption at the energy of the copper edge by the windows. To protect the sample from heating and degradation by the high photon flux of the X-rays (10^{12} photons s^{-1}) a beam shutter is placed in front of the sample. The shutter is only opened when X-ray absorption measurements are performed. The spot size of the X-ray beam in the focal spot in the sample is $0.03 \times 0.2 \text{ mm}^2$ (H x V, FWHM).

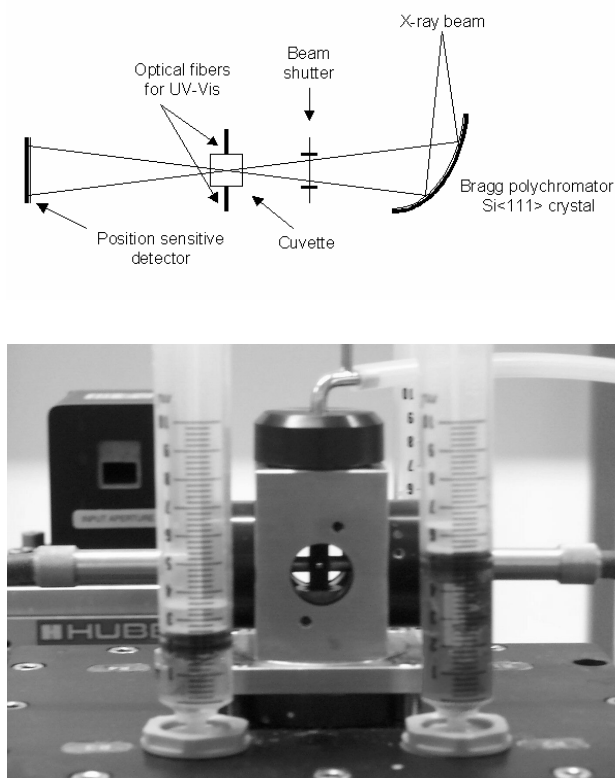


Figure 1. Schematic top-view representation of the set-up (a) and picture (b) of the cuvette in the observation head on top of the Stopped Flow Module (SFM), seen in the direction of the X-ray beam. The optical fibers for the UV-Vis analyses can be seen on the left and the right, as well as the syringes used to fill the SFM. Back in the left is the beam shutter and on top is the pipe to the waste bin.

The XAFS data were collected using a phosphorous-masked Peltier cooled Princeton CCD camera. The X-rays were focused on the sample using a curved Si(111) Bragg polychromator crystal. The energy of the monochromator was calibrated by measuring the absorption edge of a copper foil (8979 eV) prior to and following every energy scan. The UV-Vis spectra (in the range from 200-735 nm) were collected in transmission mode, perpendicular to the incident X-ray beam, using an MMS-UV1/500-1 high speed diode

spectrometer equipped with optical fibers. This spectrometer is able to collect a complete UV-Vis absorption spectrum in 0.8 ms. For the oxidation of benzyl alcohol every 9.5 s a new XAFS spectrum was recorded. The first 8 s are for the collection of the XAFS data, followed by 1.5 s for read-out of the data. During this read-out period the beam shutter is closed. In this way 25 XAFS spectra were collected in time, covering the first 4 min of the reaction. This procedure was repeated 15 times to improve the signal to noise ratio of the XAFS data. In some experiments a thermocouple was placed inside the cuvette, above the plane of the X-ray beam, to measure changes in the temperature of the reaction mixture when it was exposed to the X-ray beam.

The Cu K-edge XAFS spectra of 0.01 M aqueous copper solutions from different precursor salts were collected at the Dutch-Belgian beam line (DUBBLE) at BM26A of the ESRF. The measurements were performed at room temperature with a Si(111) double crystal monochromator. The liquid samples were measured in stainless steel cells (diameter of 2.5 mm) with kapton windows. The spot size on the sample is $0.5 \times 0.5 \text{ mm}^2$ (HxV, FWHM), with a photon flux of $10^{11} \text{ photons s}^{-1}$. The XAFS spectra were collected in the fluorescence mode, in a 90-degree orientation to the incident X-ray beam, using a nine-channel monolithic germanium detector. The time required to record one complete XAFS spectrum is 45 min.

TEM images were obtained with a Fei Technai 20 FEG TEM operating at 200 kV. Samples were, after centrifugal treatment and resuspension in water, dispersed on a glow discharge pre-treated, copper grid supported, holey carbon film.

2.3 Results

The combination of the UV-Vis and the ED-XAFS techniques was used with the intention to study the mechanism of the oxidation of benzyl alcohol to benzaldehyde using a copper bipyridine (1:1) complex in the presence of TEMPO and base as co-catalysts. The catalytic activity was found to be higher when using CuBr_2 as a precursor salt for the Cu-bipyridine solution (compared to the CuCl_2 and $\text{Cu}(\text{NO}_3)_2$ precursor salts).²³ A Cu^+ species is proposed to be an intermediate in the mechanism of the reaction.²³ UV-Vis and XAFS spectroscopy are both techniques that are very well capable of showing changes in the oxidation state of copper. In the UV-Vis spectrum Cu^{2+} (d^9) has a d-d transition in the region

of 600-800 nm, whereas in Cu^+ (d^{10}) this d-d transition is not present. In XAFS spectroscopy Cu^+ (and also Cu^0) are characterized by a pre-edge feature in the 8980-8985 eV region of the XANES of the copper edge. This feature is not present for Cu^{2+} .²⁴ The combination of the two techniques is very informative for studying changes in the oxidation state of a copper system.

2.3.1 Copper 2,2'-bipyridine (1:1) system

First the propagation of the copper 2,2'-bipyridine catalyzed oxidation of benzyl alcohol was monitored in the UV-Vis/ED-XAFS set-up by UV-Vis spectroscopy alone.

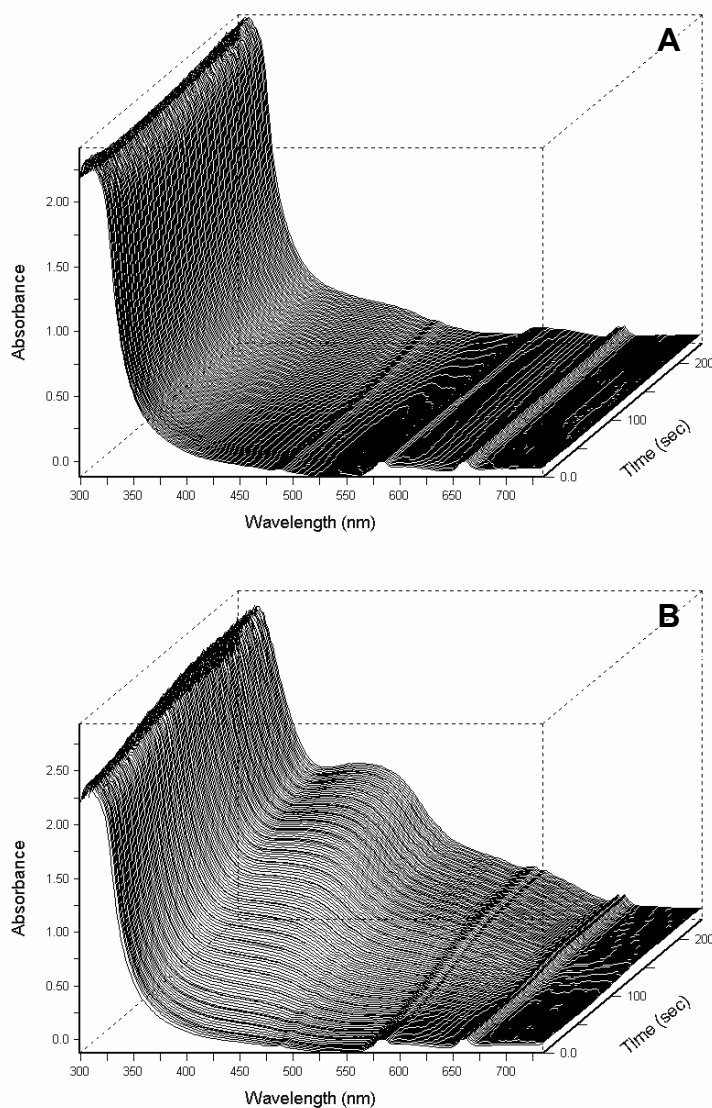


Figure 2. UV-Vis absorption spectra of the oxidation reaction of benzyl alcohol to benzaldehyde using copper bipyridine as catalyst and TEMPO and base as co-catalysts, (A) without, (B) with the X-ray beam on the sample.

The development of the first 4 min of the reaction is shown in Figure 2a. Around 420 nm a band is developing in time, which can be assigned to a metal to ligand charge transfer transition in a mononuclear copper species.²⁵ The development of the intensity of this band in time is indicated by line **a** in Figure 3. However, when the UV-Vis spectra are recorded with the X-ray beam exposed to the reaction mixture (Figure 2b), the development of this band in time is much faster (line **b** in Figure 3). What also attracts the attention is the repetitive pattern that is visible in the development of the 420 nm band in Figure 3b. This pattern is absent when there is no X-ray beam on the sample. The origin from this pattern is the closing of the beam shutter, which is closed for 1.5 s after each XAFS measurement for data read-out. In these 1.5 s the intensity of the UV-Vis absorption band decreases. After re-opening of the beam shutter for the next XAFS measurement the absorption starts to rise again. These results clearly indicate that the X-ray beam is influencing the reaction mixture in the cuvette.

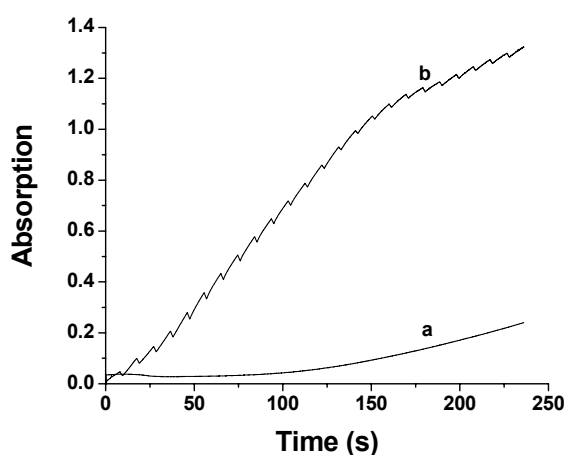


Figure 3. Evolution of the band at 420 nm in the UV-Vis spectra in time for the oxidation of benzyl alcohol to benzaldehyde using copper bipyridine as catalyst and TEMPO and base as co-catalysts: (a) without and (b) with X-ray beam.

The explanation for the difference in the UV-Vis absorption spectra with and without the X-ray beam on the reaction mixture could be a temperature effect that the X-ray beam has on the sample. The reaction mixture is heated in the plane of the dispersive X-ray beam, which speeds up complex formation and/or catalytic activity. As soon as the beam shutter is closed the heating stops and the heat and/or complexes in the plane of the X-ray beam start to exchange with the rest of the reaction mixture, which is not in the plane of the beam. This causes a decrease of the absorption in the UV-Vis spectrum during the 1.5 s the beam shutter

is closed and gives rise to the saw-tooth pattern in line **b** in Figure 3. To check this hypothesis, the temperature of the reaction mixture in the cuvette (out of the plane of the X-ray beam) was measured. It was found that as soon as the beam shutter was opened the temperature of the reaction mixture instantaneously increased by about one degree Celsius, after which it stabilized. After closing of the beam shutter the temperature decreased within a few seconds back to its original value. This indicates that there is a temperature effect of the X-ray beam on the sample; an effect that will be quite large in the plane of the X-ray beam. To quantify this effect the radiation dose per second on the sample was calculated.^{20, 26} This value was used to calculate the energy release per second in the volume exposed to the X-ray beam. Together with the value for the heat capacity of the solvent this gave a temperature rise in the volume of the plane of the X-ray beam of 14°C/s. These theoretical calculations prove that locally (especially around the plane of the X-ray beam) the temperature in the cuvette can increase dramatically. This can be an explanation for the faster upcoming of the 420 nm band when the sample is exposed to the X-ray beam. If this heating would be the only effect of the X-ray beam on the sample (provided it is not too much), the data could still be used for analysis of the species involved in the reaction mechanism.

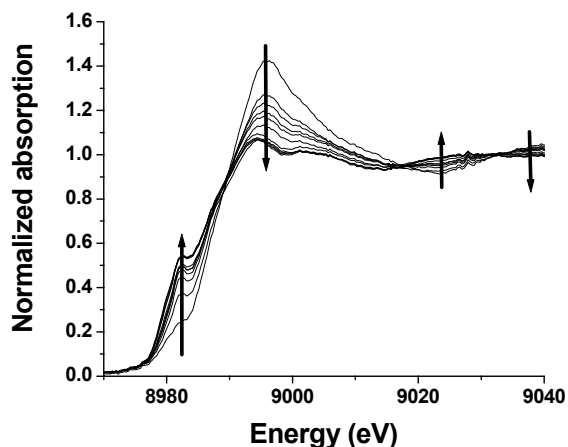


Figure 4. X-ray absorption spectra for the first 4 min of the oxidation of benzyl alcohol to benzaldehyde. The time between two consecutive absorption spectra is 9 s. The trends in time are indicated with the arrows.

However, there is an additional explanation for the observed differences. The X-ray absorption spectra of the first 4 min of the reaction (with a 9 s time resolution) are shown in Figure 4. Very large changes in the X-ray absorption spectra are occurring in the first minute of the reaction (indicated with arrows). A pre-edge feature in the region 8980-8985 eV of the

XANES region (typical for Cu^+ , but also for Cu^0) is coming up and the white line intensity decreases strongly. These changes suggest that reduction of the copper is occurring. Besides that, the features in the EXAFS region are changing completely. At first sight nothing strange is happening: the species participating in the oxidation reaction are probed and the XAFS results suggest the formation of a Cu^+ intermediate. In the last 3 min of the reaction only minor changes occur, *viz.* the development of a feature at 8979-8980 eV. However, based on the increase of the XANES feature around 8979 eV in time and the evolution of the features present in the EXAFS to features present in a copper foil (Figure 5), the formation of metallic copper is suggested.²⁷

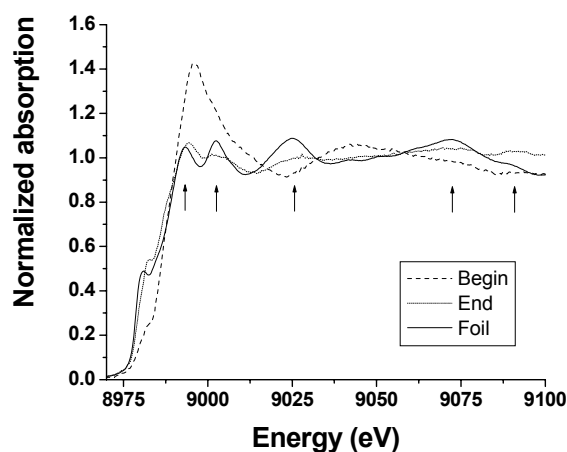


Figure 5. The X-ray absorption spectrum of a copper foil compared to the absorption spectrum of the sample after 4 min. The arrows indicate the reproduced features in the EXAFS of both samples. Also the X-ray absorption spectrum at the beginning of the reaction is shown.

In order to determine what is happening in the reaction mixture, the copper system was studied without catalytic reaction. To that end the copper bipyridine solution was measured without substrate and co-catalysts. Without X-ray beam a copper-bipyridine (1:1) solution in water/NMP (1:1) is stable in time, since there are no changes observed in the UV-Vis absorption spectrum in time. However, when this solution is exposed to the X-ray beam it is no longer stable. The absorption in the UV-Vis spectrum starts to increase over the total wavelength range and features around 460 nm and 540 nm start to develop (Figure 6). Analysis of the X-ray absorption spectra showed that all the changes that are visible in the X-ray absorption spectra of these solutions are exactly the same as those for the complete reaction mixture. These results show that the X-ray beam also has a strong reducing effect on

the sample and support the hypothesis about the formation of colloidal copper. This hypothesis is also confirmed by the UV-Vis results: the increase in absorption in the UV-Vis spectra in time is caused by the formation of colloidal copper, which causes a decrease in transmission of the sample. This process is the reason for the fast development of the 420 nm band as visualized in Figure 3. The absorption of the colloidal particles is superimposed on the absorption of the catalytic species in the 420 nm area.

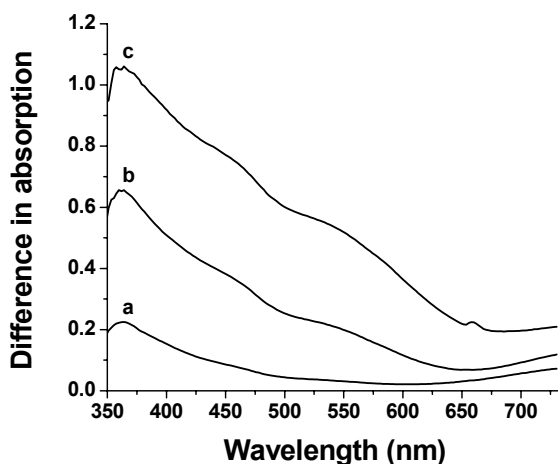


Figure 6. The difference in the absorption of the UV-Vis spectra with respect to the absorption before the X-ray beam was on the copper bipyridine solution, after (a) 100 s, (b) 200 s and (c) 300 s of X-ray irradiation.

So the study of the oxidation reaction in the UV-Vis/ED-XAS set-up shows that two processes are occurring at the same time in the cuvette. Within the plane of the X-ray beam mainly the reduction/heating process occurs, whereas in the rest of the cuvette mainly the normal catalytic reaction takes place, only influenced by the temperature effect of the X-ray beam. With the UV-Vis technique a superposition of both processes is probed, because the area probed by the UV-Vis technique in the cuvette is much larger than the plane of the X-ray beam (ratio of about 500:1). As a result the largest part of the species that are probed by UV-Vis will be the ones that participate in catalysis. However, all the species that are probed by the XAFS technique have been exposed to the X-ray beam, so the X-ray absorption spectra will show more pronounced the effect the X-ray beam has on the sample.

Of course it is a possibility that the reducing influence of the X-ray beam is facilitated or even caused by the presence of the bipyridine ligand. Therefore we also studied the influence of the X-ray beam on aqueous copper solutions from different precursor salts, to check whether the

same processes are occurring to Cu^{2+} under influence of the X-ray beam without the presence of a ligand.

2.3.2 Copper from different precursor salts

The stability of aqueous copper solutions from four different Cu(II) precursor salts under influence of the X-ray beam was investigated. The solutions from the $\text{CuSO}_4 \cdot 5\text{H}_2\text{O}$ and $\text{Cu}(\text{NO}_3)_2 \cdot 3\text{H}_2\text{O}$ precursor salts were exposed for 10 min in the cuvette and found to be stable under influence of the dispersive X-ray beam. There was however a reducing effect on the solutions from CuBr_2 and CuCl_2 , the effect being larger for the CuCl_2 solution. The X-ray absorption spectra at the beginning and the end of the exposure time and the UV-Vis spectra during the first 5 min of exposure of the CuCl_2 solution to the X-ray beam are shown in Figures 7 and 8 respectively. Again the Cu^+/Cu^0 pre-edge feature is coming up and the white line is going down in time and the absorption in the UV-Vis is increasing in time.

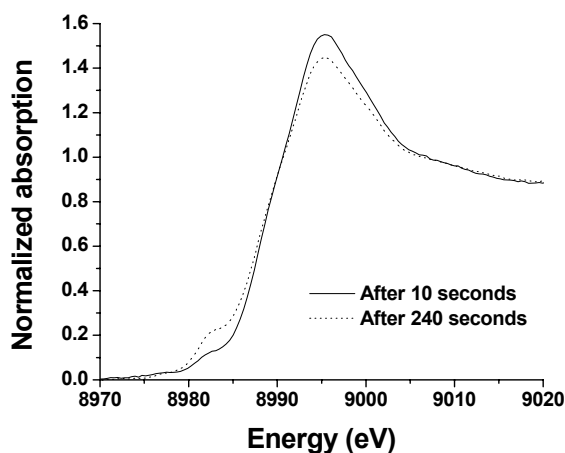


Figure 7. XANES spectra of the 0.06 M aqueous CuCl_2 solution after 10 s and 240 s of exposure.

So it seems that the presence of halide is responsible for the reducing effect of the X-ray beam. Indeed, the process was found to be dependent on the halide concentration: the higher the halide concentration (obtained by adding the sodium salt of the halide), the faster the development of the pre-edge feature in time and the faster the increase of the absorption in the UV-Vis absorption spectra.

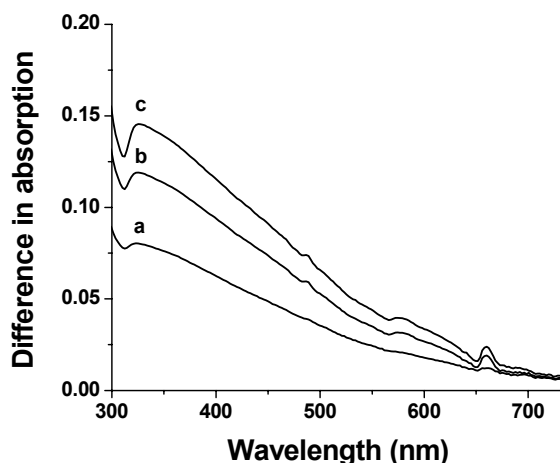


Figure 8. The difference in UV-Vis absorption spectra of a CuCl_2 solution with respect to a solution that not has been exposed to the X-ray beam, after (a) 80 s, (b) 160 s and (c) 240 s exposure to the X-ray beam.

To check the hypothesis of the formation of colloidal copper, one of the 60 mM CuCl_2 solutions that had been exposed to the X-ray beam was studied with transmission electron microscopy (TEM). The result is shown in Figure 9. In the sample the colloidal copper particles are clearly visible. The particle size distribution of the copper particles is quite homogeneous, in the range of 2-3 nm. These TEM results confirm the formation of colloidal copper particles.

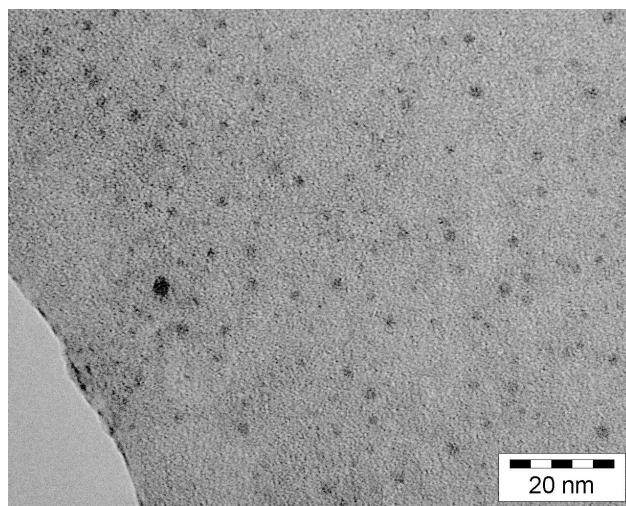


Figure 9. TEM image of the colloidal copper particles found in the aqueous CuCl_2 solutions after X-ray exposure. Most of the particles have a diameter of 2-3 nm.

The UV-Vis/ED-XAFS set-up is designed to collect X-ray absorption spectra within seconds. To achieve this all X-ray energies are focused on the sample at the same time. This makes that the radiation dose, especially at the small focal spot in the sample ($0.03 \times 0.2 \text{ mm}^2$ (HxV)), with a flux of $10^{12} \text{ photons s}^{-1}$ is very high. This high dose is the reason for the very fast formation of the colloidal copper particles. To test the influence of the photon flux the stability experiments with the aqueous copper solutions were repeated at DUBBLE. The radiation dose in the larger focal spot ($0.5 \times 0.5 \text{ mm}^2$ (HxV)) at this bending magnet beamline with a flux of $10^{11} \text{ photons s}^{-1}$ is 381 J/kg in a total volume of $6.25 \cdot 10^{-10} \text{ m}^3$. This value is much lower than on the ED-XAFS beam line ID24, where the radiation dose is 41545 J/kg in a volume of only $4.0 \cdot 10^{-11} \text{ m}^3$. So, if the flux of the incoming X-ray beam is responsible for

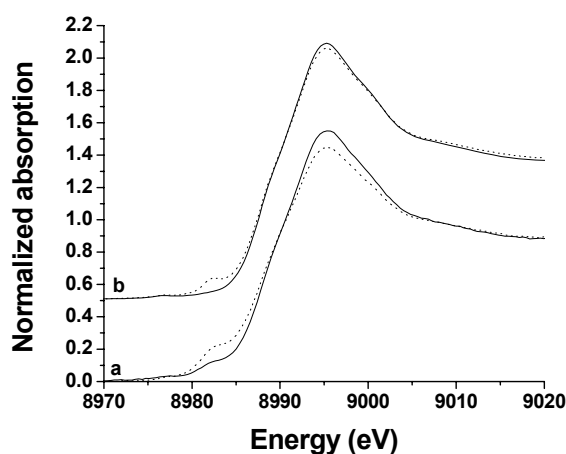


Figure 10. Comparison of the development in the X-ray absorption spectra at (a) ID24 after 10 and 240 s respectively and (b) DUBBLE after 45 min and 225 min respectively.

the reducing influence, the reducing behavior is expected to be orders of magnitudes lower. The different aqueous copper solutions were exposed to the X-ray beam for several hours. It takes about 45 min to collect a qualitatively good and complete X-ray absorption spectrum. Although the radiation dose at DUBBLE is much lower, exactly the same trends in stability were found for the copper salts, only at a different time scale (Figure 10). The solutions from the sulphate and the nitrate salts are stable and the copper solution from the CuCl_2 salt is more susceptible to reduction than the CuBr_2 salt. Again, increasing the chloride concentration increased the speed of the reduction process. This indicates that lowering the radiation dose on a sample does not prevent radiation damage to occur; it only slows down the process.

2.3.3 Copper 1,10-phenanthroline (1:2) system

The oxidation of benzyl alcohol was also studied in the combined UV-Vis/ED-XAFS setup using a Cu/1,10-phenanthroline complex as catalyst. This system differs from the Cu/2,2-bipyridine system in the sense that there are twice as much ligands available per copper ion. Figure 11 shows the set of UV-Vis spectra of the CuBr₂/phenanthroline reaction mixture measured in the presence and absence of the X-ray beam.

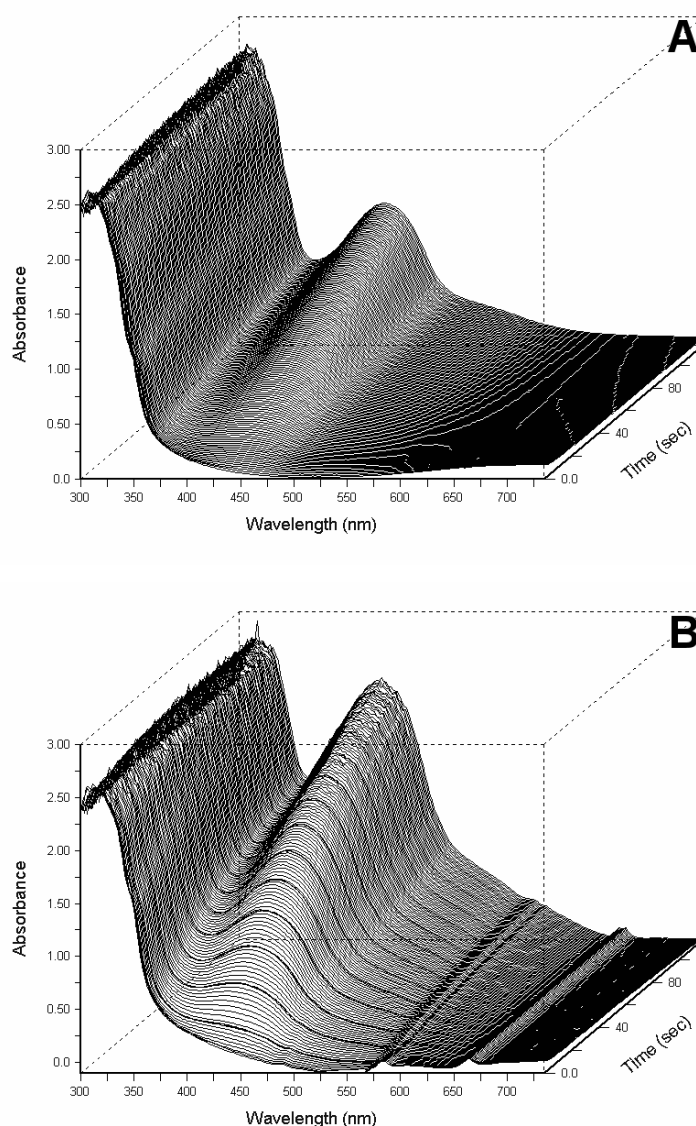


Figure 11. The development of the UV-Vis features for the complete reaction mixture in the Cu/1,10-phenanthroline catalyzed oxidation of benzyl alcohol (A) without and (B) with the reaction mixture exposed to the X-ray beam.

It is evident that both sets of spectra show an increase of an absorption band around 433 nm with reaction time, as well as a decrease of a broad absorption band at 735 nm. Again there are remarkable differences between the spectra obtained in the presence and absence of the X-ray beam.

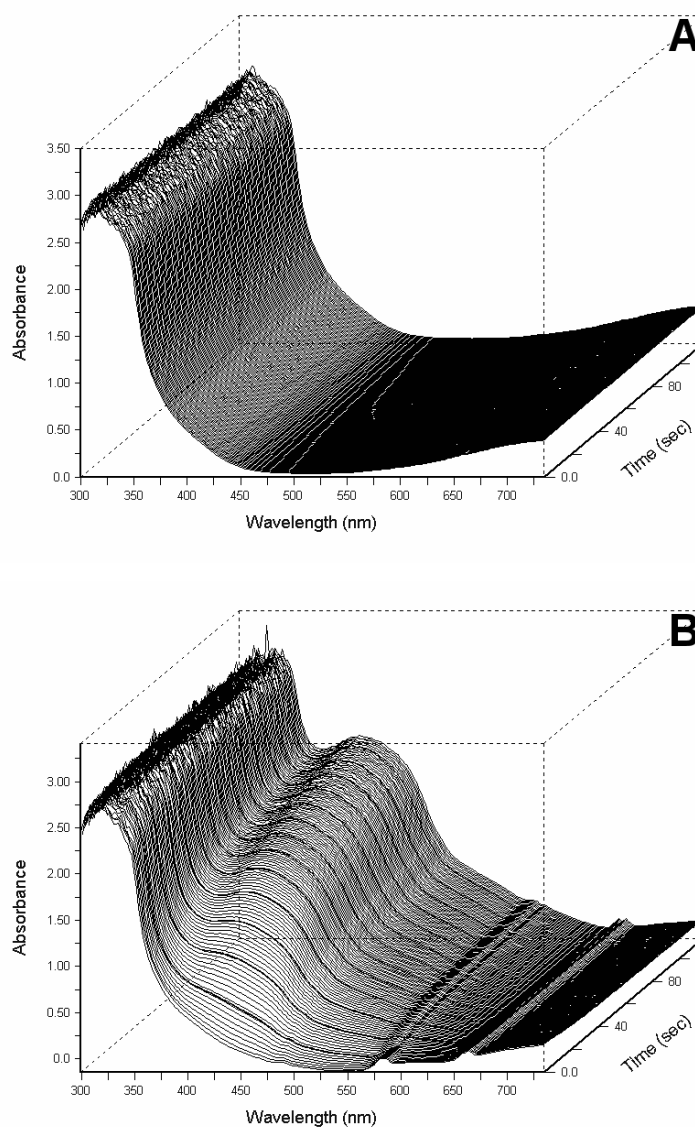


Figure 12. The development of the UV-Vis features for the reaction mixture without the presence of a reducing agent in the Cu/1,10-phenanthroline catalyzed oxidation of benzyl alcohol (A) without and (B) with the reaction mixture exposed to the X-ray beam.

An even more striking difference is observed when the developments in the UV-Vis spectra are studied in the absence of the reducing agent (see Figure 12). When the reaction mixture is

not exposed to the X-ray beam nothing is changing in the UV-Vis spectrum as a function of time. When, however, the same reaction mixture is exposed to the X-ray beam the characteristic band for the Cu^+ species comes up again and increases in time. The formation of a Cu^+ species is also confirmed by the upcoming of the Cu^+ feature in the XANES region of the X-ray absorption spectra collected at the same time. These observations again very well illustrate the reducing effect the synchrotron X-ray beam can have on the samples under study.

2.4 Discussion

It is known that in aqueous solutions radiolysis of water can occur under influence of X-rays.^{27, 28} This radiolysis process generates all kinds of species, like $\text{OH}\cdot$ and $\text{H}\cdot$ radicals, but also species like OH^- , H^+ and hydrated electrons. Usually recombination of the radiolysis products occurs. But when a scavenger takes away one of the products of the radiolysis process recombination can no longer take place and accumulation of the radiolysis products occurs. In this way also accumulation of the hydrated electrons can occur. These hydrated electrons can reduce the copper cations to the metallic state. It is possible that halide anions act as a scavenger of one of the radiolysis products, allowing the hydrated electron concentration and thus the speed of reduction to increase. Another explanation can be that nitrate and sulphate anions act as scavengers for hydrated electrons, thus protecting the copper cations from being reduced. Chloride and bromide anions are much less capable of doing that.

One has to realize that each characterization method will to a certain extent perturb the sample under investigation, *i.e.* the sample can undergo modifications due to the probe used to obtain chemical information from the sample. More specifically, high-intensity light sources, such as X-ray light (*e.g.* in the case of XAFS measurements making use of synchrotron radiation sources) and UV light (*e.g.* in the case of Raman measurements making use of UV lasers) are able to (1) generate new species in the reaction mixtures (solvent, reagent) that can influence chemical processes and/or (2) alter the molecular structure of the catalytic system under investigation. These effects can take place even at low radiation doses, *i.e.* such effects can also take place with synchrotron light sources making use of bending magnets, where the long exposure time may lead to a too high total light flux. This means that for every X-ray

absorption experiment it should be evaluated whether an observed change in oxidation state originates from the reaction under study or that it is merely due to an influence of the X-ray beam. In this study we show that the combined *in-situ* UV-Vis/ED-XAFS stopped flow set-up is ideally suited to check the influence of X-ray radiation on catalytic systems. This is a second example in which the combination of two *in-situ* techniques in one experimental set-up has an additional advantage besides providing experimental evidence for the existence or absence of catalytically active species or reaction intermediates. The first example comprised the use of *in-situ* UV-Vis spectroscopy to quantify *in-situ* Raman spectra of a catalytic solid under working conditions without the use of an internal standard.

2.5 Conclusions

The results presented in this chapter show an additional advantage of combining two different *in-situ* characterization techniques in one reaction set-up. A combination of *in-situ* UV-Vis and ED-XAFS techniques is useful to study reaction mechanisms in the homogeneous phase. In this specific case it also allowed probing of the effect of the X-ray beam on a copper sample. Using this set-up evidence for the occurrence of a temperature effect of the X-ray beam on the sample was found. This effect caused an increase in the rate of the catalytic process occurring in the cuvette. Besides that, proof for a reducing influence of the X-ray beam on the sample was also found. It was shown that the extent of the effect was influenced by the choice of the copper-precursor salt (halide concentration) and that the speed of the reduction process was influenced by the flux of the X-rays on the sample. It is very important to realize that the observed phenomena not only occur under “severe” X-ray exposure (undulator source, white beam), but are also observed (although at different time scales) under milder X-ray exposure (bending magnet, monochromatic X-rays).

This work illustrates the advantage of a second technique, such as *in-situ* UV-Vis spectroscopy, to evaluate the effect of synchrotron radiation, used to measure *in-situ* XAFS, on systems in aqueous solution. It should be stressed that this study does not imply that all synchrotron measurements are prone to radiation damage. Merely, we would like to draw attention to an often underestimated phenomenon in literature, which may lead to wrong

interpretations of the obtained *in-situ* XAFS data and consequently incorrect conclusions on the catalytic reaction cycle, especially when aqueous solutions are involved.

Acknowledgements

The European Synchrotron Radiation Facility (ESRF, Grenoble, France) is acknowledged for the provision of synchrotron radiation facilities. S. Pascarelli, S. G. Fiddy and G. Guilera of beamline ID24 (ESRF) and W. Bras and S. Nikitenko of DUBBLE (BM26A, ESRF) are thanked for their help and discussions during the XAFS experiments. We thank Hans Meeldijk (Utrecht University) for making TEM images. Isabel Arends (Delft University of Technology) and Patrick Gamez (Leiden University) are thanked for discussions on the copper bipyridine system. Moniek Tromp is acknowledged for introducing me to the combined UV-Vis/ED-XAFS set-up.

References

- [1] B. M. Weckhuysen (Ed.), *In-situ Spectroscopy of Catalysts*, American Scientific Publishers, Stevenson Ranch, 2004.
- [2] J. F. Haw (Ed.), *In-situ Spectroscopy in Heterogeneous Catalysis*, Wiley-VCH, Weinheim, 2002.
- [3] C. Lamberti, S. Bordiga, F. Bonino, C. Prestipino, G. Berlier, L. Capello, F. D'Acapito, F.X. Llabrés i Xamena and A. Zecchina, *Phys. Chem. Chem. Phys.* **5** (2003) 4502.
- [4] C. Lamberti, C. Prestipino, F. Bonino, L. Capello, S. Bordiga, G. Spoto, A. Zecchina, S. D. Moreno, B. Cremaschi, M. Garilli, A. Marsella, D. Carmello, S. Vidotto and G. Leofanti, *Angew. Chem. Int. Ed. Engl.* **41** (2002) 2341.
- [5] M. A. Newton, A. J. Dent, S. Diaz-Moreno, S. G. Fiddy and J. Evans, *Angew. Chem. Int. Ed. Engl.* **41** (2002) 2587.
- [6] B. S. Clausen, H. Topsøe and R. Frahm, *Adv. Catal.* **42** (1998) 315.
- [7] J.-D. Grunwaldt and B. S. Clausen, *Top. Catal.* **18** (2002) 37.
- [8] G. Sankar and J. M. Thomas, *Top. Catal.* **8** (1999) 1.
- [9] G. Sankar, J. M. Thomas and C. R. A. Catlow, *Top. Catal.* **10** (2000) 255.

- [10] M. Tromp, *Developments of Time-Resolved XAFS Spectroscopy Techniques*, Ph.D.Thesis, Utrecht University, Utrecht, 2004.
- [11] M. Tromp, J. R. A. Sietsma, J. A. van Bokhoven, G. P. A. van Stijdonck, R. J. van Haaren, A. M. J. van der Eerden, P. W. N. van Leeuwen and D. C. Koningsberger, *Chem. Commun.* (2003) 128.
- [12] T. A. Nijhuis, S. J. Tinnemans, T. Visser and B. M. Weckhuysen, *Phys. Chem. Chem. Phys.* **5** (2003) 4361.
- [13] T. A. Nijhuis, S. J. Tinnemans, T. Visser and B. M. Weckhuysen, *Chem. Eng. Sci.* **59** (2004) 5487.
- [14] S. J. Tinnemans, M. H. F. Kox, T. A. Nijhuis, T. Visser and B. M. Weckhuysen, *Phys. Chem. Chem. Phys.* **7** (2005) 211.
- [15] B. M. Weckhuysen, *Phys. Chem. Chem. Phys.* **5** (2003) 4351.
- [16] A. Bruckner, *Catal. Rev. Sci. Eng.* **45** (2003) 97.
- [17] A. Bruckner, *Chem. Commun.* (2001) 2122.
- [18] A. Bruckner, *Phys. Chem. Chem. Phys.* **5** (2003) 4461.
- [19] J.-D. Grunwaldt, M. Caravati, S. Hannemann and A. Baiker, *Phys. Chem. Chem. Phys.* **6** (2004) 3037.
- [20] T. Beetz, *Soft X-ray diffraction imaging with and without lenses and radiation damage studies*, Ph.D. Thesis, State University of New York, Stony Brook, 2004.
- [21] B. T. Bowie, D. B. Chase and P. R. Griffiths, *Appl. Spectrosc.* **54** (2000) 200A.
- [22] C. Li and P. C. Stair, *Catal. Today* **33** (1997) 353.
- [23] P. Gamez, I. W. C. E. Arends, R. A. Sheldon and J. Reedijk, *Adv. Synth. Catal.* **346** (2004) 805.
- [24] L.-S. Kau, D. J. Spira-Solomon, J. E. Penner-Hahn, K. E. Hodgson and E. I. Solomon, *J. Am. Chem. Soc.* **109** (1987) 6433.
- [25] A. B. P. Lever, *Inorganic Electronic Spectroscopy*, Elsevier Science B.V., Amsterdam, 1984.
- [26] T. Beetz and C. Jacobsen, *J. Synchrotron Rad.* **10** (2002) 280.
- [27] S. Jayanetti, R. A. Mayanovic, A. J. Anderson, W. A. Bassett and I.-M. Chou, *J. Chem. Phys.* **115** (2001) 954.
- [28] C. D. Jonah, *Radiat. Res.* **144** (1995) 141.

Chapter 3

Infrared and Raman Spectroscopic Study of pH-induced Structural Changes of L-histidine in Aqueous Environment

Abstract

Aqueous solutions of L-histidine (His) have been analyzed in parallel by infrared and Raman spectroscopy over the pH range 0-14 with increments of 1 pH unit. The vibrational spectra in the region $2000\text{-}500\text{ cm}^{-1}$ have been interpreted and band positions have been assigned, taking into account assignments from literature after critical evaluation. As a result a complete and complementary set of vibrational data has been obtained that can be used to determine all possible states of protonation of His, *i.e.* $\text{H}_4\text{His}^{2+}$, H_3His^+ , H_2His^0 , HHis^- and His^{2-} . In addition, IR and Raman bands have been proposed as markers for the presence of the imidazole N^π - or N^τ - protonated tautomeric forms of H_2His^0 and HHis^- .

3.1 Introduction

The elucidation of the secondary and tertiary structure of amino acid side chains has been the subject of research for many years. This is largely due to the fact that the spatial orientation plays a key role in the folding/unfolding ability of peptides and in the catalytic activity of enzymes. The pH is one of the driving forces in the orientation process, as it affects the state of protonation and hence the formation of hydrogen bridges and the number of binding sites for ions of transition metals, such as Cu, Fe and Co. An amino acid of major importance as a ligand in many metallo-enzymatic reactions is histidine.¹ Due to the presence of an imidazole ring the molecule possesses two extra potential sites for (de)protonation and metal binding in addition to the two (NH₂ and COOH) amino acid end groups. Besides, for two of the ionic structures histidine can be present in two pH-dependent tautomeric forms. As a consequence and as result of its flexible structure, histidine can occur in several pH-dependent states of protonation and coordination, either as part of a peptide backbone or as a free ligand molecule.

Next to NMR, infrared (IR) and Raman spectroscopy are commonly applied to obtain this type of structural information, as both techniques can be applied *in-vivo* and over a wide pH range. Moreover, the short time scale of vibrational absorption and relaxation in relation to the lifetime of free rotating structures and tautomeric equilibria, allows simultaneous qualitative and quantitative observation of all structures and ionic forms that are present in a chemical or biological system. Finally, IR and Raman are complementary techniques, which implies that an almost complete vibrational analysis is possible, particularly when combined with theoretical calculations. As a result many vibrational spectroscopic studies on histidine and related imidazole-type compounds have been carried out, providing a considerable amount of data in the literature, occasionally summarized in reviews²⁻⁸ and books.^{9, 10} To our knowledge, normal coordinate analysis (NCA) on histidine has not been carried out thus far and the first *ab initio* and density functional theory (DFT) study on the molecule was published only very recently.¹¹ However, this research concerned the conformational dependence of the pK_a values and not a vibrational analysis. For that reason, only results of theoretical calculations on the model compounds imidazole,^{12, 13} 4-methylimidazole,^{12, 14-17} and 4-ethylimidazole¹⁸ have been used to support the conclusions from empirical IR and Raman studies of histidine¹⁹⁻³⁶ and closely related molecules.³⁷⁻⁴¹ The majority of this

research has been focused on IR or Raman bands that can be used as a marker to determine the state of protonation of the imidazole nitrogen atoms^{15, 16, 20-27} or the type of metal ion binding^{24, 29, 32, 34, 37, 39, 40} and thus, measurements have been performed mainly under physiological conditions or at specific pH values close to the pK_a values of the different active sites. In addition, samples have often been measured in D₂O or after crystallization to circumvent interference from water bands. As a consequence there are large gaps in the availability of experimental vibrational data and assignments in H₂O, while an integrated IR and Raman study on aqueous solutions of histidine has, to our knowledge, not been published so far. Moreover, we noticed that some of the assignments and conclusions in literature are inconsistent or even conflicting. In order to clarify these controversies and obtain the lacking vibrational data we decided to carry out systematic and detailed IR and Raman measurements on histidine under well-defined experimental conditions. However, the main motivation for this work is to extend the pH region to high and low values, as this is important for the functionalization of inorganic substrates, such as zeolites, with amino acid complexes.^{42, 43} These hybrid materials are expected to have high potentials, not only in biomedical applications, but also as sensors, catalysts and molecular electronic devices.⁴⁴ For a better understanding and optimization of the structure/activity relationship it is important to have insight into the precise molecular structures and structural behaviour of the amino acids at pH values beyond those in biological systems. For that reason aqueous solutions have been measured in parallel with both techniques in the spectral region 2000-500 cm⁻¹ from pH = 0 to pH = 14 with increments of one pH unit. The resulting set of complementary spectral data has been interpreted and assigned to vibrational modes. In addition, the spectral data have been translated to bands that can be used as markers for the state of protonation, taking into account data and assignments from literature after careful comparison and evaluation. As a result, a more complete picture of aqueous histidine chemistry emerges.

3.2 Experimental

3.2.1 Chemicals and solutions

L-histidine (*p.a.* grade) was obtained from Acros Organics (Geel, Belgium). Solutions

were freshly made by dissolving L-histidine in demineralized water at a concentration of 38 g/l. Dissolution was promoted by exposure of the solution to ultrasound for 20 min. Solutions were made acidic by addition of HCl and basic by addition of NaOH. The pH was determined at ambient temperature (21°C) with a pH meter model PHM 210 from Radiometer Analytical (USA). In order to check the conversion reversibility from one state of protonation to another titration experiments from pH = 0 to pH = 14 and backwards have been carried out. The resulting IR and Raman data revealed full reversibility, which proves that degradation of the histidine molecules did not occur.

3.2.2 Characterization techniques

IR measurements were carried out at room temperature on a Perkin-Elmer 2000 Fourier Transform spectrometer equipped with a DTGS detector. The sample compartment was flushed with dry air to reduce interference of H₂O and CO₂. Spectra were recorded with a horizontal ATR accessory (Spectra-Tech) equipped with a ZnSe crystal as the reflecting element. The data point resolution of the spectra was 4 cm⁻¹ and 100 scans were accumulated for one spectrum. Spectral interpretation was carried out after subtraction of the spectrum of water at the corresponding pH as background.

Raman measurements were carried out on a Kaiser RXN spectrometer equipped with a 70 mW 785 nm diode laser for excitation, a holographic grating for dispersion and a Peltier cooled Andor CCD camera for detection. Spectra were recorded in glass vials (Spectra-Tech) at room temperature. The detector pixel resolution was about 2 cm⁻¹ and 15 scans were accumulated for one spectrum at an exposure time of 30 s per scan. Subtraction of the water background has not been performed for the Raman spectra.

3.3 Results and discussion

According to literature^{16, 23-25, 31, 32, 45, 46} histidine can be present in five different pH-dependent ionic forms, which are shown in Figure 1. In addition, the pK_a values of the different sites of protonation have been indicated according to reference 24. Furthermore, as depicted, the ionic structures H₂His⁰ and HHis⁻ can occur in two different tautomeric forms,

since the nitrogen atoms of the imidazole ring are not identical. The commonly accepted notation to distinguish (de)protonation of both atoms is N^π for the nitrogen atom which is closest to the CH_2 group and N^τ for the other one. Additionally, Blomberg *et al.*⁴⁶ proposed a third tautomeric form for H_2His^0 with intramolecular $\text{H}\cdots\text{N}$ bonding as indicated in Figure 1.

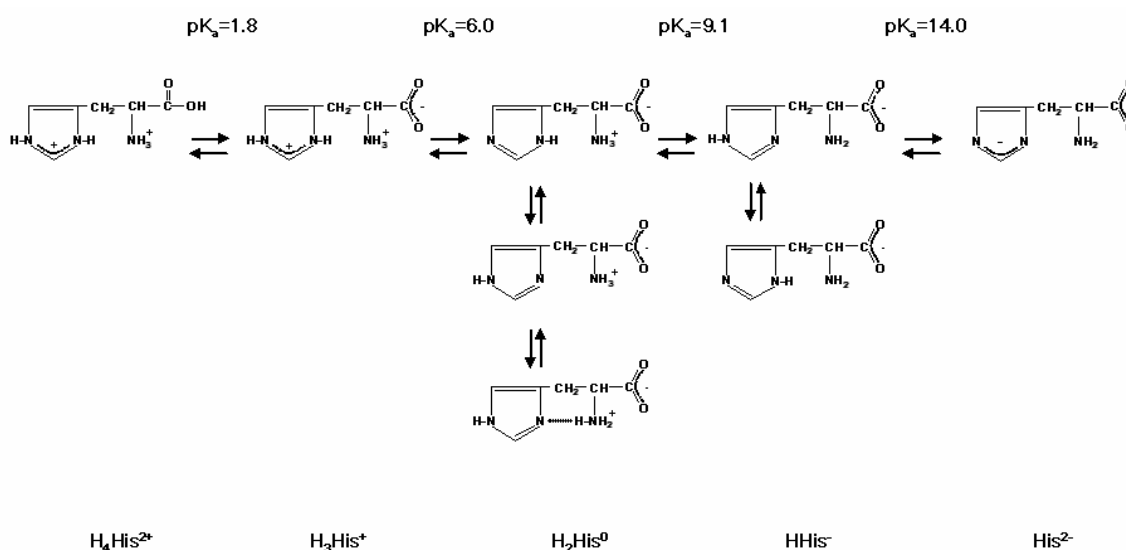


Figure 1: Proposed structures of the different states of protonation and tautomers of L-histidine in aqueous solution. The pK_a values have been taken from reference 24.

Theoretically, it should be possible to distinguish all these structures by differences in their vibrational spectroscopic features. Obviously, assignment will be relatively easy for bands related to characteristic functional group modes, provided the vibrations are sufficiently affected by a change in conformation or tautomeric form to be visible in the spectra. In contrast, less sensitive vibrations and less dramatic structural differences, such as between the three tautomeric forms of H_2His^0 , will be more difficult to distinguish with IR and Raman, particularly since a change in the dielectric constant of the solution as result of changing the pH or buffer concentration may cause frequency shifts as well. Hence, well-controlled experimental conditions have been applied to obtain accurate spectral data. For this reason the aqueous solutions of L-histidine have been measured in parallel by IR and Raman spectroscopy over the full pH range of 0-14. Besides, pH increments of 1 have been applied in order to monitor even small pH-effects on the spectra. A selection of the IR and Raman

spectra is presented in Figures 2 and 3, respectively. For reasons of clarity only spectra at even pH values are displayed. The observed IR and Raman band positions of all spectra, including the estimated positions of shoulders, are summarized in Tables 1 and 2, respectively. Assignments for most of the observed bands are proposed after spectral interpretation, taking into account IR and Raman selection rules and assignments extracted from literature. Data and assignments from literature have been carefully evaluated and occasionally simplified to obtain a fair compromise between the results from different theoretical models and from various experimental conditions (*e.g.* solutions in H₂O or D₂O, powders and single crystals, HCl salts).

3.3.1 The amino acid end groups

In a highly acidic environment histidine will be present mainly in the H₄His²⁺ ionic form (Figure 1) with all nitrogen atoms and the carboxylic acid group protonated. Indeed, the strong C=O stretching band at 1736 cm⁻¹ in the IR spectrum at pH = 0 (Figure 2) and the much weaker one in Raman (Figure 3) confirm the protonated state of the carboxyl group. The same can be concluded from the strong IR band at 1257 cm⁻¹, which can be assigned to ν C-O, in accordance with literature.^{23, 24, 26} In line with the pK_a of 1.8 of the carboxyl group the relative intensity of both bands decreases at pH = 1 and the bands disappear at pH > 2, illustrating deprotonation to CO₂⁻ and conversion to H₃His⁺. Simultaneously with the decreasing intensity of ν C=O and ν C-O in the IR spectra, the appearance of the anti-symmetric and symmetric C-O stretching vibrations of the CO₂⁻ group around 1620 and 1410 cm⁻¹, respectively, also marks the conversion from H₄His²⁺ to H₃His⁺. Referring to the general literature^{9, 10} both modes should show medium to high IR, but low Raman activity and indeed, as can be seen from Figure 2, a band arises in the IR spectrum around 1402 cm⁻¹ at pH = 2, which can be assigned straightforward to ν_s CO₂⁻.^{9, 10, 23, 26, 27} The vibration remains visible in IR and slowly increases up to 1416 cm⁻¹ at pH = 14. Assignment of the IR band at 1620 cm⁻¹ to ν_{as} CO₂⁻ seems obvious, but contrary to some reports^{23, 24, 27, 40} the peak cannot be attributed to ν_{as} CO₂⁻ solely, since a band at this position is also observed in the IR spectrum of the fully protonated form H₄His²⁺ at pH = 0. A plausible explanation is that ν_{as} CO₂⁻ coincides with

$\delta_{\text{as}} \text{NH}_3^+$, a vibration which is also expected to exhibit strong IR, but weak Raman activity around 1620 cm^{-1} .

Comparison of the IR spectrum at $\text{pH} = 0$ with those recorded at higher pH values reveals the appearance of a shoulder at the low frequency side of the 1620 cm^{-1} band at $\text{pH} = 2$. This shoulder increases in intensity at increasing pH. For that reason we assign the initial band maximum at 1620 cm^{-1} to $\delta_{\text{as}} \text{NH}_3^+$ and the low frequency shoulder at 1600 cm^{-1} to $\nu_{\text{as}} \text{CO}_2^-$. The correctness of this assignment is further evidenced by the increasing intensity of the latter absorption at higher pH. At $\text{pH} \geq 6$ $\nu_{\text{as}} \text{CO}_2^-$ becomes even more intense than $\delta_{\text{as}} \text{NH}_3^+$, which results in a red shift of the band maximum to 1600 cm^{-1} . In accordance with the pK_a value of 9.1 the NH_3^+ group becomes deprotonated at $\text{pH} > 9$ and consequently a contribution of $\delta_{\text{as}} \text{NH}_3^+$ is no longer visible in IR. The conversion from H_2His^0 to HHis^- is also marked by a considerable drop of $\nu_{\text{as}} \text{CO}_2^-$ from 1600 cm^{-1} to 1560 cm^{-1} and, as expected, this IR band remains present up to $\text{pH} = 14$ together with $\nu_{\text{s}} \text{CO}_2^-$ around 1410 cm^{-1} .

Next to the anti-symmetric bending vibration of the NH_3^+ group around 1620 cm^{-1} the protonated state of the primary amino group also seems to be correlated to the medium to strong IR band around 1530 cm^{-1} (Figure 2). Some papers report a band at this position to be mainly a C=C/C=N ring stretching vibration^{14, 28}, but in acidic and neutral environment we believe that the largest contribution to the observed band originates from $\delta_{\text{s}} \text{NH}_3^+$ for the following reasons: alike $\delta_{\text{as}} \text{NH}_3^+$ the frequency of the vibration shifts downwards on increasing pH and disappears in accordance with the pK_a at $\text{pH} > 9$. The absence of a Raman counterpart and the large bandwidth, probably as a result of hydrogen bonding interactions, are two other arguments. Finally, the correlation between $\delta_{\text{s}} \text{NH}_3^+$ and the presence of an IR band at 1530 cm^{-1} has been illustrated in literature by the disappearance of the band upon deuteration of the NH_3^+ group using glycine^{45, 46} and histamine⁴⁷ as model compounds.

It should be noted, that one might expect the appearance of the NH_2 scissoring vibration around 1600 cm^{-1} in the IR spectrum at $\text{pH} > 9$ simultaneously with the disappearance of the NH_3^+ related bands. Indeed, closer examination of the $\nu_{\text{as}} \text{CO}_2^-$ band at 1560 cm^{-1} on going from $\text{pH} = 10$ to 13 reveals some asymmetry at the high frequency side, but apparently the contribution is too weak to be observed as a separate band.

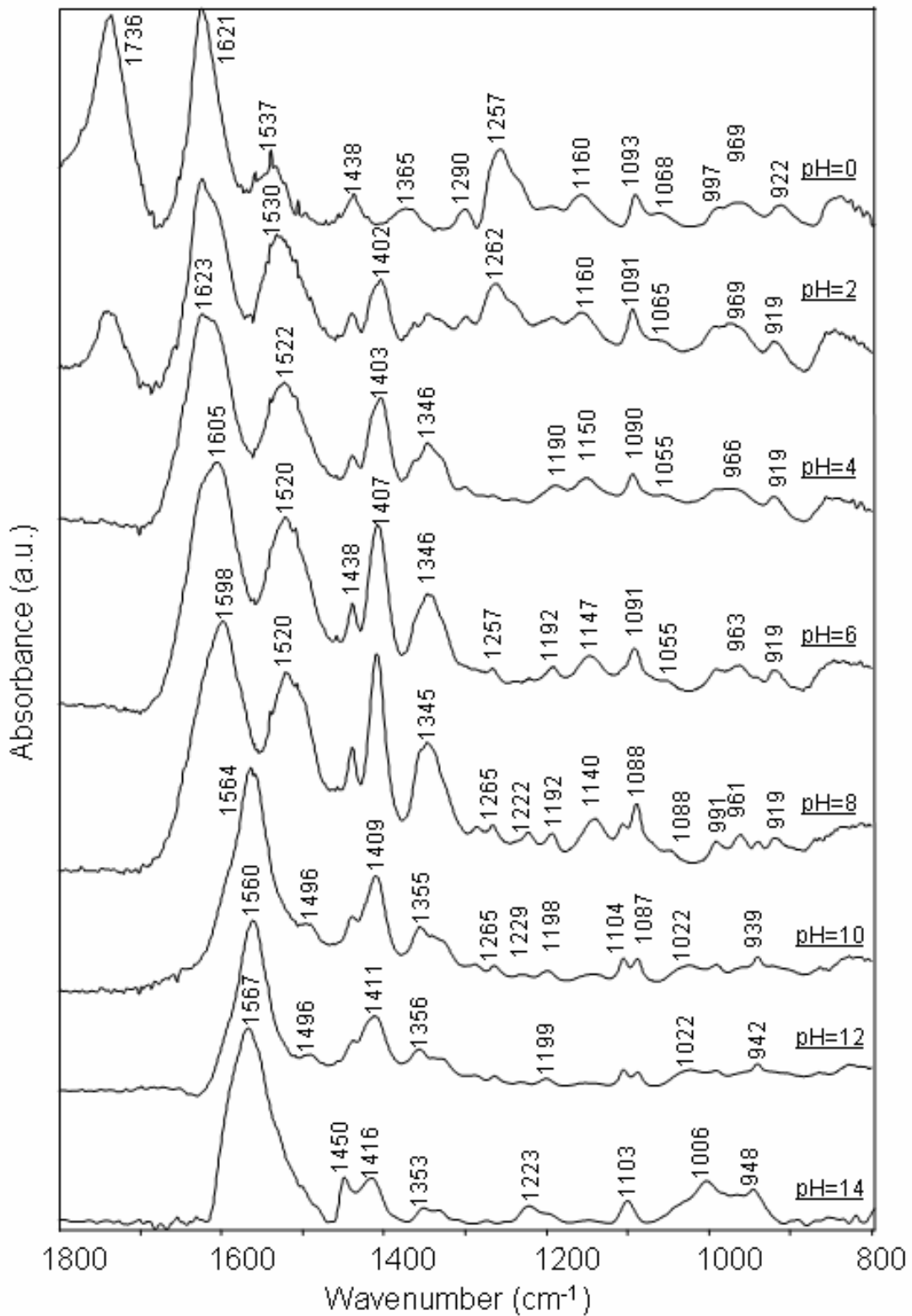


Figure 2: Infrared spectra of aqueous solutions of L-histidine at pH = 0, 2, 4, 6, 8, 10, 12 and 14.

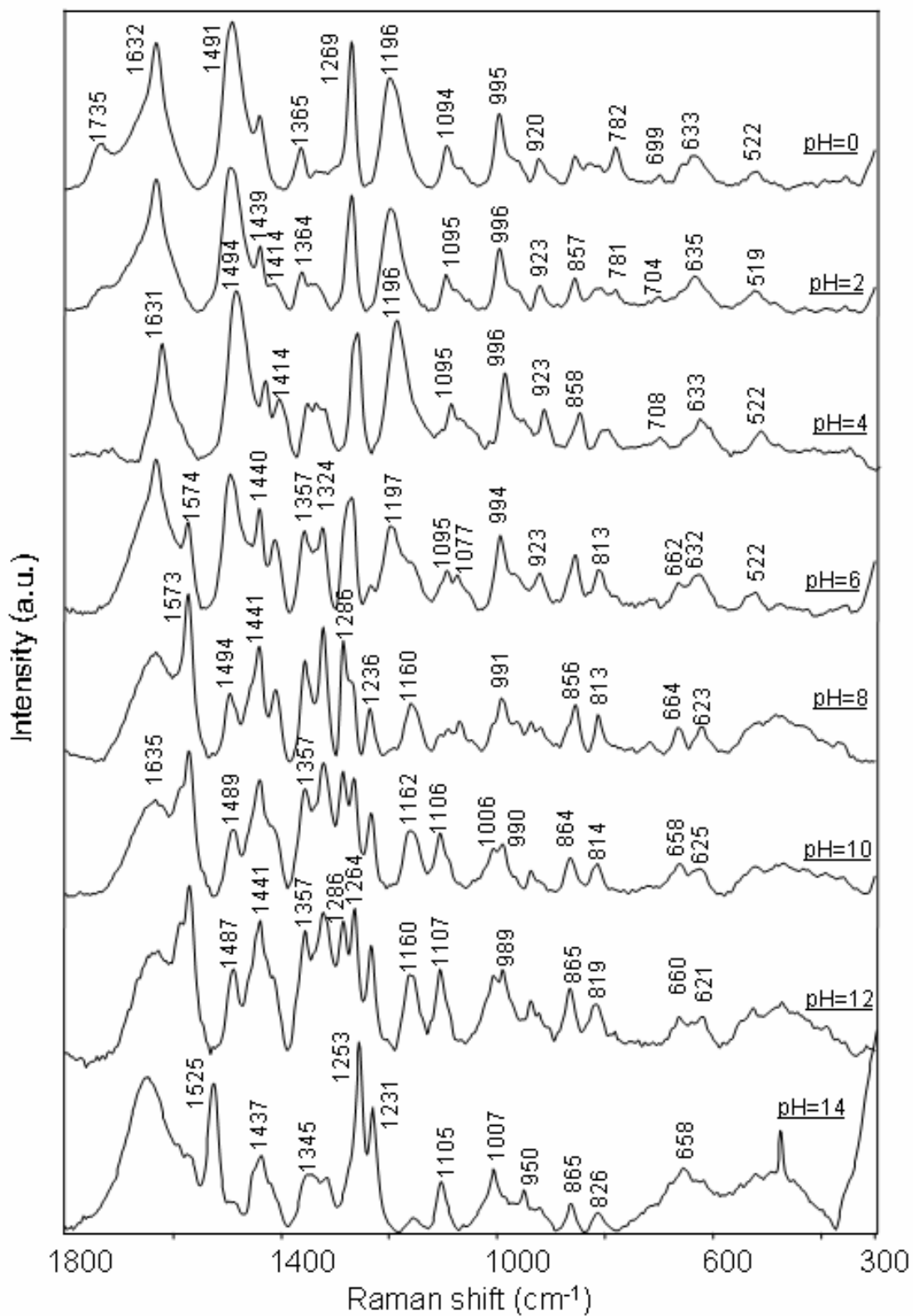


Figure 3: Raman spectra of aqueous solutions of L-histidine at pH= 0, 2, 4, 6, 8, 10, 12 and 14.

Table 1. Observed infrared absorption frequencies of aqueous solutions of histidine in the pH range 0-14. Coupled vibrations are indicated by “+” and coinciding modes by “/”. Wavenumbers with indication (s) are shoulders.

pH=0	pH=1	pH=2	pH=3	pH=4	pH=5	pH=6	pH=7	pH=8	pH=9	pH=10	pH=11	pH=12	pH=13	pH=14	Assignment	References
1736	1737	1738													v C=O	9,10,23,24,26
1621	1624	1623	1623	1623	1622	1623(s)	1620(s)	1620(s)	1598	1593	1594(s)				δ_{as} NH ₃ ⁺	9,10,26
		1606(s)	1610(s)	1611(s)	1609(s)	1605	1599	1598							v _{as} CO ₂ ⁻	9,10,27,28
1537	1535	1530	1522	1522	1521	1520	1520	1520	1517	1570	1564	1560	1564	1567	v _{as} CO ₂ ⁻	9,10,27,28
															v ring / δ_s NH ₃ ⁺	13,23,28
1438	1440	1438	1438	1438	1438	1438	1438	1439	1438	1438	1437	1437	1440	1450	δ N-H i.p./v C=N	15,16,18,21
	1402	1404	1403	1403	1404	1407	1408	1408	1408	1409	1410	1411	1415	1416	δ CH ₂	23,26,28,48,49
1365	1363(s)	1361(s)	1361(s)	1361(s)	1361(s)	1362(s)	1355(s)	1356(s)	1354	1355	1355	1356	1355	1353	v _s CO ₂ ⁻	9,10,23,26,27
															δ CH ₂ wagging	
															β NH ₃ ⁺	.
															β CH ₂	23,40,49
															δ CH ₂ / δ =C-H	23,27,28,47
1295(s)	1297	1297	1299	1300	1299										v C=N + δ =C-H	12,14,28,48
															v =C-N + δ C-H	6,12,14-18
															v =C-N + δ C-H	6,12,14,18,34
1257	1260	1262													v _s C-O	9,10,23, 24

1240(s)	1238(s)	1239	1239	1222	1222	1223	1229	1230	1230	1223	1230	1223	v C-N=C-C+ δ C-H	6,12,14,15,17,18
1190(s)	1190(s)	1192	1187	1191	1192	1192	1198	1199	1199	1198(s)	1198	1198(s)	δ -C-H (γ CH ₂)	-
1161	1160	1155	1152	1149	1147	1142	1144	1147	1152	1149	1151	1149	v =C-N / δ =N-H	13-17,26
1094	1094	1094	1093	1093	1106(s)	1106	1104	1104	1104	1103	1104	1103	v=C-N/ δ =C-H(N ⁺)	14-17,23,25-26
1068(s)	1066(s)	1065(s)	1055	1054	1055(s)	1049	1088	1087	1087	1088	1088	1088	v=C-N/ δ =C-H(N ⁺)	14-17,23,25-27
997	991	991	990(s)	990(s)	990	990	991	990	1024	1022	1022	1022	v C-N side chain	-
969	970	969	969	966	963	961	961	961	991	991	991	991	v =C-N / δ ring	16,25
													δ NH ₃ ⁺	-
922	920	919	919	919	940(s)	940	939	940	942	948	942	948	δ ring	12,15-18,27,29
856	851	855	855	855	850		922(s)						δ =C-H i.p.	12,30,49
													δ ring i.p./NH ₃ ⁺ rock	23,27,28,37

Table 2. Observed Raman shifts of aqueous solutions of histidine in the pH range 0 to 14. Coupled vibrations are indicated by “+” and coinciding modes by “?”. Wavenumbers with indication (s) are shoulders.

pH=0	pH=1	pH=2	pH=3	pH=4	pH=5	pH=6	pH=7	pH=8	pH=9	pH=10	pH=11	pH=12	pH=13	pH=14	Assignment	References
1735	1735														v C=O	9,10,23,24,26
1632	1632	1632	1631	1631	1631	1632									v C=C + v C=N	21,22,31,32,35
					1574(s)	1574	1573	1573	1573	1572	1572	1588	1588	1524	v C=C + v C=N(N ⁺)	15,16,18,31
1491	1492	1492	1494	1494	1492	1496	1494	1494	1494	1489	1489	1487	1492		v C=C + δ N-H(N ⁺)	15,16,18,31
1439	1439	1440	1439	1440	1439	1440	1441	1441	1441	1441	1440	1441	1440	1451	δ N-H i.p.	15,16,18,21
		1414	1413	1412	1414	1412	1412	1411	1412	1417(s)	1415(s)	1416(s)	1423	1423	δ CH ₂	23,28,48,49
1365	1362	1364	1363	1363	1363										δ CH-(CO ₂)	-
						1357	1356	1355	1356	1357	1356	1358	1357	1345	δ CH ₂ /v ring	16,24,34
															v C=N + v C-C(N ⁺)	16,23,28,34
1330	1332(s)	1335	1335	1338(s)	1340										v ring (C-N)	16
1325	1328	1329(s)	1328(s)	1328(s)	1327(s)										v ring (C-N)	16
						1324	1323	1322	1323	1322	1323	1321	1322	1317	δ CH ₂	16,18,34,48
															v C=N + v C-N(N ⁺)	16,23,24,34
1269	1269	1270	1269	1269	1269	1269	1268	1268(s)	1267	1264	1264	1264	1264		v =C-N + v C-C(N ⁺)	16,21
															δ =C-H(N ⁺)	16,21,34
														1253	δ =C-H	34

3.3.2 The side chain CH₂ and CH groups

The band around 1440 cm⁻¹ in both the IR and Raman spectra can be easily assigned to the CH₂ scissoring vibration.^{23, 26, 28, 48, 49} Since this alkyl group is neither subject to protonation nor very sensitive to solvent pH effects, its vibrational frequency and intensity are almost unaffected throughout the pH range from 0 to 14. According to literature CH₂ deformation vibrations also contribute to the complex IR bands between 1365 and 1325 cm⁻¹.^{23, 26, 28, 47-49} We partly agree on this assignment for the spectra recorded at low and high pH, but in view of the considerably increased intensity and broadening of the 1346 cm⁻¹ component at pH = 6 - 9 we also assume a substantial contribution of another vibration, which is related to the ionic state H₂His⁰. The large bandwidth points to a mode in which hydrogen bonding is involved, *e.g.* an NH₃⁺ wagging or a vibration that is related to the intra-molecular bridged tautomer of H₂His⁰, as depicted in Figure 1, but we have no further proof for this hypothesis. Furthermore, a ring =C-H deformation might contribute as well to the weak band around 1325 cm⁻¹.^{23, 27, 28} *Vice versa*, a contribution of the CH₂ wagging vibration to the Raman bands in the same region cannot be excluded^{18, 24, 34, 47, 48}, but as pointed out later, we believe that most of the intensity originates from skeletal modes.

3.3.3 The imidazole C=C and C=N vibrations

At low pH a sharp intense peak at 1632 cm⁻¹ is superimposed on the weak O-H deformation band of water in the Raman spectra. The peak starts to disappear at the pK_a value of the protonated imidazole group, *i.e.* at pH = 6 (see Figure 3) and it is therefore a good marker for the conversion of H₃His⁺ to the zwitterionic state H₂His⁰. Simultaneously, a peak at 1574 cm⁻¹ shows up and remains present up till pH = 13. Since both bands are strong in Raman, but virtually absent in IR, it seems obvious to assign the band at 1632 cm⁻¹ predominantly to the C=C stretching vibration of the protonated imidazole ring (conformers H₄His²⁺ and H₃His⁺) and the band at 1574 cm⁻¹ to the weakened ν C=C of the neutral and negatively charged ring (conformers H₂His⁰, HHis⁻ and His²⁻). In view of the relatively large sensitivity of the band to protonation, some coupling with the C=N stretching vibration will probably occur. The same holds for a second Raman band, that appears at 1588 cm⁻¹ at pH > 9 and remains present up till pH = 13. The simultaneous presence of two C=C bands can be

explained only by assuming the presence of two tautomeric forms of HHis^- as indicated in Figure 1, *i.e.* with either N^π or N^τ protonated. Indeed, as empirically demonstrated by Ashikawa and Itoh^{21, 22} and confirmed by others^{16, 18, 31}, the 1588 cm^{-1} band appears to be correlated to the N^π -protonated tautomer and the 1571 cm^{-1} one to the N^τ -protonated form. From the strong intensity of the latter compared to that of the 1588 cm^{-1} peak it can be concluded that protonation of N^τ is preferred over protonation of N^π , which is in line with the results of a temperature dependency study of histidine by means of NMR⁴⁵ and of 4-methylimidazole by Raman.¹⁶ The fact that the 1588 cm^{-1} component is even virtually absent below $\text{pH} = 9$ can be interpreted as the absence (or largely reduced presence) of the N^π protonated form of H_2His^0 . Furthermore, it can be concluded that the sensitivity of the C=C vibrational frequency for (de)protonation of N^π or N^τ points to either an inductive effect of N-protonation or to coupling of the C=C vibration with =C-N, =C-C or =C-N-H modes. According to DFT calculations on 4-methyl- and 4-ethylimidazole^{15, 16, 18} coupling of δ N-H and ν C=C indeed occurs, but only in the N^τ -protonated tautomer. This explains the difference in band position compared to the N^π -protonated form. Obviously, complete deprotonation of the imidazole ring ($\text{pK}_a = 14$) will affect the C=C vibration and as can be seen from Figure 3 the C=C region in the Raman spectra changes dramatically at $\text{pH} > 13$, which marks the conversion from HHis^- to His^{2-} . The C=C bands around $1570/1580\text{ cm}^{-1}$ disappear completely and a new strong band shows up at 1525 cm^{-1} . The drop in the vibrational frequency can be explained by a further decrease of the C=C bond strength, while the increased symmetry of the imidazole ring explains the strong Raman activity. It should be noted that the imidazole C=C vibration might exhibit some minor IR activity as well, but a contribution of $\nu_{\text{as}}\text{ CO}_2^-$ and $\delta_{\text{as}}\text{ NH}_3^+$ to the IR bands in the $1620\text{-}1570\text{ cm}^{-1}$ region is not observed.

Assignment of a band to the C=N stretching mode is more difficult due to the unlocalized character of this vibration, *i.e.* coupling to ν C=C, and the possible resonance structures of the imidazole ring in the ionic structures $\text{H}_4\text{His}^{2+}$, H_3His^+ and His^{2-} . According to literature the corresponding band around 1600 cm^{-1} should be medium in Raman and weak in IR, but no peak is found at this position that points towards the conversion of H_3His^+ to H_2His^0 or of HHis^- to His^{2-} .

3.3.4 Imidazole skeletal modes

The dominating peak in the Raman spectra at low pH is found at 1491 cm^{-1} , but there is no consensus on the assignment in literature. The band has been reported as an N-H in-plane bending²¹ and as a ring stretching combined with =C-H bending^{23, 29} for histidine and as a coupled ring δ N-H / ν C=N mode for 4-methyl- and 4-ethylimidazole.^{15, 16, 18} Coupling of vibrations undoubtedly plays a role and in agreement with literature^{15, 16, 18, 21} we believe the band to be predominantly an in-plane N-H bending / C=N stretching vibration for two reasons. Firstly, the band disappears upon deuteration, as shown by Toyoma *et al.*,¹⁶ which implies that the ring nitrogens are largely involved. Secondly, the largest Raman activity of the vibrations can be expected for the positively charged imidazole ring ($\text{H}_4\text{His}^{2+}$ and H_3His^+), as the ring is highly symmetrical due to protonation of both N^π and N^τ . The fact that the Raman intensity drops at $\text{pH} > 6$, upon partial deprotonation of the ring, and completely disappears at $\text{pH} = 14$, where both N^π and N^τ are deprotonated, is in line with this assignment. The same holds for the weak IR activity, as a band at the same position is only observed at pH 8 to 12.

Assignment of the Raman band at 1414 cm^{-1} to a coupled ring N-H bending / C-N stretching mode as indicated by the results of DFT calculations on 4-methyl- and ethylimidazole^{15, 18} is rejected as the band is still present when the ring is completely deprotonated, *i.e.* at $\text{pH} = 14$. Attribution to $\nu_s\text{ CO}_2^-$, as proposed in literature,^{24, 34, 35} is also discarded since the Raman shift is significantly higher than the position of this vibration in IR. On the other hand, the band arises at $\text{pH} = 2$ and remains present up to $\text{pH} = 14$ and hence a correlation to the deprotonated carboxyl group seems more obvious than to an imidazole ring vibration. For that reason we tentatively assign this band to a CO_2^- related mode without further detail on the type of vibration.

Several other bands, which are prominent in Raman but weak in IR, can be attributed to imidazole skeletal modes. In accordance with the results of normal coordinate analysis of 4-methylimidazole,¹⁶ we assign the intense pair of Raman bands around 1357 and 1324 cm^{-1} in the pH range 6-13 to coupled C=N and =N-C ring stretching vibrations, the high frequency one being characteristic for N^π protonation and the low frequency band for the N^τ -H form of the ionic states H_2His^0 and HHis^- . However, at lower pH (0-5), a Raman band is present at

1365 cm^{-1} , which must be due to another vibration in view of its shifted position and significant lower intensity. We reject the assignment of Garfinkel *et al.*¹⁹ of a $\nu_s \text{CO}_2^-$ because of the absence of a strong band in IR, but in line with the IR data, a CH_2 wagging is a plausible explanation. On the other hand, we believe that a ring stretching mode of the protonated imidazole ring^{16, 34} contributes to the observed band, as the presence of the peak appears to be correlated to $\text{H}_4\text{His}^{2+}$ and H_3His^+ . A similar explanation can be given for the Raman band at 1325 cm^{-1} . As pointed out above, this peak is intense at pH 6 to 13, but a weak band at the same position is also observed at other pH-values as well as in the IR-spectra. For that reason we also propose a contribution of a CH_2 deformation vibration next to the previously mentioned coupled $\text{C}=\text{N} / =\text{N}-\text{C}$ mode.^{16, 34} The weak Raman shifts between 1330 and 1347 cm^{-1} have not been referred to in literature. Band maxima are only clearly visible in the spectra of pH 0 to 5 and for these bands we propose a stretching vibration of the ring C-N bond with enhanced strength in the ionic states $\text{H}_4\text{His}^{2+}$ and H_3His^+ .¹⁶

It is generally agreed that the IR and Raman bands below 1300 cm^{-1} originate from coupled skeletal stretching and bending modes of C-N, C-C, N-H and C-H, which are, therefore, not well-localized. On the other hand, it is logical to assign the strong Raman band at 1269 cm^{-1} in acidic environment (pH < 6) to an imidazole ring breathing vibration,^{21, 22} regarding the high symmetry of the ring in the ionic forms $\text{H}_4\text{His}^{2+}$ and H_3His^+ . However, at pH > 3 a second band around 1285 cm^{-1} comes up and both bands mainly have been assigned to a ring type of $=\text{C}-\text{H}$ in plane bending by Stewart.³⁴ This is in line with the results of normal coordinate analysis of 4-methylimidazole^{14, 16} for the 1265 cm^{-1} peak, but the 1285 cm^{-1} band has been calculated as a coupled $\text{C}-\text{C} = / =\text{C}-\text{N}$ stretching vibration. The fact that both vibrations show only minor IR activity does not contradict these assignments. It should be noted, however, that the empirical correlation of the 1285 cm^{-1} band to the N^τ - and the 1265 cm^{-1} one to the N^π -protonated tautomeric form of H_2His^0 and HHis^- , as reported in the literature,^{16, 21} is only valid for the pH range 9 to 13. As a shoulder at 1285 cm^{-1} is already present at pH = 3, this implies that the bands are only useful as a marker for the conversion from one ionic state to another when the intensity is taken into account.

The Raman band at 1236 cm^{-1} , that appears at pH > 6, has been assigned to a coupling of $\nu_s \text{N}-\text{C}-\text{N}$ and an in-plane N-H bending by Ashikawa and Itoh,^{21, 22} while Majoube *et al.*¹⁴ suggested a ring $=\text{C}-\text{H}$ bending for 4-methylimidazole. The latter is partly in accordance with

Toyama *et al.*,¹⁶ who calculated the band to be an overlap of a =C-N stretching of the N^π-H tautomer and a =C-H bending of the N^τ-H counterpart. We follow this assignment up till pH = 13. However, our data show that a band at 1230 cm⁻¹ is also present at pH = 14, where the imidazole ring is unprotonated, which more or less excludes a nitrogen-involved ring vibration, at least for the ionic state His²⁻. For that reason we believe this band to originate from an in-plane =C-H bending in accordance with reference 14. The absence of a significant IR band is in line with this proposal. Literature assignments of the very weak IR bands that we observe in the same region are absent, probably due to the lack of intensity, but as the IR bands around 1284 and 1265 cm⁻¹ largely overlap with the positions found in Raman it seems obvious to follow the same assignments. Indeed, they probably concern coupled =C-N stretching modes¹⁵⁻¹⁸ and/or =C-H deformation modes,^{6, 12, 14} but in view of the weak intensities the usefulness as tautomer markers is poor.

The intense Raman band around 1196 cm⁻¹ at pH = 0 disappears at pH > 6, which makes it a good marker for H₄His₂⁺ and H₃His⁺. The high intensity points to a symmetrical mode of the double protonated imidazole ring, either as a type of ring breathing or a combination of ν_s N-C-N with an in-plane N-H bending.^{14, 21, 22} A band around 1196 cm⁻¹ is also observed in IR, but the intensity is low and the band is present throughout the pH range 0 to 14. Only one reference has been found in literature for an IR band at this position, *i.e.* at pH = 7.7, and it has been assigned to an in-plane ring deformation.²⁶ Contrary to what the authors report, we observe hardly any effect of the pH and for that reason we assume it is a pH-insensitive vibration side chain -C-H deformation, possibly a rocking CH₂ vibration. The weak IR band in the region 1160-1140 cm⁻¹ has not been mentioned either in papers on histidine and therefore we follow the assignment based on theoretical calculations on imidazole¹³ and 4-methylimidazole.¹⁴⁻¹⁷ Accordingly, we assign the band to a coupled ν =C-N / δ =N-H vibration of which the calculated potential energy distribution points to predominantly =C-N stretching. A band also shows up around 1160 cm⁻¹ in the Raman spectra at pH = 6, which considerably weakens at pH = 14. In view of this it can be regarded as a good marker for the ionic states H₂His⁰ and HHis⁻. At some pH values the difference between the IR and Raman band maxima is significantly larger than the instrumental resolution, which implies that principally two different modes are involved. In line with the

theoretical calculations, we assign the band to similar types of (coupled) ring =C-N stretching and/or =N-H bending vibrations.

The IR and Raman bands around 1106 and 1090 cm^{-1} exhibit more or less the same behavior in the sense that the former arises concomitantly in the IR and the Raman spectra at $\text{pH} > 6$, while the contribution at 1090 cm^{-1} is present from $\text{pH} = 0$ up to 13, in Raman as a shoulder and in IR as a separate band. Different from empirical correlations,²¹ *ab initio* DFT calculations and normal coordinate analysis on 4-methylimidazole¹⁵⁻¹⁷ indicate that the bands are mainly ring =C-N stretching vibrations coupled to the corresponding =C-H in-plane deformation. This is in accordance with the assignments proposed by others.^{14, 23, 25-27} Obviously, the intensities in IR and Raman differ due to different activities, but the fact that two peaks are present in the pH range of H_2His^0 and HHis^- ($\text{pH} = 6$ to 13) can be explained by the sensitivity of the imidazole nitrogen atoms to protonation. Hence, the small bands are useful as tautomer markers, particularly in IR; the 1105 cm^{-1} component representing the N^π -protonated form and the 1090 cm^{-1} one the N^τ -H form.^{15, 17, 25}

Assignments of the weak IR and Raman signals between 1070 and 1020 cm^{-1} have not been found in the literature for histidine- and imidazole-type of compounds. In contrast, for amino acids a band in this region is usually assigned to a C-N stretching vibration.^{9, 10} The position of the IR band suggests a correlation to the ionic form of histidine, as the downward ‘jumps’ in frequency from 1068 cm^{-1} ($\text{pH} = 0$) to 1055 cm^{-1} ($\text{pH} > 2$), 1048 cm^{-1} ($\text{pH} > 6$), 1022 cm^{-1} ($\text{pH} > 9$) and 1006 cm^{-1} ($\text{pH} = 14$) correspond surprisingly well to the different pK_a values. In view of the central position of the carbon atom attached to the primary amino group with respect to the different sites that can be protonated, we propose a side chain C-N stretching vibration, but further evidence is needed for a reliable assignment. In view of its position and intensity the IR band at 1006 cm^{-1} at $\text{pH} = 14$ can be used as a marker for the ionic state His^{2-} .

The Raman spectra show a peak of medium intensity at 995 cm^{-1} from $\text{pH} = 0$ to $\text{pH} = 13$ and a second band that arises as a shoulder at 1007 cm^{-1} at $\text{pH} = 8$ (Figure 3). The bands have been proposed as tautomer markers for the N^τ - and N^π -protonated forms of H_2His^0 and HHis^- , respectively.^{16, 21, 22} However, since the 995 cm^{-1} peak is also present at very low pH this correlation can only be valid for the 1007 cm^{-1} component. Both bands have been assigned to =C-H in-plane bending vibrations^{21, 22, 37} and ring deformations,²⁴ but it has been

demonstrated recently that the 995 cm^{-1} band is most likely a $=\text{C-N}$ stretching vibration coupled to a ring deformation.¹⁶ The simultaneous presence of a weak IR band at the same position throughout the pH range is in line with this assignment and not in contradiction with the less detailed description of a $=\text{C-N}$ stretching vibration²⁵ or a ring stretching mode.²³

The IR and Raman bands below 990 cm^{-1} are mostly weak and assignments are only indicative. The weak shoulder in Raman around 970 cm^{-1} at acidic to neutral conditions has not been assigned in literature, but based on the observations and calculations for 4-methylimidazole a coupled $=\text{C-N}$ stretching and ring deformation is a plausible explanation for this band.^{14-17, 37} The large width of the IR band at 960 cm^{-1} , particularly at low pH, points to a vibration that is sensitive to hydrogen bonding. As the band disappears at $\text{pH} > 9$, a deformation vibration of the NH_3^+ group is most likely causing this band. The usefulness of the band to mark conversion from HHis^- to His^{2-} is limited, because of its low intensity. The weak Raman and IR bands around 940 cm^{-1} that appear at $\text{pH} \geq 6$ are assigned to an in-plane ring deformation in accordance with the literature on histidine^{27, 29} and 4-imidazole,^{12, 15-18} but clearly different from the assignment of $\nu\text{ C-COO}^-$ for histamine.⁴⁷

The Raman band at 920 cm^{-1} has been assigned to a $=\text{C-H}$ deformation vibration,³⁰ but this study concerned histidine in the crystalline state. Suggestions for the origin of the peak in spectra of aqueous solutions have not been found. The results for imidazole also point to a ring deformation vibration¹² and regarding the weak intensity of the band in both IR and Raman this assignment seems plausible. Occasionally, very weak Raman bands also appeared in the region $910\text{-}890\text{ cm}^{-1}$, but the origin of these peaks is not clear.

The weak to medium Raman band between 865 and 855 cm^{-1} has been assigned to a coupled $=\text{C-C}$ stretching / ring deformation vibration,²⁴ which is not fundamentally different from the suggestions that have been given for the IR band at this position.^{23, 27, 28} Marti *et al.*²³ proposed a coupling of $\nu\text{ =C-C}$ with $\nu\text{ C-C-N}$ for the IR band, which seems reasonable since the vibrations show a higher Raman activity. However, the IR band is extremely broad and largely decreases in intensity on conversion from H_2His^0 to HHis^- ($\text{pK}_a = 9.1$). This points to a contribution of an NH_3^+ deformation mode, possibly a rocking vibration as reported by Torregiani *et al.*³⁷ for the histidine-related compound carnosine. For that reason we propose a combination of both vibrations for the IR band.

The Raman spectra show two weak bands at 808 and 824 cm^{-1} up till pH = 4, which turn into a single band at 820 cm^{-1} on increasing pH. The band has been attributed to a ring breathing vibration²⁴ and to a CO_2^- deformation vibration,³⁰ but we prefer the assignment to =C-H out of plane deformation vibrations,²⁸ as this is largely in line with the results of the theoretical studies on imidazole-related compounds.^{14, 15, 17, 18, 48}

The Raman shift at 782 cm^{-1} is only present up till pH = 2 and therefore it is a small but significant marker for the conversion of $\text{H}_4\text{His}^{2+}$ to H_3His^+ . Consequently, it is reasonable to assume that the band originates from a deformation vibration of the protonated carboxyl group, even though different assignments have been given to this vibration frequency in the literature.^{24, 36} Unfortunately, IR data could not be obtained to confirm our proposal because of the opaqueness of the ATR crystal below 800 cm^{-1} . At first glance, it also seems difficult to extract an unambiguous assignment for the weak Raman band that is observed in the pH range 0 to 8 between 699 and 718 cm^{-1} . Theoretical calculations on imidazole model compounds more or less agree on a combination of coupled ring =C-H bending modes,^{15, 17, 18} although some papers report on the involvement of ring puckering and a N-H wagging mode.^{13, 36} The large contribution of ring =C-H deformation vibrations, however, is not in contrast with the assignment of a ring deformation mode that has been proposed for the Raman spectra of histidine^{21, 24, 34} and therefore we assign the 718-699 cm^{-1} band accordingly. Similar arguments can be put forward for the Raman band that appears at 662 cm^{-1} , when the pH is raised to 6 or higher, and the peak between 633 and 621 cm^{-1} that is present from pH = 0 up to pH = 13. The results of theoretical calculations point to coupled skeletal modes such as β =C-H and ν =C-C, which can be summarized as ring deformation vibrations.^{14-17, 48} These assignments agree well with the assignments that are based on empirical data of histidine^{21, 23} and hence we assign both bands to skeletal ring deformation modes. Finally, assignment of the Raman band at 522 cm^{-1} to a COO^- deformation vibration, as proposed in the literature,^{24, 30} is doubtful, as a band at this position is also present at pH = 0. As we do not have a plausible alternative we leave this band unassigned.

3.4 Conclusions

The combined measurement of IR and Raman spectra of aqueous solutions of L-histidine over the pH range 0 to 14 provides a complete set of vibrational data that can be used to determine and monitor pH-induced structural changes. As such, the obtained information can be a useful contribution in the development of organic-functionalized inorganic substrates with histidine as well as other amino acid compounds. The data collection allows a thorough integrated interpretation of the complementary spectral data, which leads to a higher reliability of the peak assignments. As a result, we have been able to confirm, correct and add conclusions to previously published vibrational studies on histidine. Furthermore, we have demonstrated that the obtained set of vibrational data can be used to determine all possible states of protonation, *i.e.* $\text{H}_4\text{His}^{2+}$, H_3His^+ , H_2His^0 , HHis^- and His^{2-} . Besides, IR and Raman bands that represent the imidazole N^π - or N^τ - protonated tautomeric forms of H_2His^0 and HHis^- have been established. These bands, as well as the ones that can be used to mark the conversion from one state of protonation to another, are summarized in Table 3. The majority of the bands agrees well with the empirical and theoretical correlations that have been proposed in literature, but in some cases modifications appeared to be necessary.

Table 3. Characteristic experimental IR and Raman bands for the different ionic states and tautomer forms of L-histidine. The addition (s) means the band is a shoulder.

	$\text{H}_4\text{His}^{2+}$	H_3His^+	H_2His^0 ($\text{N}^\pi\text{-H}$)	H_2His^0 ($\text{N}^\tau\text{-H}$)	HHis^- ($\text{N}^\pi\text{-H}$)	HHis^- ($\text{N}^\tau\text{-H}$)	His^{2-}
IR	1736	1623	1600	1600	1560	1560	1567
	1621	1600(s)	1520	1520	1496	1496	1450
	1537	1520	1408	1408	1410	1410	1416
	1257	1403	1265	1286	1265	1286	
			1105	1088	1105	1087	1006
Raman	1735	1631	1575	1575	1588	1571	1525
	1632	1494	1494	1494	1488	1488	1253
	1494	1414	1357	1324	1357	1325	
	1196	1324	1286	1286	1265	1286	
	782	1196			1005	990	

3.4.1 $\text{H}_4\text{His}^{2+} \rightarrow \text{H}_3\text{His}^+$

The fully protonated state $\text{H}_4\text{His}^{2+}$ is easily determined from the strong IR and weakly Raman active C=O stretching band at 1736 cm^{-1} and the corresponding C-O(-H) stretching IR band at 1257 cm^{-1} . Furthermore, the IR band at 1537 cm^{-1} and a weak but characteristic Raman peak at 782 cm^{-1} can be used to determine the presence of $\text{H}_4\text{His}^{2+}$. Other Raman shifts at 1632 , 1494 and 1196 cm^{-1} are also prominent but these remain present in the spectra of H_3His^+ . In agreement with the pK_a value of the carboxyl group, the disappearance of the corresponding C=O and C-O(-H) bands around $\text{pH} = 2$ marks the conversion to H_3His^+ . Concomitantly, the IR active anti-symmetric and symmetric C-O stretching vibrations of the CO_2^- group arise; the first one as a shoulder around 1600 cm^{-1} on the 1623 cm^{-1} band and the second one as a band of medium intensity at 1403 cm^{-1} . Finally, the IR band at 1537 cm^{-1} shifts to 1520 cm^{-1} and in Raman weak bands show up at 1414 and 1324 cm^{-1} .

3.4.2 $\text{H}_3\text{His}^+ \rightarrow \text{H}_2\text{His}^0$

Conversion from H_3His^+ to the zwitterionic form H_2His^0 by partial deprotonation of the imidazole ring ($\text{pH} > 6$) is marked in the Raman spectra by the disappearance of the bands at 1631 and 1196 cm^{-1} and a large decrease in intensity of the peak at 1494 cm^{-1} . Simultaneously, a new Raman band appears around 1575 cm^{-1} , which indicates that the N^τ -protonated form is the dominant tautomer of H_2His^0 . The same can be concluded from the Raman band at 1286 cm^{-1} . The strong Raman bands at 1357 and 1324 cm^{-1} can be used as tautomer markers too, but only when taking into account their intensity and in combination with the 1575 and 1286 cm^{-1} bands, since other ionic forms also have peaks at these positions. In IR the shifted band maximum from 1623 to 1600 cm^{-1} and an increased intensity of the 1407 cm^{-1} peak can be regarded as good markers for the conversion to H_2His^0 . In addition, the presence of the N^τ -protonated tautomer can be derived from the weak bands at 1265 and 1105 cm^{-1} , while the bands at 1286 and 1088 cm^{-1} represent the N^π -protonated form.

3.4.3 $\text{H}_2\text{His}^0 \rightarrow \text{HHis}^-$

Upon further increasing the pH above 9, the conversion of H_2His^0 to HHis^- is reflected by a downward shift of the IR band at 1600 cm^{-1} to 1560 cm^{-1} . Besides, a weak but characteristic band appears at 1496 cm^{-1} , while the 1410 cm^{-1} peak decreases in intensity. The position of the IR bands at 1265 and 1105 cm^{-1} and the ones at 1286 and 1088 cm^{-1} that reflect the N^τ and N^π tautomers, respectively, remain virtually unaffected. In Raman two bands grow in at 1588 and 1265 cm^{-1} , more or less proportional to the conversion to HHis^- . The increasing intensity of the shoulder at 1005 cm^{-1} on the band at 990 cm^{-1} is due to the same effect; *i.e.* an increasing amount of the N^π -protonated form of HHis^- . The 1488 , 1357 and 1325 cm^{-1} bands remain constant.

3.4.4 $\text{HHis}^- \rightarrow \text{His}^{2-}$

The conversion from HHis^- to His^{2-} is marked by a considerable change in the Raman spectra, as all bands related to the N^τ - and N^π -protonated tautomers disappear. Firstly, the highly Raman active C=C stretching band around 1580 cm^{-1} shifts to 1525 cm^{-1} upon deprotonation of the imidazole ring. Secondly, the prominent bands at 1488 , 1286 and 1160 cm^{-1} disappear, whereas a strong peak at 1253 cm^{-1} arises. Finally, the IR band at 1560 cm^{-1} shifts slightly upwards to 1567 cm^{-1} and the weak band around 1496 cm^{-1} disappears. New IR peaks at 1450 and 1006 cm^{-1} further illustrate the conversion to His^{2-} .

References

- [1] L. Stryer, *Biochemistry*, W.H. Freeman and Company, New York, 1988.
- [2] E. Goormaghtigh, V. Cabiaux and J.-M. Ruysschaert, *Subcell. Biochem.* **23** (1994) 329.
- [3] E. Li-Chan, S. Nakai and M. Hirotsuka, *Prot. Struct.-Funct. Relat. Foods* **163** (1994) 163.
- [4] A. Barth, *Progr. Biophys. Mol. Biol.* **74** (2000) 141.
- [5] C. Jung, *J. Mol. Recogn.* **13** (2000) 325.
- [6] A. Barth, *Progr. Biophys. Mol. Biol.* **74** (2001) 141.
- [7] A. Barth and C. Zscherp, *Quart. Rev. Biophys.* **35** (2002) 369.
- [8] A. T. Tu, *J. Chin. Chem. Soc.* **50** (2003) 1.

- [9] F. R. Dollish, W. G. Fateley and F. R. Bentley, *Characteristic Raman Frequencies of Organic Compounds*, Wiley, New York, 1974.
- [10] D. Lin-Vien, N. B. Colthup, W. G. Fateley and J. G. Graselli, *The Handbook of Characteristic Infrared and Raman Frequencies of Organic Molecules*, Academic Press Inc., London, 1991.
- [11] P. Hudaky and A. Perczel, *J. Phys. Chem. A* **108** (2004) 6195.
- [12] S. Hashimoto, K. Ono, H. Takeuchi and I. Harada, *Spectrochim. Acta* **50A** (1994) 1647.
- [13] J. Sadlej, A. Jworski and K. Miaskiewicz, *J. Mol. Struct.* **274** (1992) 247.
- [14] M. Majoube, P. Millie and G. Vergoten, *J. Mol. Struct.* **344** (1995) 21.
- [15] K. Hasegawa, T. Ono and T. Noguchi, *J. Phys. Chem. B* **104** (2000) 4253.
- [16] A. Toyoma, K. Ono, S. Hashimoto and H. Takeuchi, *J. Phys. Chem. A* **106** (2002) 3403.
- [17] K. Hasegawa, T. Ono and T. Noguchi, *J. Phys. Chem. A* **106** (2002) 3377.
- [18] H. Gallouj, P. Lagant and G. Vergoten, *J. Raman Spectrosc.* **28** (1997) 909.
- [19] D. Garfinkel and J. T. Edsall, *J. Am. Chem. Soc.* **80** (1958) 3807.
- [20] F. P. Robinson and S. N. Vinogradov, *Appl. Spectrosc.* **18** (1964) 234.
- [21] I. Ashikawa and K. Itoh, *Biopolymers* **18** (1979) 1859.
- [22] I. Ashikawa and K. Itoh, *Chem. Lett.* **7** (1978) 681.
- [23] E. M. Marti, C. Methivier, P. Dubot and C. M. Pradier, *J. Phys. Chem. B* **107** (2003) 10785.
- [24] S. Martusevičius, G. Niaura, Z. Talaikyte and V. Razumas, *Vibr. Spectrosc.* **10** (1996) 271.
- [25] T. Noguchi, Y. Inoue and X.-S. Tang, *Biochem.* **38** (1999) 10187.
- [26] N. Wellner and G. Zundel, *J. Mol. Struct.* **317** (1994) 249.
- [27] R. H. Carlson and T. L. Brown, *Inorg. Chem.* **5** (1966) 57.
- [28] S. R. de Andrada Leite, M. A. Coutos dos Santos, C. R. Carobelli and A. M. Galindo Massabni, *Spectrochim. Acta A* **55** (1999) 1185.
- [29] D. S. Caswell and T. G. Spiro, *J. Am. Chem. Soc.* **108** (1986) 6470.
- [30] J. L. B. Faria, F. M. Almeida, O. Pilla, F. Rossi, J. M. Sasaki, F. E. A. Melo, J. M. Filho and P. T. C. Freire, *J. Raman Spectrosc.* **35** (2004) 242.
- [31] T. Miura, T. Satoh, A. Hori-i and H. Takeuchi, *J. Raman Spectrosc.* **29** (1998) 41.
- [32] T. Miura, A. Hori-i, H. Mototani and H. Takeuchi, *Biochem.* **38** (1999) 11560.
- [33] X. Zhao, D. Wang and T. G. Spiro, *Inorg. Chem.* **37** (1998) 5414.
- [34] S. Stewart and P. M. Fredericks, *Spectrochim. Acta A* **55** (1999) 1641.
- [35] M. Tasumi, I. Harada, T. Takamatsu and S. Takahashi, *J. Raman Spectrosc.* **12** (1982) 149.
- [36] L. M. Markham, L. C. Mayne, B. S. Hudson and M. Z. Zgierski, *J. Phys. Chem.* **97** (1993) 10319.
- [37] A. Torreggiani, M. Tamba and G. Fini, *Biopolymers* **57** (2000) 2000.

- [38] A.-M. Bellocq and C. Garrigou-Lagrange, *J. Chim. Phys. Phys. Chim. Biol.* **66** (1969) 1511.
- [39] I. N. Jakab, K. Hernadi, D. Méhn, T. Kollár and I. Pálinkó, *J. Mol. Struct.* **651-653** (2003) 109.
- [40] J. A. Cuadrado, W. Zhang, W. Hang and V. Majidi, *J. Environ. Monit.* **2** (2000) 355.
- [41] S. Hashimoto, K. Ono and H. Takeuchi, *J. Raman Spectrosc.* **29** (1998) 969.
- [42] J. G. Mesu, D. Baute, H. J. Tromp, E. E. van Faassen and B. M. Weckhuysen, *Stud. Surf. Sci. Catal.* **143** (2002) 287.
- [43] D. Baute, D. Arieli, F. Neese, H. Zimmermann, B. M. Weckhuysen and D. Goldfarb, *J. Am. Chem. Soc.* **126** (2004) 11733.
- [44] G. Tzvetkov, G. Koller, Y. Zubavichus, O. Fuchs, M. B. Casu, C. Heske, E. Umbach, M. Grunze, M. G. Ramsey and F. P. Netzer, *Langmuir* **20** (2004) 10551.
- [45] W. F. Reynolds, I. R. Peat, M. H. Freedman and J. R. Lyerla, *J. Am. Chem. Soc.* **95** (1973) 328.
- [46] F. Blomberg, W. Maurer and H. Ruterjans, *J. Am. Chem. Soc.* **99** (1977) 8194.
- [47] K. Furić, V. Mohaček, M. Bonifačić and I. Štefanić, *J. Mol. Struct.* **267** (1992) 39.
- [48] F. J. Ramirez, I. Tuñon, J. A. Collado and E. Silla, *J. Am. Chem. Soc.* **125** (2003) 2328.
- [49] S. Olsztynska, K. Komorowska, L. Vrielynck and N. Dupuy, *Appl. Spectrosc.* **55** (2001) 901.

Chapter 4

Unravelling the Coordination Chemistry and Molecular Structure of Cu^{2+} /Histidine Complexes in Aqueous Solution

Abstract

Aqueous solutions of Cu^{2+} /histidine (1:2) have been analysed in parallel with infrared (IR), Raman, ultraviolet-visible (UV/Vis), electron spin resonance (ESR) and extended X-ray fine structure (EXAFS) spectroscopy in the pH range from 0 to 10. The aim of the research was to unravel the mechanism that leads to the formation of the biologically highly important Cu^{2+} /histidine complexes and to elucidate the coordinating sites and the corresponding molecular structures. IR, Raman and UV/Vis spectroscopy have been carried out during titration experiments using small increments in pH to obtain detailed insight, while ESR and EXAFS measurements were performed at specific pH values. An integrated interpretation of all spectroscopic data has been used to extract a maximum of complementary structural information and to determine the relative abundance of the different complexes. The formation of seven different species has been proposed, of which several co-exist at specific pH values. At highly acidic conditions Cu^{2+} and histidine are present as free ions, but around pH = 2 coordination starts *via* the deprotonated carboxylic acid group. Most likely this results

in the intermediate species $\text{Cu}^{2+}[\text{H}_3\text{His}^+(\text{O}_c)]$ and $\text{Cu}^{2+}[\text{H}_3\text{His}^+(\text{O}_c)]_2$, which convert almost concomitantly to the bidentates $\text{Cu}^{2+}[\text{H}_2\text{His}^0(\text{O}_c, \text{N}_{\text{am}})]$ and $\text{Cu}^{2+}[\text{H}_2\text{His}^0(\text{O}_c, \text{N}_{\text{am}})]_2$, of which the latter is dominant at $\text{pH} = 3.5$. Coordination by the imidazole ring begins around $\text{pH} = 3$ and leads to the formation of the mixed tridentate complexes $\text{Cu}^{2+}[\text{H}_2\text{His}^0(\text{O}_c, \text{N}_{\text{am}})] [\text{HHis}^-(\text{O}_c, \text{N}_{\text{am}}, \text{N}_{\text{im}})]$ and $\text{Cu}^{2+}[\text{HHis}^-(\text{N}_{\text{am}}, \text{N}_{\text{im}})] [\text{HHis}^-(\text{O}_c, \text{N}_{\text{am}}, \text{N}_{\text{im}})]$ around $\text{pH} = 5$. It is demonstrated that coordination of the imidazole ring occurs predominantly *via* the N^π atom. At $\text{pH} > 7$ the bi-ligand tridentate complex $\text{Cu}^{2+}[\text{HHis}^-(\text{O}_c, \text{N}_{\text{am}}, \text{N}_{\text{im}})]_2$ is the major species having nitrogen atoms in the equatorial plane and oxygen atoms in axial position. At $\text{pH} > 10$ this complex becomes unstable and decomposes with the formation of a copper oxide/hydroxide precipitate. The overall results provide a consistent picture of the mechanism that drives the coordination and complex formation of the Cu^{2+} /histidine system. As a result, structural proposals from literature have been unambiguously confirmed, clarified or, in several cases, corrected.

4.1 Introduction

Copper is one of the most abundant transition metals present in living systems and Cu^{2+} ions are well-known to play a key role in the working mechanism of several important metallo-enzymes, such as nitrogenase, galactose oxidase and superoxide dismutase. A driving force in the activity of these enzymes is the folding of a peptide chain, which consists of amino acids, around the Cu^{2+} cation. Histidine (His) moieties are known to be of major importance in this process, as this type of N-coordinating ligand forms fairly stable complexes with the copper cation. In order to unravel the formation processes of these types of enzymes and to find the exact coordination geometry of the copper-histidyl moieties, a lot of research has been conducted in this area.¹⁻¹⁷

A wide variety of analytical tools has been applied to obtain this type of information directly from the enzyme systems, but the analyses are often hampered by interference of the protein matrix. As an alternative complexes of Cu^{2+} with amino acid ligands are used as model systems and this approach is even more interesting since complexes of Cu^{2+} with His can be used to mimic the working mechanism of copper enzymes. Another important motivation to study Cu^{2+} /His species is their expected role in the development of man-made

enzymes *via* functionalization of inorganic hosts, such as zeolites and clay minerals, with this type of complexes.¹⁸⁻²² Finally, as a spin-off, this type of research may provide fundamental knowledge on the role of metal/amino acid complexes as precursors in the origin of life on earth, particularly when performed at extreme pH values.

Elucidation of the coordination geometry of the Cu²⁺/His complexes, however, is not easy, since this amino acid ligand has four potential sites for (de)protonation and thus for metal binding, *i.e.* the carboxylate group (O_c), the primary amino group (N_a) and two different nitrogen atoms of the imidazole ring (N^π and N^τ). In principle, each of these sites can be involved in the coordination to Cu²⁺, which may result in mono-, bi- or tridentate binding forms. Besides, the state of protonation of the different sites, the way of coordination and the co-existence of several different complexes are all pH-dependent. Furthermore, the copper to His ratio, the Cu²⁺ concentration and the ionic strength of the solution are generally known to affect the structure of the complexes. In order to elucidate the molecular structure of Cu²⁺/His complexes and to obtain insight into the forces that drive anchoring of the metal ion many studies have been carried out since the late 1960's. In these studies, a wide variety of techniques have been used to obtain the desired information, ranging from spectroscopic techniques like circular dichroism,^{10, 23, 24} UV/Vis,^{10, 23-27} IR,^{3, 14, 24-31} Raman,^{3-5, 10, 13, 15-17, 31-33} ¹H-NMR,^{10, 30, 34-37} ¹³C-NMR,³⁴ ESR^{10, 25, 35, 38-45} and EXAFS^{6, 46} spectroscopy to potentiometric^{10, 24, 27, 47-51} and calorimetric⁵² experiments.

A variety of Cu²⁺/His complexes consisting of one or two central copper atoms has been proposed in these studies, with one or two His ligands in a mono-, bi- or tridentate coordination and neutrally, negatively or positively charged. However, despite all these efforts, controversies on the mode of His binding to Cu²⁺ and the geometrical structure of the different complexes still exist. As an example, a point of dispute is that Cu²⁺ prefers a square planar or highly distorted octahedral configuration, which would exclude coordination *via* more than two binding sites of the same His molecule.^{29, 51} Furthermore, Itabashi and Itoh³² reported the existence of four different species and stated that Cu²⁺ is bound predominantly as a glycine-like chelate *via* the deprotonated NH₂ group and the carboxylate group. In contrast, Kruck and Sarkar²⁷ suggested eight different complexes, of which several involve coordination of the imidazole nitrogens.

A major cause for the conflicting views is that conclusions are often based on only one

or two characterization techniques, occasionally combined with theoretical calculations. Moreover, the corresponding experimental conditions are usually different, as they have been optimized for a specific characterization technique. To mention a few examples, the weak scattering efficiency in Raman spectroscopy requires high copper concentrations, whereas the opposite is desired in UV/Vis because of the intense blue color of the complexes dissolved in water. Contrary, IR spectroscopic studies on aqueous systems are largely hampered by the interference of water absorptions. For that reason the preferred method for this technique is analysis after lyophilization, crystallization or the use of D₂O. Finally, (pulsed) ESR and electron-nuclear double resonance (ENDOR) studies have been carried out on frozen solutions at temperatures even down to 4 K.^{18, 38, 39, 41} Hence it is very difficult to compare data and to draw objective and integrated conclusions.

In our opinion a more successful strategy to gain more insight into the coordination chemistry of Cu²⁺/His complexes is to combine several complementary analytical techniques in one integrated approach, which allows analysis at more or less the same sample conditions. To our knowledge such a multi-technique approach has not been reported for Cu²⁺/His complexes so far. Five techniques that, within certain limits, meet the above mentioned requirements are IR, Raman, UV/Vis, ESR and EXAFS spectroscopy. As demonstrated in the previous chapter the integrated use of IR and Raman has proven to be an ideal tool to distinguish all possible states of protonation of His, while UV/Vis is the method of choice to determine the identity and the amount of the atoms that are coordinating to the central Cu²⁺ ion from the copper d-d transition band. In addition, ESR can be used to discriminate between coordination of oxygen and nitrogen in the equatorial plane of the complexes. Finally, EXAFS can supply information on the distance between the central copper cation and the oxygen and/or nitrogen atoms in the first coordination sphere and thus on changes in the local structure around the Cu²⁺ ion. Moreover, an important advantage of these characterization techniques is that they can be applied not only at physiological conditions, but also at more extreme pH values. For that reason we decided to carry out a systematic study, using this multi-spectroscopic approach, on Cu²⁺/His complexes in aqueous solutions that covers the widest possible pH range. As a result we expect that a more consistent picture will emerge on both the mechanism that drives the complex formation and the molecular structure of this very important Cu²⁺/His system.

4.2 Experimental

4.2.1 Chemicals and solutions

All chemicals were obtained from Acros Organics (Geel, Belgium). For each experiment solutions of L-histidine, $\text{Cu}(\text{NO}_3)_2 \cdot 3\text{H}_2\text{O}$ and CuCl_2 (all *p.a.* grade) were freshly made by dissolving each of the components in demineralized water at various concentrations. All solutions were prepared in a Cu^{2+} : His ratio of 1 : 2 and acidified by addition of HCl or basic by addition of NaOH in order to prevent interfering buffer absorption in the IR or Raman spectra. To minimize the reducing effect of the X-ray beam on the samples $\text{Cu}(\text{NO}_3)_2 \cdot 3\text{H}_2\text{O}$ was used as precursor salt instead of CuCl_2 and HNO_3 was used instead of HCl to adjust the pH for the EXAFS analyses.⁵³ Concentrations were 0.001 M (Cu^{2+}) for ESR, 0.01 M for EXAFS and UV/Vis and 0.25 M for IR, Raman and UV/Vis analysis. IR, Raman and UV/Vis measurements were carried out simultaneously with the same 0.25 M solution. Additional UV/Vis analyses of the 0.01 M solutions were performed to determine possible concentration effects and hence to facilitate comparison of the IR and Raman data with the results of the more diluted samples used for EXAFS and ESR. All experiments were done at ambient temperature (298 K) and a pH meter model PHM 210 from Radiometer Analytical (USA) was used to determine the pH values. In order to determine the stability of the Cu^{2+} /His complexes and the reversibility of the complexation process two titration experiments were carried out, monitored by IR and Raman spectroscopy. Firstly, titration was performed from pH = 0 up to pH = 12 and backwards and secondly from pH = 0 up to pH = 10 and backwards. For comparison also solutions containing copper glycine and copper histamine complexes were studied, as glycine and histamine are structural analogues of histidine.

4.2.2 Characterization

IR measurements during titration were performed at room temperature on an Autochem ReactIR-4000 system (Mettler Toledo) equipped with a Dicomp ATR probe and a

nitrogen-cooled MCT-detector. The sample compartment was flushed with dry air to reduce interference from H₂O and CO₂. For each spectrum 256 scans were accumulated at a data point resolution of 2 cm⁻¹ (optical resolution of 4 cm⁻¹). Spectral interpretation was carried out after subtraction of the spectrum of water at the corresponding pH as background.

Raman measurements were carried out on a Kaiser RXN spectrometer equipped with a 70 mW 532 nm diode laser for excitation, a holographic grating for dispersion and a Peltier cooled Andor CCD camera for detection. Scanning was performed *via* a 10 mm objective probe head that was mounted just above the surface of the solution. The solution was stirred and kept at room temperature during the measurements to prevent local heating, *i.e.* degradation of the sample. The detector pixel resolution was about 2 cm⁻¹ and 15 scans were accumulated for one spectrum at an exposure time of 30 s per scan. Subtraction of the water background has not been applied for the Raman spectra.

UV/Vis spectra of the aqueous solutions were measured from 50000 to 10000 cm⁻¹ (200 to 1000 nm) at a spectral resolution of 0.15 nm with a Cary 50 (Varian) equipped with a probe head that was connected to the spectrometer *via* optical fibers. The effective optical path length in the probe head was 2 mm for the 0.25 M samples, whereas the path length was 10 mm for the 0.010 M samples.

X-band ESR measurements were carried out on a Bruker ESP300 spectrometer and on a Bruker ESP300E spectrometer, both operating near 9.5 GHz. ESR spectra were recorded at room temperature, using 80 μL quartz capillaries as sample cells. Spectra were taken at pH values of 2.0, 2.9, 3.4, 4.4 and 7.3. An in-house developed computer program was used for simulation of the Cu²⁺/His spectra, taking into account the natural abundances of the ⁶³Cu and ⁶⁵Cu isotopes. The simulation is a sum over Lorentzians. The different widths of the copper hyperfine lines were taken into consideration by fitting the relaxation parameters α , β and γ , according to the formula $T_2^{-1} = \alpha - \beta m + \gamma m^2$. In this way the g- and A-values, together with the relative abundance of the different Cu²⁺/His complexes at various pHs, were determined.

X-ray absorption data were collected on beamline BM29 at the ESRF (Grenoble, France), which operates at 6 GeV with a typical beam current of 200 mA. The station was equipped with an Si(311) double crystal monochromator and ion chambers for measuring incident and transmitted beam intensities. Measurements were performed at the Cu K-edge (8979 eV) in transmission mode on samples at pH = 2.0, 2.9, 3.4, 4.4, 6.0 and 8.0 at room

temperature in a stainless steel cell (diameter of 2.5 mm) with kapton windows. Higher harmonic contributions were filtered out by detuning the Si crystals by 50%. A copper foil was applied to calibrate the energy of the monochromator. Several scans were averaged to improve the signal to noise ratio of the data. The XAFS data were processed using the suite of programmes available at Daresbury laboratory, namely EXCALIB (for converting the raw data to energy vs. absorption coefficient) and EXBROOK (for *pre*- and *post*-edge background removal) to obtain the normalized XANES part of the spectra and EXCURV98⁵⁴ in order to carry out EXAFS data analysis. EXAFS refinements were carried out on k¹-weighted spectra plotted over a k-range of 3-13.3 Å⁻¹, considering only single scattering paths. An amplitude reduction factor (S₀²) value of 0.9 obtained from fitting the Cu metal foil was also used in the analysis. Since the Cu-O and Cu-N bond distances and backscattering amplitudes are about similar it is difficult to distinguish between their respective contributions in the EXAFS. This is a particular problem for the Cu²⁺/His system, in which the two different atoms are coordinating in the same coordination shell. As the fitting of two shells with the respective atoms leads to unphysical results, the refinements were performed considering only a single shell of either Cu-O or Cu-N with the best fit to the data being determined by the R-factor (which is a measure of the goodness of the EXAFS fit).

4.3 Results

As described in the previous chapter, histidine in aqueous solution can be present in five different, pH-dependent states of protonation, *i.e.* H₄His²⁺, H₃His⁺, H₂His⁰, HHis⁻ and His²⁻ (Figure 1). In principle all four deprotonation sites are potential sites for metal coordination, but metal binding *via* the double deprotonated imidazole ring is generally rejected, because of the extremely high pK_a value of the ring (pK_a = 14). Furthermore, the ionic state H₄His²⁺ lacks a site available for coordination and this leaves, in principle, H₃His⁺, H₂His⁰ and HHis⁻ as possible ligating structures. On the other hand, the presence of two different nitrogen atoms in the imidazole ring also makes that H₂His⁰ and HHis⁻ can be present in two pH-dependent tautomeric forms.

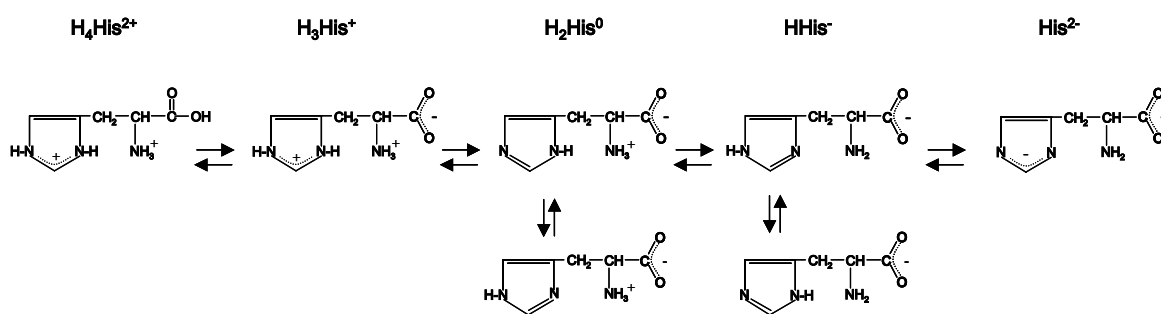


Figure 1. The different states of protonation of His as a function of the pH.

The commonly accepted notation to distinguish both nitrogen atoms is N^π for the one closest to the CH_2 group and N^τ for the other one. Unfortunately, a uniform nomenclature to describe the different Cu^{2+}/His complexes is absent in literature. In order to prevent further confusion, we define the state of protonation of His as described in Figure 1, while for the different metal binding sites the following notation is used: O_c for the carboxylate group, N_{am} for the amino group and N_{im} for the imidazole nitrogen atoms which can be denoted in more detail, if appropriate, as N^π and N^τ . Furthermore, it should be noted that at certain pH values two, three or even more different complexes can co-exist, which implies that spectra will not always correspond to single species. Obviously, this will hamper a straightforward interpretation and unambiguous structural elucidation. Spectral subtraction, deconvolution and difference spectroscopy have been proposed in literature to partially circumvent this problem, but in general these methods were found to be not very successful due to the lack of reliable standards and the large number of factors that may affect band positions and intensities. For those reasons these methods have not been applied here. Instead, in order to obtain as much information as possible, titration experiments have been carried out under well-controlled experimental conditions and, when appropriate, with increments of about 0.1 pH units between two subsequent measurements. As described in the experimental section, two different titration experiments were performed to check the reversibility of the complex formation. In the first experiment the pH of the Cu^{2+}/His solution was raised from pH = 0 up to pH = 12 and back, but we observed precipitation and a change of color of the solution above pH = 10. The same observations were reported by Itabashi and Itoh³² and in accordance with these authors we identified the precipitate as copper oxide/hydroxide. However, we also

noticed that the complex formation process was irreversible when passing pH = 12 and the same result was obtained when titration was started at pH = 12. Furthermore, precipitation turned out to proceed faster when the solution was not freshly prepared. These phenomena were not observed when a pH value of 10 was not exceeded and for that reason spectral data at a pH higher than 10 have been rejected. This implies that we also reject the existence of a binuclear Cu²⁺/His complex at pH > 10.5, as proposed in literature.²⁷

4.3.1 Vibrational spectroscopy

A three-dimensional plot of the IR spectra recorded during the titration experiment going from pH = 0.3 up to pH = 10 is presented in Figure 2.

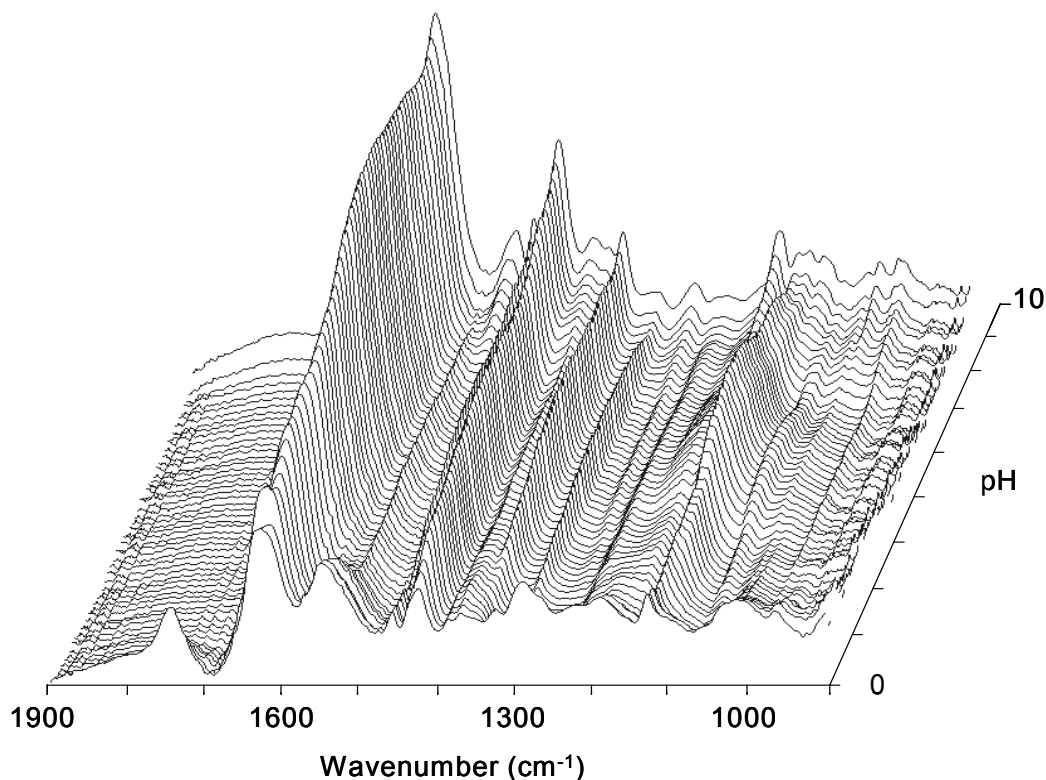


Figure 2. 3-D plot of IR spectra of Cu²⁺/His recorded during the titration experiment from pH = 0.3 to 10.

The graph illustrates the overall changes in the spectra as a function of the pH, but determination of small spectral changes requires a closer examination of individual spectra, as will be shown later. A similar 3-D representation of the Raman spectra turned out to be less

informative, as the band intensities drop dramatically at higher pH due to strong darkening of the solution. As an alternative a number of representative IR and Raman spectra have been extracted from the 3-D plots. These spectra are presented in Figures 3 and 4, respectively, and the positions of the most relevant bands have been indicated. In the discussion section assignments for these bands are proposed after spectral interpretation, taking into account IR and Raman selection rules and assignments from the work described in the previous chapter.⁵⁵ In addition, spectral details, which are relevant to determine coordination sites and the geometrical structure of complexes, will be presented.

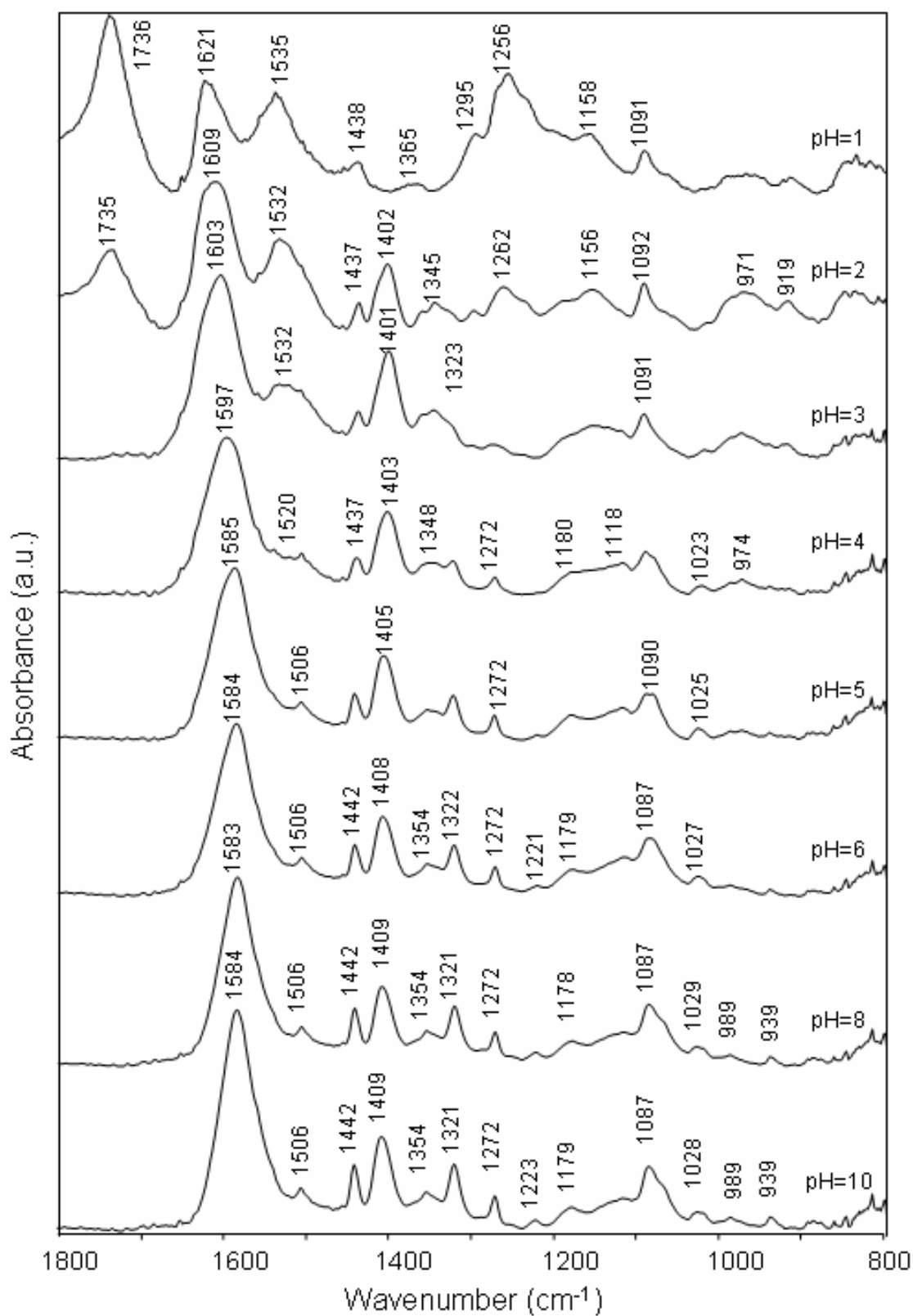


Figure 3. IR spectra of Cu²⁺/His solutions at pH = 1 (top) to pH = 10 (bottom).

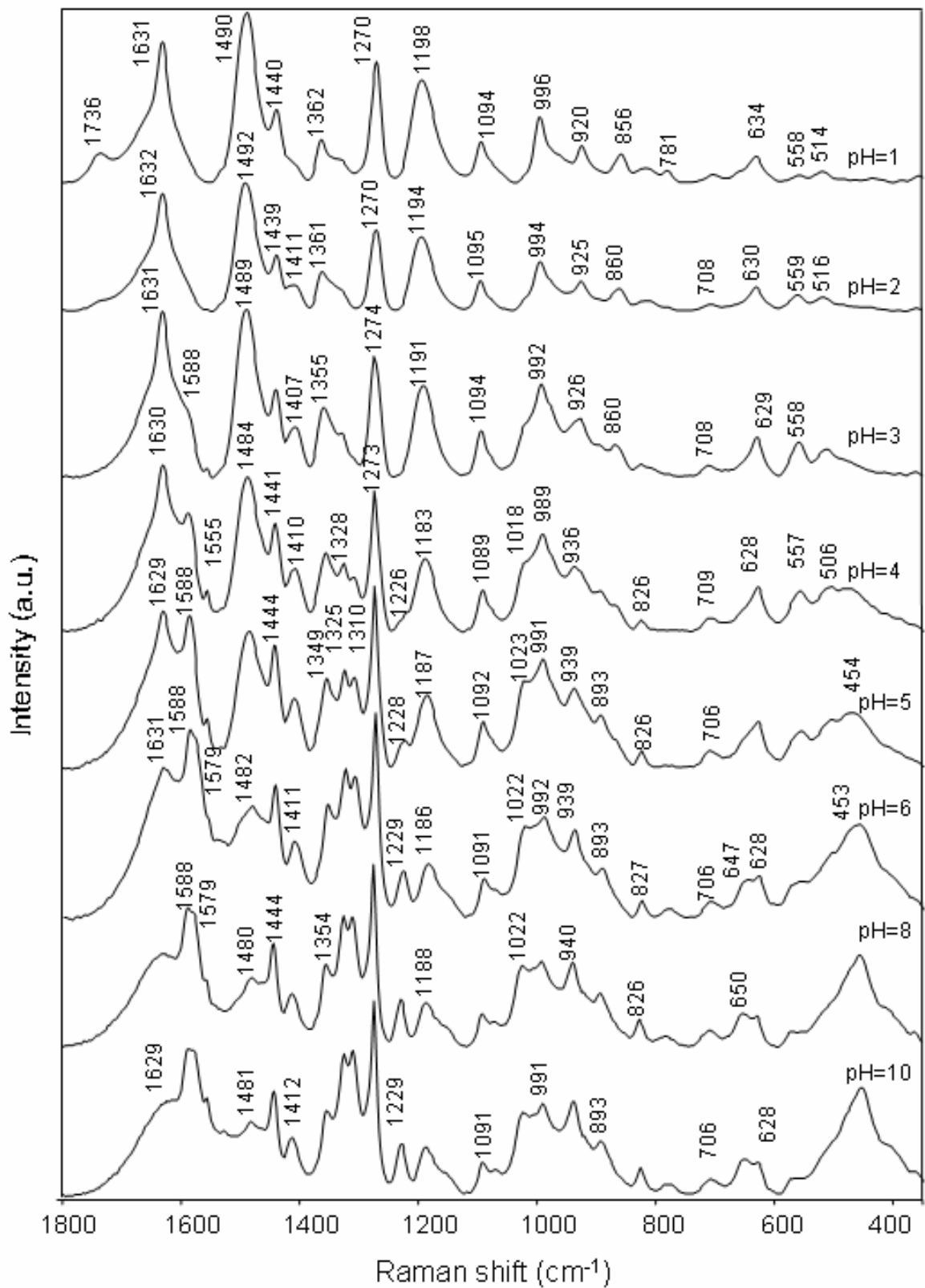


Figure 4. Raman spectra of $\text{Cu}^{2+}/\text{His}$ solutions at pH = 1 (top) to pH = 10 (bottom).

4.3.2 UV/Vis spectroscopy

The UV/Vis absorption spectra of aqueous 0.01 M Cu²⁺/His solutions as a function of the pH are presented in Figure 5. One absorption band is present in the visible part of the spectra, *i.e.* between 16500 and 12500 cm⁻¹ (600-800 nm), while strong absorption bands are present in the UV area of the spectra, *i.e.* around 35000 cm⁻¹ (285 nm). According to literature the band in the visible region can be assigned to the d-d transition of Cu²⁺.^{56, 57} The intensity of this d-d band increases with pH. Furthermore, the position of the band is not fixed, but with increasing pH it shifts to shorter wavelengths up to pH = 5, after which it shifts back to longer wavelengths for pH values > 5. Absorption in the UV-part of the spectrum is relatively small at low pH's, but increases very strongly with increasing pH. Besides, the absorption shifts to longer wavelengths.

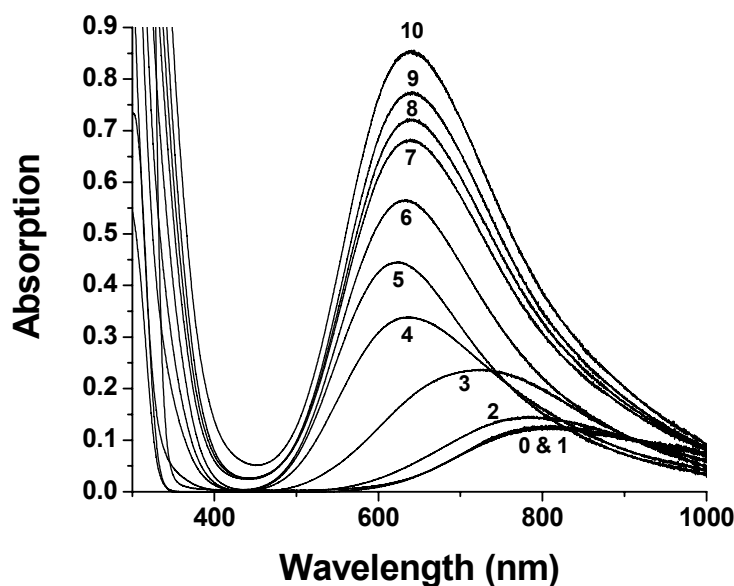


Figure 5. UV/Vis spectra of the 0.01 M Cu²⁺/His (1:2) solutions in the pH range 0-10 (pH values are indicated).

In order to determine the origin of the intensity increase and the shift in the position of the d-d absorption band the spectra of the Cu²⁺/His system were compared with the UV/Vis data of solutions containing Cu²⁺ complexes with histamine (Him) and glycine (Gly). These ligands have been chosen since they have only two coordinating sites, which are highly comparable to the ones of His, *i.e.* N_{am} and N_{im} for histamine and N_{am} and O_c for glycine. The coordination

geometry of these Cu^{2+} complexes is well-known and relatively simple, as both ligands possess only two potential sites for coordination to the Cu^{2+} cation. The spectra of the complexes were recorded over the same pH range and at the same concentration as for the $\text{Cu}^{2+}/\text{His}$ compounds. As illustrated in Figure 6, the position of the d-d transition band is the same for all three compounds at $\text{pH} = 1$, but different at higher pH values. Furthermore, all samples exhibit a considerable shift to shorter wavelength, but the band of $\text{Cu}^{2+}/\text{His}$ passes through a minimum at $\text{pH} = 5$, whereas the positions of the $\text{Cu}^{2+}/\text{Gly}$ and $\text{Cu}^{2+}/\text{Him}$ solutions stabilize when they reach the shortest wavelengths. However, after the maximum of the d-d transition band $\text{Cu}^{2+}/\text{His}$ reaches the shortest wavelengths, it starts to increase again with the pH up till $\text{pH} = 8$, after which it stabilizes.

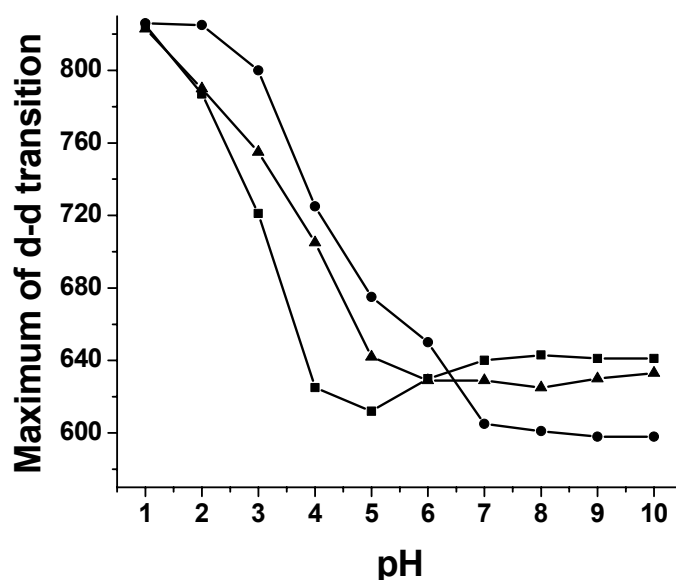


Figure 6. The maximum of the copper d-d transition as a function of the solution pH for 0.01 M aqueous solutions of $\text{Cu}^{2+}/\text{His}$ (-■-), $\text{Cu}^{2+}/\text{Gly}$ (-▲-) and $\text{Cu}^{2+}/\text{Him}$ (-●-) with $\text{Cu}:\text{L}=1:3$.

4.3.3 Electron spin resonance spectroscopy

The first derivative ESR spectra of the $\text{Cu}^{2+}/\text{His}$ solutions at different pH values are presented in Figure 7. As can be seen, the spectra recorded at pH values 4.4 and 7.3 show four hyperfine lines as expected for a Cu^{2+} ($I = 3/2$) complex in solution at room temperature. In

contrast, at least five hyperfine lines can be distinguished at pH = 2.0, 2.9 and 3.4, which indicates that more than one Cu²⁺ species must be present in the corresponding solutions.

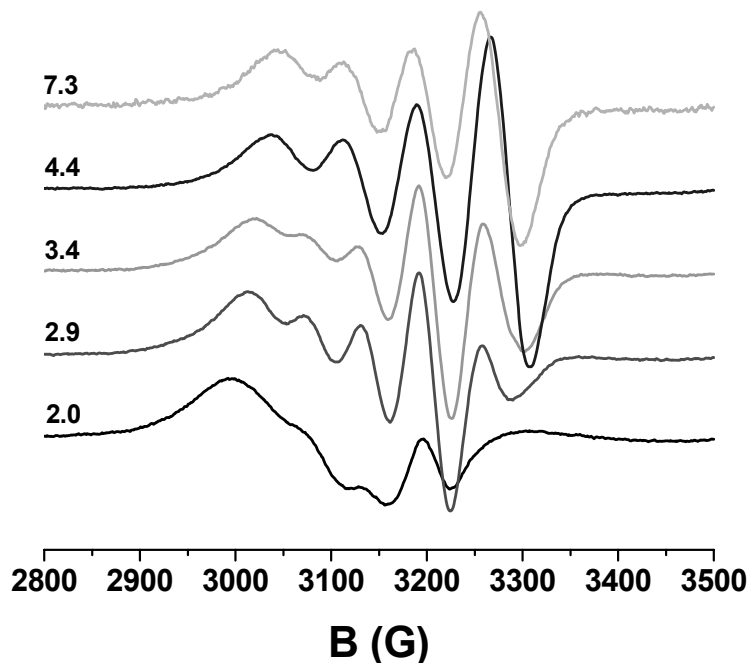


Figure 7. First derivative ESR spectra of 0.001 M Cu²⁺/His solutions at room temperature at pH values 2.0, 2.9, 3.4, 4.4, and 7.3.

In order to determine the ESR parameters of the different complexes and to determine their relative contribution spectrum simulations were carried out. The natural abundance of the copper isotopes and the different widths of the copper hyperfine lines were taken into consideration by fitting the relaxation parameters. As an example of the results obtained from these calculations, the simulated spectrum of the Cu²⁺/His solution at pH = 2.0 is shown in Figure 8, together with the experimental spectrum and the residual that remains after subtraction of the simulation from the experimental data. In addition, the results of the calculations obtained for all samples are summarized in Table 1. As can be seen from this table and Figure 8 the main contribution (85%) at pH = 2 originates from a complex with a relatively high g_0 value and a low A_0 value. Furthermore, the spectrum of a second species (15%) with a much lower g_0 value and a higher A_0 value is present, superimposed on the spectrum of the main complex. Finally, the spectrum of a third copper species is visible in the

residual. In the pH range 2.0-7.3 at least five different $\text{Cu}^{2+}/\text{His}$ complexes were found to be present in a relatively large abundance; each one characterized by its own g_0 and A_0 values. A rough estimate of the relative contribution of the different species in the various absorption spectra is also presented in Table 1.

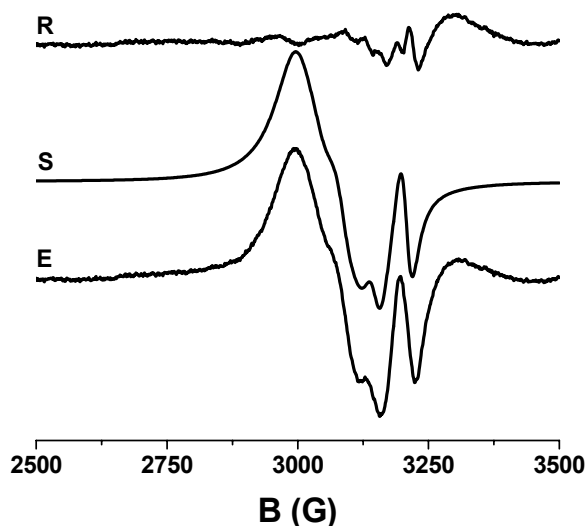


Figure 8. Overview of the experimental spectrum (E), the result of the simulation (S) and the residual (R) of the $\text{Cu}^{2+}/\text{His}$ solution at pH = 2.0.

Table 1: Optimized ESR parameters obtained from simulation of the $\text{Cu}^{2+}/\text{His}$ ESR spectra at different pH's. The species indicated c, e, f and h refer to the structures as depicted in Figure 13.

pH	Species	%	g_0 value	A_0 value
2.0	$\text{Cu}^{2+}(\text{H}_2\text{O})_6$	85	2.193	34
	c	15	2.154	58
2.9	c	75	2.154	58
	e	25	2.126	74
3.4	c	50	2.154	58
	e	50	2.126	74
4.4	f	90	2.119	72
7.3	h	90	2.120	64

4.3.4 Extended X-ray absorption fine structure spectroscopy

The X-ray absorption near edge structures (XANES) of the X-ray absorption spectra of four Cu²⁺/His samples are presented in Figure 9. Furthermore, the background subtracted EXAFS data (k^1 weighted) at various pHs (2.0, 2.9, 3.4, 4.4, 6.0, 7.3 and 8.0) are shown in Figure 10 and the associated Fourier Transforms (including both the real part and the transform envelope) are given in Figure 11.

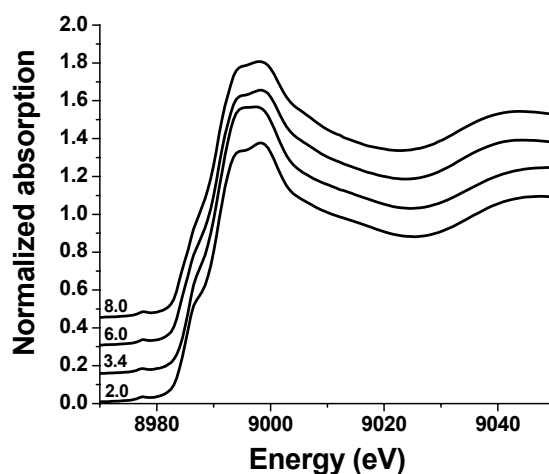


Figure 9. The XANES regions of the aqueous Cu²⁺/His solution at different pH values (indicated in Figure).

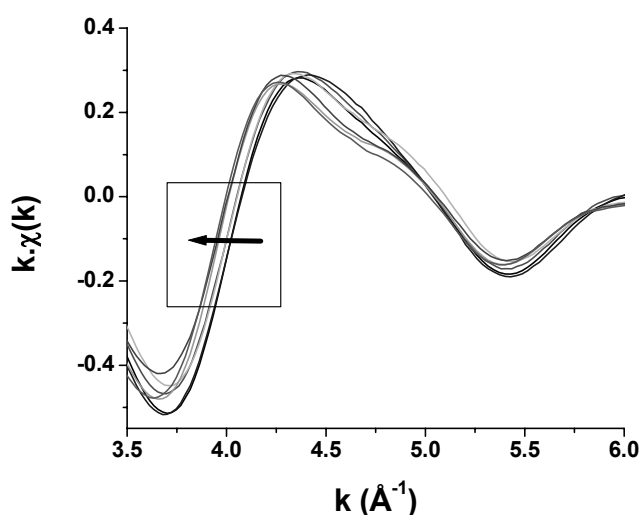


Figure 10. Phase-corrected k^1 -weighted EXAFS spectra recorded at increasing pHs. Note that data are k^1 -weighted in order to emphasise the changes that occur in the first shell of the Cu²⁺/His complex. The arrow indicates the trend in the data with increasing pH.

Although the differences between the spectra are very small, closer examination revealed a small shift for the start of the oscillations towards a lower k -space value with increasing pH. This has been indicated in Figure 10 by an arrow. Since the position of the Cu K-edge did not change, it is unlikely that this shift is due to a change in the oxidation state of copper. However, it is well known that such a shift, which is also associated with an increase in the EXAFS oscillation frequency, is related to an increase in the average absorber-scatterer distance.⁵⁸ Since the shift is observed at low k -space values it is clear that it corresponds to changes in the first $\text{Cu}^{2+}/\text{His}$ coordination shell. Indeed, the corresponding Fourier Transforms shown in Figure 11 confirm these observations, as the centroid position of the peaks from the real part of the transform is shifted towards higher r values (indicated by the arrow). Next, it is possible to conclude from a comparison of these positions that the bond distance sequence as a function of pH is $2.0 \approx 2.9 \approx 3.4 < 4.4 < 6.0 < 7.3 \approx 8.0$.

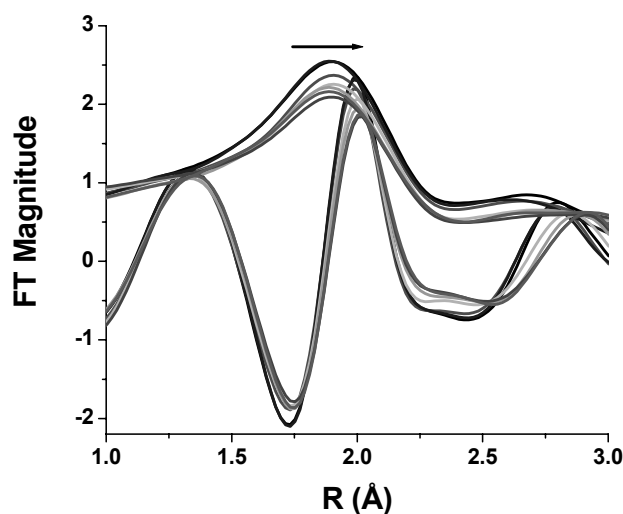


Figure 11. Associated Fourier Transforms for the data shown in Figure 10. Both the real part and the envelope are shown. The shift in the position of the centroid of the peaks in the real part indicates that the bond distance between copper and its nearest neighbours follows the trend in pH: $2.0 \approx 2.9 \approx 3.4 < 4.4 < 6.0 < 7.3 \approx 8.0$.

Fitting of the EXAFS data was also performed and the results obtained are shown in Table 2. Most notably, the best fit for the first shell for samples between $\text{pH} = 2.0$ and $\text{pH} = 3.4$ is obtained with 4 oxygen atoms at a distance of 1.95 \AA . At $\text{pH} = 4.4$ this distance has increased to 1.96 \AA , although a tendency towards under-coordination ($\text{CN} < 4.0$) was

observed. This finding may reflect a gradual increase in the number of nitrogen atoms present in the first coordination sphere, which might prevent sensible refinement parameters from being obtained. Indeed for pH = 6.0, 7.3 and 8.0 better r values were obtained when considering 4 nitrogen atoms as nearest neighbours at a distance of 1.99 – 2.00 Å. Whilst we note that the error in the determination of bond distances by fitting the EXAFS is *ca.* 0.02 Å (1%),⁵⁹ it is clear that the parameters derived by this process follow closely the variation observed in r- and k-space shown in Figures 10 and 11. This suggests that the refined differences of 0.01 Å observed between pH = 3.4, 4.4, 6.0 and 7.3, respectively, are real and not an artefact of the data fitting procedure. The observed Debye-Waller factors are typical for these species in solution.⁶

Table 2. Parameters derived from a 1st shell analysis of k¹-weighted EXAFS data.

pH	r (Å)	CN	Scatterer	$\sigma^2(\text{Å}^2)$	E _f
2.0	1.95	4.3	O	0.015	0.59
2.9	1.96	3.9	O	0.013	0.00
3.4	1.95	4.4	O	0.014	0.93
4.4	1.96	3.7	O	0.013	-0.66
6.0	1.99	4.4	N	0.012	1.19
7.3	1.98	4.0	N	0.010	-0.08
8.0	1.99	4.4	N	0.015	1.27

r(Å) = average 1st shell distance, CN = coordination number, $\sigma^2(\text{Å}^2)$ = Debye-Waller factor, E_f = Fermi energy.

4.4 Discussion

A large amount of spectral data, covering a variety of spectral changes as a function of pH, has been obtained from the different experiments. In order to systematically relate these data to (changes in) the geometrical structures of Cu²⁺/His complexes the results will be discussed in sub-sections that represent the most important pH ranges.

4.4.1 pH range 0 - 2

The IR and Raman spectra of the Cu²⁺/His solutions recorded up to pH = 1.8 appeared to be virtually identical to the ones obtained from the solution containing only His at the same

highly acidic conditions. Besides, as can be seen in Figures 3 and 4, respectively, the relatively high intensity of the ν C=O band at 1736 cm^{-1} in IR and Raman as well as the C-O(-H) stretching band in IR around 1257 cm^{-1} confirm that the carboxyl group is largely protonated in accordance with the pK_a value of 1.8 of this structural element. It implies that, under these conditions, His is exclusively present as a free, non-coordinated ligand in the double protonated ionic form, $\text{H}_4\text{His}^{2+}$, and thus complex formation does not occur. This is confirmed by the UV/Vis data, since the copper solutions with His, Him and Gly exhibit the same band position and intensity at $\text{pH} = 2$. The position of the d-d transition and its intensity are characteristic for copper surrounded by oxygen atoms. This is a clear indication that Cu^{2+} is present as a free, non-bonded ion, *i.e.* as a hexa-aqua complex. The same conclusion can be drawn from the ESR data. It is known that the effect of the nuclear spin of Cu^{2+} on the unpaired d-electron will be larger when the density of the electron at the position of the copper nucleus increases. When only oxygen atoms are coordinating, the density of the unpaired paramagnetic electron at Cu^{2+} is at its minimum and this is accompanied by a relatively high g- and low A-value compared to coordination by N-atoms. The simulation of the ESR spectrum of the $\text{Cu}^{2+}/\text{His}$ solution at $\text{pH} = 2$ indicates an 85% abundance of a complex with the relatively lowest A- and highest g-values (Table 1). From literature it is known that these g- and A-values are characteristic for the copper hexa-aqua complex.⁶⁰ This confirms the outcome of the other characterization techniques, which state that the copper hexa-aqua complex is the main species present at $\text{pH} < 2$. In accordance with these results, a perfect EXAFS fit is obtained when four oxygen atoms from water are assumed to be present in the first shell of the equatorial plane at a distance of 1.95 \AA . This distance is in accordance with the literature on studies on the structure of the copper hexa-aqua complex.⁶¹

4.4.2 pH range 2 - 4

On increasing the pH, the first differences compared to the IR and Raman spectra of free His are observed at about $\text{pH} = 2$. This indicates that complex formation starts around this pH value. The changes in the IR vibrations are well illustrated by the spectra recorded during titration from $\text{pH} = 1.95$ to $\text{pH} = 3.55$, as shown in Figure 12. Obviously, the intensity of the CH_2 scissoring band at 1440 cm^{-1} remains the same, but the C=O stretching band at

1736 cm⁻¹ disappears completely. Concomitantly, two bands increase in intensity, *viz.* the symmetric stretching vibration of the CO₂⁻ group at 1402 cm⁻¹ and the anti-symmetric analogue that is part of a combined absorption band around 1610 cm⁻¹. These changes reflect the deprotonation of the carboxyl group at increasing pH and as such, this behaviour is identical to what we observed for free His.⁵⁵

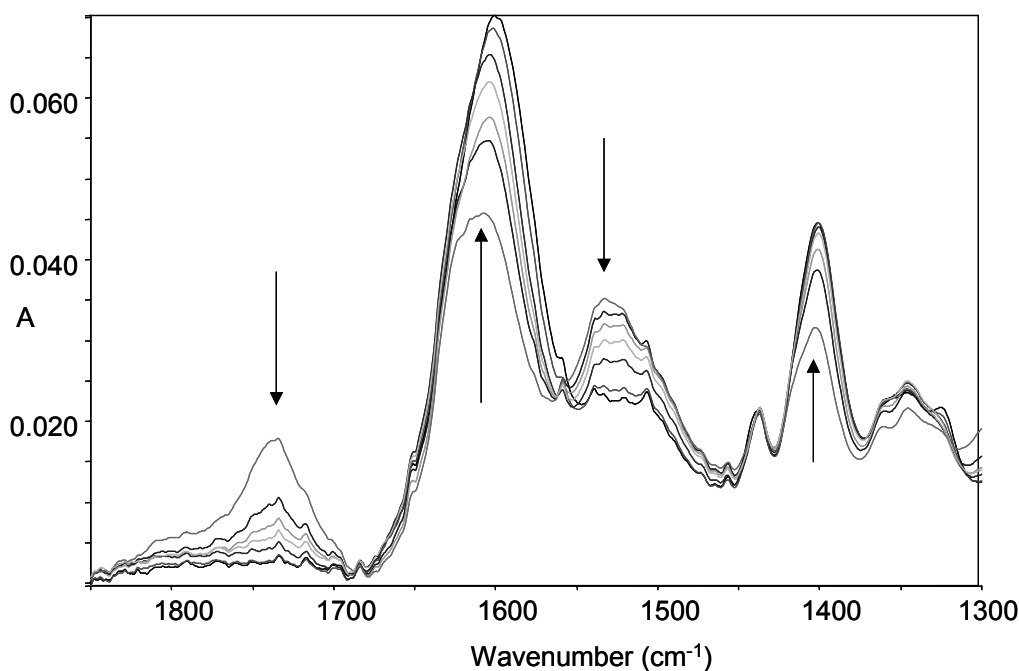


Figure 12. IR spectra of aqueous solutions of 0.25 mM Cu²⁺ / His at pH 1.95 to 3.55. The arrows indicate the increasing (↑) and decreasing (↓) intensities at increasing pH.

However, the position of the ν_{as} CO₂⁻ band is about 10-15 cm⁻¹ lower than we determined in the spectra of free His recorded at the same pH values. Although a part of this shift can be attributed to deprotonation of the amino group, as will be pointed out later, the large downward shift must be the result of coordination of the carboxylate oxygen atoms to the Cu²⁺ ion.⁶² The same conclusion has been reported by Kruck and Sarkar²⁷ from the intensity decrease of the 1736 cm⁻¹ band at pH = 2.5 upon addition of Cu²⁺, but it also illustrates that the conclusion of a Cu²⁺/His complex with a protonated carboxyl group as proposed by Meyer and Bauman⁵⁰ is wrong. In accordance with literature,⁶³ the effect of metal coordination on ν_{s} CO₂⁻ around 1402 cm⁻¹ is much smaller. The presence of a Raman shift around 560 cm⁻¹ at pH > 2 has been proposed as additional evidence by Itabashi and Itoh

³² and the band has been assigned to an out of plane bending mode of equatorial Cu-bound CO_2^- . Indeed, as can be seen from Figure 4, a Raman band is observed at 559 cm^{-1} at $\text{pH} = 2$, which rapidly increases in intensity at higher pH. However, it should be noted that a weak band at this position is also present in the spectrum at $\text{pH} = 1$, but this weak band possibly originates from another vibration. In principle, these observations point to the formation of complexes of the type $\text{Cu}^{2+}[\text{H}_3\text{His}^+(\text{O}_c)]$ and $\text{Cu}^{2+}[\text{H}_3\text{His}^+(\text{O}_c)]_2$, as depicted in Figures 13a and 13b, but closer examination of the IR spectra in Figure 12 shows that the intensity of the IR band at 1535 cm^{-1} decreases rapidly too on raising the pH to 3.55. Referring to the vibrational study on His,⁵⁵ this absorption originates from the symmetric bending vibration of the protonated amino group ($\delta_s \text{NH}_3^+$), which implies that the observed intensity decrease must be the result of deprotonation of this structural element. Regarding the pK_a value of 9.1 of this amino group, it can only be concluded that deprotonation must be the result of coordination of N_{am} to Cu^{2+} . The same can be concluded from the absorption band around 1610 cm^{-1} . The observed band consists of a peak from $\delta_{\text{as}} \text{NH}_3^+$ at about 1620 cm^{-1} that partly overlaps the absorption of $\nu_{\text{as}} \text{CO}_2^-$ around 1600 cm^{-1} . Upon increasing pH, the contribution of $\delta_{\text{as}} \text{NH}_3^+$ to the summed intensity of the observed band decreases and as a result the band maximum shifts to lower wavenumber and $\nu_{\text{as}} \text{CO}_2^-$ becomes the dominating component. In principle, one might expect the appearance of an NH_2 scissoring vibration in the same region; but as for the ionic states HHis^- and His^{2-} of free His, this absorption is probably weak or it coincides with $\nu_{\text{as}} \text{CO}_2^-$. Either way, the observed spectral changes can only be explained by assuming coordination of N_{am} to Cu^{2+} , which eliminates the dominating presence of a complex with $(\text{O}_c, \text{N}_{\text{im}})$ coordination at this pH, as proposed in several literature reports.^{30,36,51,64} It follows that the complexes must convert practically instantaneously via a monodentate complex with O_c to a bidentate complex with O_c and N_{am} as the coordinating anchors. Clear vibrational spectroscopic differences between the complexes with one or two His ligands cannot be expected since the coordination and the structure of both ligands are largely the same and hence it is not possible to draw quantitative conclusions on their relative abundance. Most likely, in accordance with Itabashi and Itoh,³² the glycine-like form with one ligand, $\text{Cu}^{2+}[\text{H}_2\text{His}^0(\text{O}_c, \text{N}_{\text{am}})]$, as depicted in Figure 13c, will be the major species at $\text{pH} = 3$.

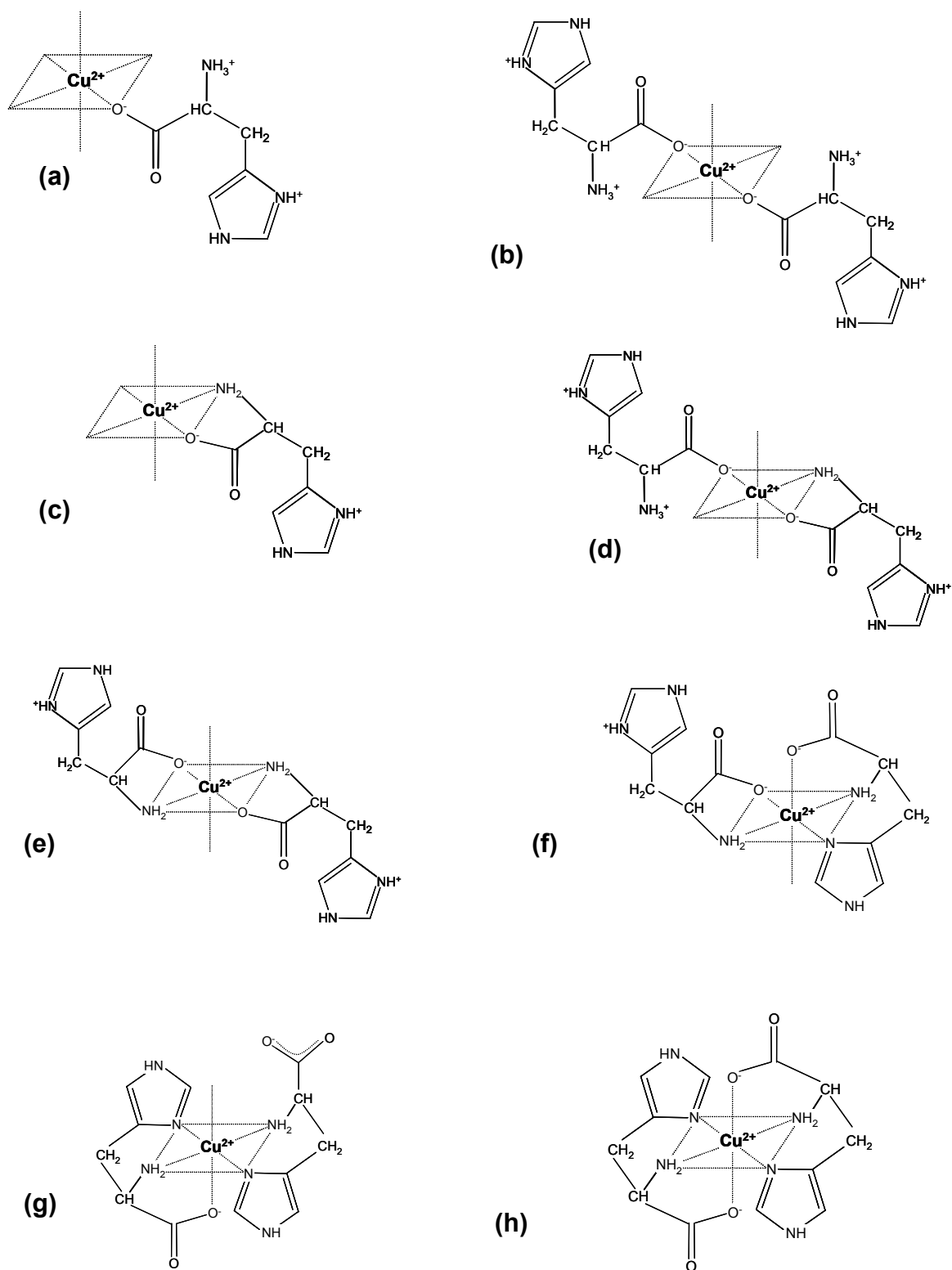


Figure 13. Proposed molecular structures of Cu^{2+} /His complexes at different pH values in the pH range 0 - 10. Coordination sites not coordinated by His are occupied by H_2O .

However, since all bands related to C=O (1736 cm^{-1}) and NH_3^+ (1535 cm^{-1}) have virtually disappeared at $\text{pH} = 3.5$, it is evident that free His is practically absent at this pH and as a result the complex with two His ligands, $\text{Cu}^{2+}[\text{H}_2\text{His}^0(\text{O}_c, \text{N}_{\text{am}})]_2$, represented in Figure 13e, must be the predominant structure at this pH. It is reasonable to assume that the formation of this species will proceed *via* the intermediate form $\text{Cu}^{2+}[\text{H}_2\text{His}^0(\text{O}_c, \text{O}_c, \text{N}_{\text{am}})][\text{H}_3\text{His}^+(\text{O}_c)]$ (Figure 13d), but the lifetime of this complex will be negligibly short.

The shift in equilibrium from a complex with one His ligand to a structure with two His molecules, as well as the nature of the coordinating groups, can also be observed from the UV/Vis spectra. The position of the Cu^{2+} d-d transition band is primarily defined by the physical properties of the coordinating atoms, the relative number of these coordinating atoms and the distance between these atoms and the Cu^{2+} ion. The higher the amount of nitrogen atoms in the equatorial plane (compared to oxygen atoms, either originating from the carboxyl group or from water molecules), the more the band maximum shifts to higher energies (lower wavelengths). Since EXAFS analysis reveals that there is no change in distance of the first coordination sphere (Table 2), the observed shift points to an increasing amount of coordinating nitrogen atoms in the equatorial plane. Furthermore, as can be seen in Figure 5, on increasing the pH of the Cu^{2+} /His solution to about 4, the band position of the d-d transition shifts to 15750 cm^{-1} (635 nm), a position which is about the same as for the maximum of the d-d transition of the Cu^{2+} /Gly solution in the pH range 6-10. In this system the ligands are known to be coordinating by two N_{am} and two O_c atoms in the equatorial plane and hence it is logical to assume an $\text{N}_{\text{am}}\text{O}_c\text{N}_{\text{am}}\text{O}_c$ -like coordination for Cu^{2+} /His at $\text{pH} = 4$. This conclusion is in agreement with the majority of the papers in literature.^{10, 27, 28, 32}

The ESR results support these interpretations. The copper hexa-aqua complex is dominant at $\text{pH} = 2$ (85 %) with g_0 and A_0 values that are characteristic for an oxygen coordination sphere around the copper cation. The less dominant copper complex at $\text{pH} = 2$ becomes the dominating one (75 %) at $\text{pH} = 2.9$. The g_0 and A_0 parameters of this species indicate the coordination of one nitrogen atom to the copper cation and can, therefore, be assigned to the mono-His complex (Figure 13c) or the bis-His complex as depicted in Figure 13d. In the latter complex, two His molecules are coordinating *via* the carboxyl oxygen atoms, while one of the ligands is also coordinating with the amino group. As stated before, we assume that the amino group deprotonates and subsequently coordinates to the copper

cation immediately after coordination of the carboxyl group. So, it is not very likely that the main species at pH = 2.9 is the structure of Figure 13d. Probably, it is the mono-His complex as drawn in Figure 13c. The ESR parameters of the minor species at this pH value (2.9) are characteristic for a complex in which two nitrogen atoms are coordinating to the copper cation. This species can be assigned to the bis-His complex, in which both ligands are coordinating *via* the carboxyl group and the amino group (Figure 13e). The relative amount of the two species is changing to a 50% : 50% mixture at pH = 3.4.

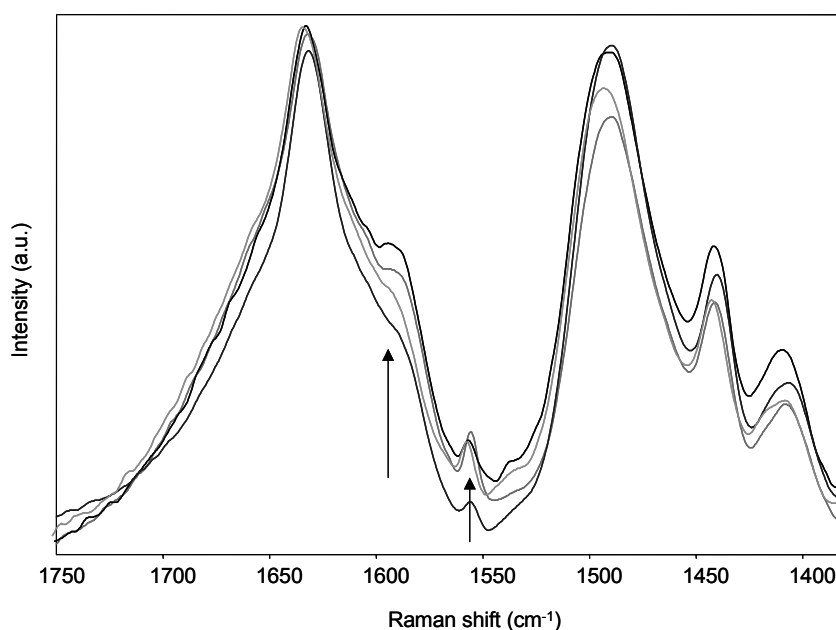


Figure 14. Raman spectra of 0.25 mM aqueous solutions of Cu²⁺/His at pH = 2.78, 2.97, 3.14 and 3.47. The arrows indicate the appearance of bands at 1588 and 1555 cm⁻¹ with increasing pH.

Further information on the coordination geometry of the different complexes at this pH can also be extracted from the Raman spectra. As can be seen in Figure 14, small but significant changes are also observed in the range 1750-1400 cm⁻¹. At pH = 2.8 two bands start to appear around 1588 cm⁻¹ and 1555 cm⁻¹. The position of the 1588 cm⁻¹ band is close to that of $\nu_{as} \text{CO}_2^-$ in the IR spectra, but it is unlikely that the band originates from the same vibration, since this type of polar mode is usually not very Raman active. Bands around 1580 cm⁻¹ also show up in the Raman spectra of free His, but at much higher pH values. These bands have been assigned to coupled imidazole C=C / C=N modes and are the result of deprotonation of the ring in accordance with the pK_a value of 6.1.⁵⁵ Apparently, analogous to

the amino group, deprotonation of the ring can only be explained as the result of coordination of (one of) the N_{im} atoms. The latter is in agreement with literature reports.^{15, 16, 32} The involvement of the imidazole ring in the coordination can also be concluded from the prominent imidazole =N-H deformation bands in the Raman spectra at 1490 and 1198 cm^{-1} , which start to reduce in intensity at about pH = 3.5 instead of around pH = 6, as for free His.

At first glance, the deprotonation of the imidazole ring and the primary amino group at a pH significantly lower than the corresponding pK_a value seems strange. Moreover, repulsive forces will hamper attraction between Cu^{2+} and the positively charged ring and the NH_3^+ group, which implies that another mechanism must be the driving force. A plausible explanation is that, after coordination to O_c , the Cu^{2+} ion has an inductive effect on the ligand that promotes deprotonation and hence coordination of the rest of the functional groups. The fact that coordination to N_{am} seems to be favored over N_{im} can be attributed to a sterically or energetically more stable geometry. It is also probable that the inductive effect *via* the imidazole ring is partly reduced by the longer distance to the carboxylate group in combination with the resonance properties of the imidazole ring system that will act as an electronic buffer. On the other hand, it is evident that coordination to N_{im} also starts at a considerably acidic pH. However, regarding the low intensity of the corresponding bands, it can be concluded that the abundance of the species in which N_{im} coordinates, is fairly low around pH = 3. The UV/Vis data, as depicted in Figures 5 and 6, are in accordance with this conclusion. The observed d-d transition bands represent the summation of all complexes that are present in the solution, but the position and the intensity determined at pH = 3 are closer to the values recorded at pH = 2 than to the data at pH = 4. This indicates that N_{im} coordination does not play a large role at pH = 3, but it also demonstrates that its relative abundance increases upon raising the pH to 4. The growing involvement of nitrogen atoms in the coordination also follows from comparison of the ESR data recorded at pH = 3.4 and pH = 4.4. A single copper complex is found to be dominating at pH = 4.4 and the corresponding ESR parameters differ from those of the complex with two His ligands at pH = 3.4. The g_0 and A_0 parameters indicate a relatively smaller number of nitrogen atoms in the coordination sphere of the copper cation at pH = 3.4 compared to the species at pH = 4.4.

4.4.3 pH range 4 - 5

On increasing the pH to 5 the maximum of the UV/Vis d-d transition band shifts to about 16200 cm⁻¹ (615 nm), a value which is similar to that of the Cu²⁺/Him complex at pH > 7, where the coordination is known to be N_{am}N_{im}N_{am}N_{im} in the equatorial plane. The observed shift for Cu²⁺/His can only be explained by an increase in the number of nitrogen atoms coordinating to the copper cation, as the ligand field splitting for nitrogen atoms is larger than the splitting for oxygen atoms.^{56, 57} The increase in the ligand field splitting cannot be caused by a decrease in the distance of the first coordination sphere around the copper cation, as the EXAFS analysis reveals that this distance remains the same in this area. For that reason it is concluded that the predominant equatorial N_{am}O_cN_{am}O_c coordination at pH = 3.5 starts to change into a N_{am}O_cN_{am}N_{im} coordination around pH = 4.5 and subsequently into an N_{am}N_{im}N_{am}N_{im} coordination at pH > 5. This is in line with most of the literature,^{27 35, 36 32, 64} but proves that the assignment of Crawford and Dalton, who stated that N_{am}O_cN_{am}O_c coordination remains the major structure up till pH = 8, is incorrect.⁴⁴ According to the UV/Vis data, N_{am}N_{im}N_{am}N_{im} coordination appears to be almost complete already at pH = 5, since the position of the band is almost identical to that of the Cu²⁺/histamine solution at pH > 6. This is in line with the ESR results, as the simulation of the ESR spectrum recorded at pH = 4.4 shows the presence of one dominating complex with g₀ and A₀ values that confirm the increasing number of coordinating nitrogen atoms in the equatorial plane.

The IR and Raman data are largely in accordance with this conclusion. Firstly, it is evident that N_{am} remains coordinated to Cu²⁺ as the IR peaks related to the NH₃⁺ group remain absent in the spectra although the pH is still far below the pK_a value of the amino group. Secondly, the Raman band at 1588 cm⁻¹ rapidly increases in intensity and at pH = 5 it becomes even stronger than the one at 1632 cm⁻¹, which clearly points to an increasing amount of coordination of (one of) the N_{im} atoms. The presence of a band at about 1588 cm⁻¹ has also been reported in Raman studies on copper (II) complexes with histidyl side chain peptides^{3, 16} and histamine.³¹ This Raman shift has been proposed to represent N^π-Cu²⁺ ligation (N^τ-protonated). Additional indications that N^π is the favored coordination site are extracted from the weak Raman band at 990 cm⁻¹ and the IR absorptions at 1272 and 1087 cm⁻¹. These bands are commonly used to distinguish the N^τ-protonated from the N^π-

protonated tautomer in the free ionic states H_2His^0 and HHis^- . In addition, the appearance and increasing intensity of a broad band at 454 cm^{-1} also indicates coordination to N_{im} . In literature this band has been assigned to a Cu-N stretching vibration in Cu^{2+} /histidyl and histamine complexes.^{3,31} Furthermore, the IR spectra reveal the appearance of a weak band at 1506 cm^{-1} around $\text{pH} = 4$. This band is absent in the spectra of free His and therefore it must originate from a Cu^{2+} /His complex. It has been proposed as a marker for coordination to N^π in the spectrum of copper(II) histamine,³¹ but the corresponding vibrational mode is not clear.

Consequently, it seems logical to conclude that the increasing coordination of N_{im} (*i.e.* N^π) will be accompanied by a proportional release of carboxylate groups from the equatorial plane to the free form. However, the vibrational frequency of the IR active $\nu_{\text{as}}\text{CO}_2^-$ decreases to 1584 cm^{-1} , while $\nu_{\text{s}}\text{CO}_2^-$ increases from 1403 to 1408 cm^{-1} . Indeed, the direction and magnitude of the shifts are similar to what we measured in the spectra of free His recorded in the same pH range, but the position of $\nu_{\text{as}}\text{CO}_2^-$ remains about 15 cm^{-1} lower, which means that a substantial amount of the carboxyl groups must remain coordinated to Cu^{2+} , either still in the equatorial plane or converted into the axial position. Therefore, we propose that the equatorial glycine-like bidentate complex $\text{Cu}^{2+}[\text{H}_2\text{His}^0(\text{O}_{\text{c}},\text{N}_{\text{am}})]_2$ (see Figure 13e) starts to convert to the tridentate complex $\text{Cu}^{2+}[\text{HHis}^-(\text{N}_{\text{am}},\text{N}_{\text{im}},\text{O}_{\text{c}})]_2$ with an equatorial histamine-like coordination for the N_{am} 's and N_{im} 's and the carboxyl O_{c} 's in the axial position (see Figure 13h). Most likely this process proceeds *via* the mixed bidentate / tridentate complex $\text{Cu}^{2+}[\text{HHis}^-(\text{N}_{\text{am}},\text{N}_{\text{im}})][\text{HHis}^-(\text{N}_{\text{am}},\text{N}_{\text{im}},\text{O}_{\text{c}})]$ as an intermediate species (see Figure 13g).

4.4.4 pH range 5 - 7

The data obtained at higher pH values confirm the previous conclusions, but also reveal that a complex with $\text{N}_{\text{im}}\text{N}_{\text{im}}\text{N}_{\text{im}}\text{N}_{\text{im}}$ coordination around $\text{pH} = 6.5$ as proposed by Basosi *et al.* is very unlikely.⁴⁰ As apparent from Figure 6, the increase of pH from 5 to 7 and basic conditions results in a shift of the maximum of the UV/Vis d-d transition band back to longer wavelength. This behavior is different from that of the Cu^{2+} /Gly and Cu^{2+} /Him solutions (Figure 6) where the band positions remain stable at respectively $\text{pH} > 6$ and $\text{pH} > 7$ after reaching the shortest wavelengths. This can be explained by assuming a process of increasing oxygen coordination in the equatorial plane at the expense of nitrogen coordination, but this is

very unlikely, as will be illustrated later by the IR and Raman data interpretation. As already mentioned before, a more plausible explanation is, that on increasing pH, two N_{am}'s and two N_{im}'s coordinate in the equatorial plane, while the O_c atoms convert from the equatorial to the axial position by substituting the axially coordinating water molecules. The net result will be a decrease of the ligand field splitting, as this parameter is also related to the distance of the d-metal orbitals to the atoms of the ligand. Such an increase in axial carboxyl coordination also explains why the intensity of the d-d transition band enhances, as this type of geometrical orientation causes a distortion of the tetragonally elongated symmetry. The effect is that the transition probability becomes larger than for a complex structure without distortion and hence the intensity increases. The observed shift of the band maximum to lower energy confirms the distortion of the symmetry, as the coordination of a carboxyl group at an axial position initiates an increase in the distance between the central copper ion and the chelating atoms in the equatorial plane. This is confirmed by the EXAFS analysis, in which an increase in the distance of the copper cation to the first coordination sphere is observed upon increasing the pH from 4.4 to 7.3. The average distance increases significantly from 1.96 at pH = 4.4 to 1.99 at pH = 6.0. In the Cu²⁺/Him solution this distorting axial coordination cannot occur, so both the position and the intensity of the d-d transition will not change on increasing the pH. Although this phenomenon is often overlooked in literature, it illustrates that the position of the d-d transition band in the UV/Vis spectra is not only a function of the nature and the amount of the coordinating atoms, but also depends on the distance between the central ion and the coordinating groups.

These conclusions confirm the conversion from the bidentate ligand complex Cu²⁺[H₂His⁰(O_c,N_{am})]₂ to the tridentate ligand form Cu²⁺[HHis⁻(O_c,N_{am},N^π)]₂, most likely *via* the mixed bidentate / tridentate complex Cu²⁺[HHis⁻(N_{am},N^π)] [HHis⁻(O_c,N_{am},N^π)] as an intermediate form. In contrast, the co-existence of the mono-ligand tridentate form Cu²⁺[HHis⁻(O_c,N_{am},N^π)] is unlikely, since this would mean the presence of free His in the solution. However, bands that can be assigned to free His have not been observed in this pH range, neither in the IR nor in the Raman spectra.

As already pointed out, coordination of both N_{am} and N_{im} also follows from the vibrational spectra. At pH = 6 a shoulder around 1578 cm⁻¹ appears on the Raman band at 1590 cm⁻¹ and the intense peak at 1492 cm⁻¹ drops in intensity. Furthermore, new bands

appear at 1325, 1310, 1226, 1022, 826 and 456 cm^{-1} . Similar to free His, the decrease in intensity of the 1492 cm^{-1} band can be attributed to the decrease in symmetry of the imidazole ring as result of deprotonation of one of the N_{im} atoms. It also seems obvious to assign the shoulder around 1578 cm^{-1} as well as the other new bands to the formation of a complex with N^{τ} coordination, since the presence of two bands around 1580 cm^{-1} is also observed in free His above $\text{pH} = 6$, in accordance with the pK_{a} value of the ring. However, according to literature,^{3, 15, 16, 31} the vibration that is correlated to N^{τ} -ligation (N^{π} -protonated) should be found at the high instead of the low frequency side of the 1588 cm^{-1} band, *i.e.* around 1603 cm^{-1} . Besides, model calculations revealed that coordination to N^{τ} is not attractive for sterical reasons. This implies that the co-existence of complexes with coordination to both N^{τ} and N^{π} or a complex with both tautomeric forms coordinated to the same copper ion, as suggested by Torregiani *et al.*,³¹ is unlikely. Another argument to reject two types of coordination of the N_{im} atoms is the lack of doublets around 1100 cm^{-1} in IR and around 1275 and 1000 cm^{-1} in Raman. According to literature, such double bands should have been present as additional, commonly accepted tautomer markers,^{9, 29, 30, 33, 65-67} but only one band is observed in these regions. The presence of one tautomeric form is further evidenced by the small bandwidth of the Raman active ring breathing vibration at 1273 cm^{-1} . This peak is considerably sharper than the corresponding one in the Raman spectra of free His, which indicates a single, rigid structure of the ring, *i.e.* only one type of N_{im} coordination. In order to explain the presence of the band around 1578 cm^{-1} we propose two possibilities: (1) the metal coordination of the ring results in decoupling of the combined C=C / C=N vibration, which gives rise to separate C=C and C=N stretching modes, or (2) two N^{π} -ligated complexes are present that only differ in the symmetrical orientation towards the copper ion. The origin of the weak Raman band that comes up at 1555 cm^{-1} is not clear, but its appearance matches the explanation of decoupling, as in this region only C=C and/or C=N stretching modes are present. Finally, the fact that only one Raman band arises at 1228 cm^{-1} can also be attributed to deprotonation of only one of the N_{im} atoms, similar to free His.⁵⁵

4.4.5 pH range 7 - 10

The spectral changes in IR, Raman, UV/Vis and EXAFS in the pH range 7-10 are

relatively small compared to the data collected at pH = 6. The EXAFS results show a negligible increase of the average first shell inter-atomic distance between the copper ion and the chelating N-atoms, which implies that the distortion of the octahedral symmetry is maintained, obviously as a result of the axial coordination of the carboxyl groups. These results confirm that Cu²⁺[HHis⁻(O_c,N_{am},N^π)]₂ (species **h**) has become the predominant complex at neutral and basic conditions. In accordance, simulation calculations on the ESR spectrum at pH = 7.3 clearly point to the dominating presence of a single copper complex. Moreover, the high A₀ and low g₀ value are fully in line with the Cu²⁺[HHis⁻(O_c,N_{am},N^π)]₂ complex (species **h** in Table 1). As can be seen from Figure 5, the UV/Vis absorption band recorded at pH = 7 shows a minor red shift compared to the spectrum taken at pH = 6, but at higher pH the position of the band stabilizes at 16000 cm⁻¹ (625 nm). The former trend illustrates the increasing distortion of the octahedral symmetry as a result of conversion to Cu²⁺[HHis(O_c,N_{am},N^π)]₂, whereas the latter phenomenon indicates that this process is virtually completed at pH > 7. The same can be concluded from the increase in absorption intensity in the UV/Vis on raising the pH from 5 to 7, which is consistent with the results from EXAFS and ESR. The on-going intensity increase in UV/Vis at pH > 7 seems to contradict this, but, most likely, this is due to the formation of precipitating copper hydroxide/oxide species, as pointed out in the experimental section. It also explains why Perrin and Sharma⁴⁷ and Sigel *et al.*³⁶ erroneously assumed the presence of Cu²⁺(OH)/His-type of complexes at pH > 7.

As already indicated, the changes in the vibrational spectra are small, but important information on the coordination of the CO₂⁻ group can be extracted from the position of the anti-symmetric stretching band (ν_{as} CO₂⁻) around 1584 cm⁻¹ in IR. In contrast to free His, where we observed a continuous red shift on increasing the pH, the band remains fixed at 1584 cm⁻¹ for Cu²⁺/His at pH > 5. This finding confirms the conclusion drawn from UV/Vis that the carboxyl group is coordinated to Cu²⁺, but the fact that the band does not shift, like in free His, also indicates a change in the coordination position from the equatorial to the axial position. Closer examination of the 1584 cm⁻¹ band reveals that it is much broader around pH = 4, which points to differently coordinated CO₂⁻ groups and hence to the co-existence of two different complexes. A plausible explanation is to assume a mixture of complexes at this pH with the oxygen(s) in the equatorial plane, in the axial position or both. As already explained,

the equatorial position is supposed to be preferred at low pH and so the complexes at higher pH must be the ones with the O_c coordinated in the axial position. The fixed band position and band width in the pH range 7-10 can be considered as a prove that reorientation into the axial position is completed. The simultaneous disappearance of the Raman band at 560 cm^{-1} , which has been assigned to a Cu-O vibration in the equatorial plane, can be seen as additional evidence for the correctness of this assignment. Further changes in the Raman spectra in Figure 5 are small, although the intensity of the combined C=C / C=N band at 1580 cm^{-1} increases at the expense of the one at 1632 cm^{-1} . This indicates that all His has become coordinated to Cu^{2+} via N^π , which is confirmed by the enhanced intensity of the Cu-N stretching band at 454 cm^{-1} . It follows that the bi-ligand tridentate complex $\text{Cu}^{2+}[\text{HHis}^-(O_c, N_{am}, N_{im})]_2$ (species **h**) is indeed the major species prevailing at high pH, while bidentate geometries are probably no longer present.

4.5 Conclusions

The combined application of IR, Raman, UV/Vis, ESR and EXAFS spectroscopy appears to be a very successful approach to obtain a variety of complementary information on the geometrical structures and relative abundances of the complexes that are formed in the aqueous $\text{Cu}^{2+}/\text{His}$ (1:2) system at various pHs. The results from UV/Vis and ESR analyses are fully consistent with the nature of the atoms in the first coordination shell of the Cu^{2+} ion, while EXAFS yields information on the average distance between the coordinating atoms and the central Cu^{2+} ion. Finally, IR and Raman spectroscopic monitoring during titration experiments produces detailed complementary information on the state of protonation of the His ligands and hence on the sites involved in the coordination to Cu^{2+} . The multi-technique approach of measuring samples under more or less identical conditions over a wide range of pH values proves to be extremely valuable for obtaining accurate and reliable information on the coordination chemistry of $\text{Cu}^{2+}/\text{His}$ complexes. As a result, structural proposals from literature have been unambiguously confirmed, clarified or corrected.

The results of the integrated interpretation of the spectroscopic data have been summarized in Figure 15. In addition, equilibrium constants have been calculated, which are presented in Table 3. The process of complex formation turns out to be reversible as long as

the pH does not exceed a value of 10. At a higher pH decomposition and precipitation occurs.

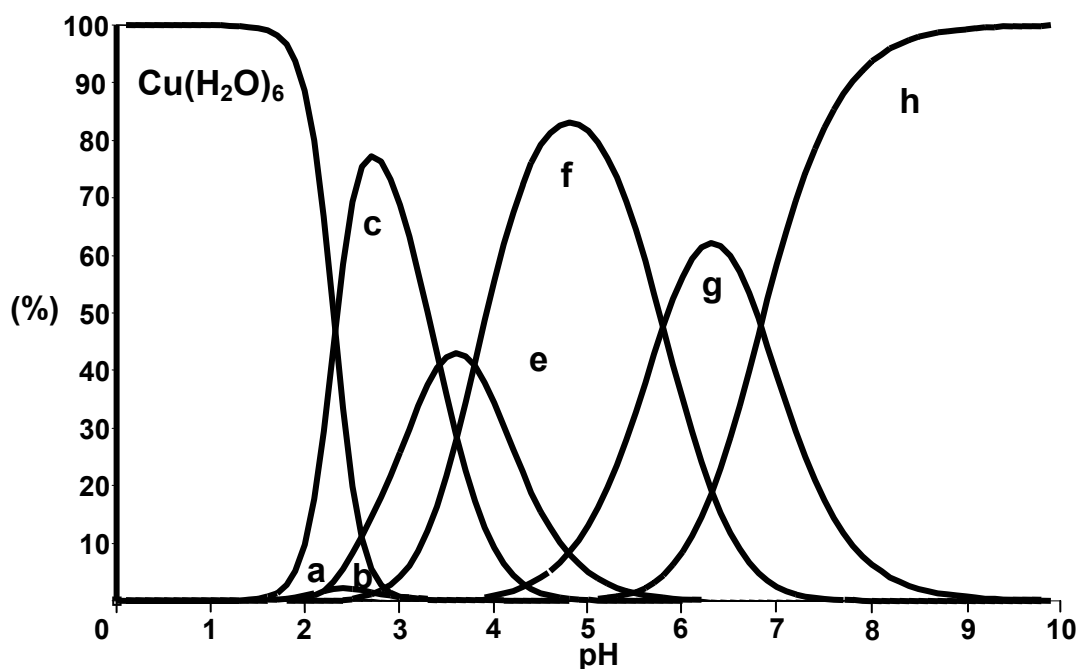


Figure 15. Proposed distribution of Cu²⁺/His complexes as a function of the solution pH. Indications **a**, **b**, **c**, **e**, **f**, **g** and **h** correspond to the structures depicted in Figure 13. Note that complex **d** is supposed to be absent.

Table 3. Equilibrium constants K_{eq} of the Cu²⁺/His complexes in aqueous solution in the pH range 0-10. The complexes **a**, **b**, **c**, **e**, **f**, **g** and **h** correspond to the structures depicted in Figure 13.

Conversion	K_{eq}
Cu ²⁺ ↔ a	3.5×10^{-5}
a ↔ b	3.0×10^{-2}
b ↔ c	1.0×10^{-1}
c ↔ e	3.7×10^{-4}
e ↔ f	1.6×10^{-4}
f ↔ g	1.6×10^{-6}
g ↔ h	1.5×10^{-7}

Under highly acidic conditions both Cu²⁺ and His are present as free ions. The formation of complexes starts around the pK_a value of the carboxyl group, *i.e.* at pH = 1.8, by the coordination of a carboxyl oxygen atom in the equatorial plane (species **a** and **b**). Almost concomitantly coordination *via* the amino group begins, which results in a bidentate glycine-

like chelation with mainly one ligand (species **c**). At pH = 3 this complex is the major constituent. However, coordination of a second His molecule rapidly follows and at pH = 3.5 the bi-ligand complex is the dominant species (**e**). Raman data show that coordination to the N^π atom of the imidazole ring starts around pH = 2.8 and around pH = 5 complexes with coordination *via* both N_{am} and N^π become the main components (species **f** and **g**). The coordination of the nitrogen atoms is histamine-like in the equatorial plane. Most likely, this reorientation of the His ligands is accompanied by a partial release of the carboxyl groups to the non-bonded state. According to the IR spectra, the coordination of the oxygen atoms changes from the equatorial to the axial position. At pH > 7 the bi-ligand tridentate complex with four N atoms in the equatorial plane and two carboxyl O atoms in the axial position is the dominant geometrical structure (species **h**). This complex remains stable up till pH=10, but decomposes at a higher pH.

Finally, it is concluded that the pK_a values are not the primary driving force in the coordination process. After deprotonation and anchoring to the carboxyl group, in accordance with the first His pK_a value (1.8), coordination of N_{am} and N_{im} to Cu^{2+} occurs around pH = 3 and 5, respectively, which is in a different order and at significantly lower pH levels than could be expected on the basis of the pK_a values of these nitrogen groups (9.1 and 6.0, respectively). This might be the result of an inductive effect of Cu^{2+} , but the precise origin of the phenomenon is not yet clear.

Acknowledgements

Financial support from NWO/CW - Van der Leeuw, NRSC-C and NWO/CW-VICI is gratefully acknowledged. Mettler Toledo (Autochem) is kindly thanked for the use of the React-IR 4000 system. Fouad Soulimani is thanked for collecting the IR, Raman and UV-Vis data. Andy Beale is acknowledged for his contribution to the EXAFS analyses. Ernst van Faassen (UU) is thanked for writing the ESR simulation program, for his help with the ESR measurements, for the use of the ESR spectrometer (ESP300) and for discussion on the content of this chapter. Robert Schoonheydt (KU Leuven) is thanked for use of the ESR spectrometer (ESP300E).

References

- [1] R. J. Sundberg and R. B. Martin, *Chem. Rev.* **74** (1974) 471.
- [2] A. Abbaspour and M. A. Kamyabi, *Anal. Chim. Acta* **512** (2004) 257.
- [3] A. Torreggiani, M. Tamba and G. Fini, *Biopolym.* **57** (2000) 149.
- [4] D. Wang, X. Zhao, M. Varghek and T. G. Spiro, *J. Am. Chem. Soc.* **122** (2000) 2193.
- [5] D. S. Caswell and T. G. Spiro, *J. Am. Chem. Soc.* **108** (1986) 6470.
- [6] F. Carrera, E. Sanchez-Marcos, P. J. Merklung, J. Chaboy and A. Muñoz-Páez, *Inorg. Chem.* **43** (2004) 6674.
- [7] G. R. Arena, R. Cali, V. Cucinotta, S. Musumeci, E. Rizzarelli and S. Sammartano, *J. Chem. Soc. Dalton Trans.* (1984) 1651.
- [8] P. J. Glusker, *Adv. Protein Chem.* (1991) 1.
- [9] K. Hasegawa, T. Ono and T. Noguchi, *J. Phys. Chem. A* **106** (2002) 3377.
- [10] M. Casolaro, M. Chelli, M. Ginanneschi, F. Laschi, M. Muniz-Miranda, A. M. Papini and G. Sbrana, *Spectrochim. Acta A* **55** (1999) 1675.
- [11] M. A. Doran, S. Chabarek and A. E. Martell, *J. Am. Chem. Soc.* **86** (1964) 2129.
- [12] R. W. Larsen, D. J. Nunez, W. T. Morgan, B. B. Muhoberac and M. R. Ondrias, *Biophys. J.* (1992) 1007.
- [13] S. Hashimoto and H. Takeuchi, *J. Am. Chem. Soc.* **120** (1998) 11012.
- [14] S. L. Gao, S. Chen, H. Liu, R. Hou and Q. Ji, *Russ. J. Gen. Chem.* **74** (2004) 371.
- [15] T. Miura, A. Hori-i, H. Mototani and H. Takeuchi, *Biochem.* **38** (1999) 11560.
- [16] T. Miura, T. Satoh, A. Hori-i and H. Takeuchi, *J. Raman Spectrosc.* **29** (1998) 41.
- [17] X. Zhao, D. Wang and T. G. Spiro, *Inorg. Chem.* **37** (1998) 5414.
- [18] R. Grommen, P. Manikandan, Y. Gao, T. Shane, J. J. Shane, R. A. Schoonheydt, B. M. Weckhuysen and D. Goldfarb, *J. Am. Chem. Soc.* **122** (2000) 11488.
- [19] L. Fu, B. M. Weckhuysen, A. A. Verberckmoes and R. A. Schoonheydt, *Clay Minerals* **31** (1996) 491.
- [20] J. G. Mesu, D. Baute, H. J. Tromp, E. E. van Faassen and B. M. Weckhuysen, *Stud. Surf. Sci Catal.* **143** (2002) 287.
- [21] B. M. Weckhuysen, A. A. Verberckmoes, L. Fu and R. A. Schoonheydt, *J. Phys. Chem.* **100** (1996) 9456.
- [22] B. M. Weckhuysen, A. A. Verberckmoes, I. P. Vannijvel, J. A. Pelgrims, P. L. Buskens, P. A. Jacobs and R. A. Schoonheydt, *Angew. Chem. Int. Ed. Engl.* **34** (1995) 2652.

- [23] K. M. Wellman and B.-K. Wong, *Proc. N.A.S.* **64** (1969) 824.
- [24] L. Casella and M. Gulotti, *J. Inorg. Biochem.* **18** (1983) 19.
- [25] B. A. Goodman, D. B. McPhail and H. K. J. Powell, *J. Chem. Soc. Dalton Trans.* (1980) 82.
- [26] E. Prenesti and S. Berto, *J. Inorg. Biochem.* **88** (2002) 37.
- [27] T. P. A. Kruck and B. Sarkar, *Can. J. Chem.* **51** (1973) 3549.
- [28] Y. W. B. Sarkar, *J. Biol. Chem.* **242** (1967) 5572.
- [29] E. M. Marti, C. Methivier, P. Dubot and C. M. Pradier, *J. Phys. Chem. B* **107** (2003) 10785.
- [30] R. H. Carlson and T. L. Brown, *Inorg. Chem.* **5** (1966) 5.
- [31] A. Torreggiani, M. Tamba, S. Bonora and G. Fini, *Biopolym.* **72** (2003) 290.
- [32] M. Itabashi and K. Itoh, *Bull. Chem. Soc. Jpn.* **53** (1980) 3131.
- [33] S. Martusevičius, G. Niaura, Z. Talaikyte and V. Razumas, *Vibr. Spectrosc.* **10** (1996) 271.
- [34] G. Valensin and R. Basosi, *J. Inorg. Biochem.* **23** (1985) 125.
- [35] H. Sigel and D. B. McCormick, *J. Am. Chem. Soc.* **93** (1971) 2041.
- [36] H. Sigel, R. E. MacKenzie and D. B. McCormick, *Biochim. Biophys. Acta* **200** (1970) 411.
- [37] P. A. Tishmack and D. Bashford, *Biochem.* **36** (1997) 11984.
- [38] B. Epel, P. Manikandan, P. M. H. Kroneck and D. Goldfarb, *Appl. Magn. Res.* **21** (2001) 287.
- [39] P. Manikandan, B. Epel and D. Goldfarb, *Inorg. Chem.* **40** (2001) 781.
- [40] R. Basosi, G. Valensin, E. Gaggelli, W. Froncisz, M. Pasenkiewicz-Gierula, W. E. Antholine and J. S. Hyde, *Inorg. Chem.* **25** (1986) 3006.
- [41] D. Baute, D. Arieli, F. Neese, H. Zimmerman, B. M. Weckhuysen and D. Goldfarb, *J. Am. Chem. Soc.* **126** (2004) 11733.
- [42] G. Rotilio and L. Calabrese, *Arch. Biochem. Biophys.* **143** (1971) 218.
- [43] M. J. Colaneri and J. Peisach, *J. Am. Chem. Soc.* **114** (1992) 5335.
- [44] T. H. Crawford and J. O. Dalton, *Arch. Biochem. Biophys.* **131** (1969) 123.
- [45] V. A. Abramenko, S. N. Bolotin and I. A. Nikolaienko, *J. Mol. Liq.* **91** (2001) 219.
- [46] R. W. Strange and N. J. B. e. al, *J. Am. Chem. Soc.* **109** (1987) 7157.
- [47] D. D. Perrin and V. S. Sharma, *J. Chem. Soc. A* (1967) 724.
- [48] D. R. Williams, *J. Chem Soc. Dalton* (1972) 790.
- [49] H. C. Freeman and R. P. Martin, *J. Biol. Chem.* **224** (1969) 4823.
- [50] J. L. Meyer and J. E. Bauman, *J. Am. Chem. Soc.* **92** (1970) 4210.
- [51] R. Leberman and B. R. Rabin, *Trans. Farad. Soc.* **55** (1959) 1660.
- [52] Y. Zhang and S. Akilesh, *Inorg. Chem.* **39** (2000) 3057.
- [53] J. G. Mesu, A. M. J. van der Eerden, F. M. F. de Groot and B. M. Weckhuysen, *J. Phys. Chem. B* **109** (2005) 4042.

- [54] N. Binsted, J. W. Campbell, S. J. Gurman and P. C. Stephenson, *EXAFS Analysis Programs*, Daresbury Laboratory, Warrington, 1991.
- [55] J. G. Mesu, T. Visser, F. Soulimani and B. M. Weckhuysen, *Vibr. Spectrosc. in press*.
- [56] M. Gerloch and E. C. Constable, *Transition Metal Chemistry*, VCH, Weinheim, 1994.
- [57] A. B. P. Lever, *Inorganic Electronic Spectroscopy*, Elsevier Science B.V., Amsterdam, 1987.
- [58] B. K. Teo, *EXAFS: Basic Principles and Data Analysis*, Springer-Verlag, New York, 1986.
- [59] D. C. Koningsberger, B. L. Mojet, G. E. van Dorssen and D. E. Ramaker, *Top. Catal.* **10** (2000) 143.
- [60] T. Szabo-Planka, A. Rockenbauer, M. Gyor and F. Gaizer, *J. Coord. Chem.* **17** (1988) 69.
- [61] P. S. Salmon, G. W. Neilson and J. E. Enderby, *J. Phys. C* **21** (1988) 1335.
- [62] O. Siiman, N. M. Young and P. R. Carey, *J. Am. Chem. Soc.* **96** (1974) 5583.
- [63] K. Nakamoto, Y. Morimoto and A. E. Martell, *J. Am. Chem. Soc.* **83** (1961) 4528.
- [64] D. R. Williams, *J. Chem. Soc. Dalton Trans.* (1972) 790.
- [65] A. Toyoma, K. Ono, S. Hashimoto and H. Takeuchi, *J. Chem. Phys. A* **106** (2002) 3403.
- [66] I. Ashikawa and K. Itoh, *Biopolym.* **18** (1979) 1859.
- [67] T. Noguchi, Y. Inoue and X. S. Tang, *Biochem.* **38** (1999) 10187.

Chapter 5

On the Molecular Structure of Aqueous Cu^{2+} /Histidine Complexes as Studied with XANES Spectroscopy

Abstract

X-ray absorption spectroscopy has been used to study the molecular structures of Cu^{2+} /His complexes in aqueous solution at different pH values. Information on the coordination geometry and local environment of copper was obtained by following the changes in the features present in the X-ray absorption near edge structure (XANES) as a function of the solution pH. For the Cu^{2+} /His solutions measured at high photon flux beamlines a reducing influence of the X-ray beam on the sample was found. The extent of reduction was found to be independent of time, but dependent on the solution pH. A similar trend was found for the development of the maximum of the d-d transition as a function of solution pH, as measured with UV/Vis spectroscopy. These findings provide evidence that (1) Cu^{2+} reduction is facilitated when the imidazole rings are in equatorial coordination and (2) XANES can be used to monitor the molecular structure of Cu^{2+} /His complexes in aqueous solution.

5.1 Introduction

X-ray absorption spectroscopy (XAS) is a direct method to probe the electronic and structural nature of transition metal ion complexes. In contrast to X-ray diffraction, XAS is not dependent on long-range ordering of these complexes. The technique can be used to probe the local structure around the transition metal ion by analyzing the extended X-ray absorption fine structure (EXAFS) of the X-ray absorption spectrum. From this analysis information can be obtained on which neighboring atoms are present, as well the distances of these neighboring atoms, even though it is very difficult to discriminate between neighboring atoms in the periodic table. The technique can also be used to determine the oxidation state of the transition metal ion by studying the X-ray absorption near edge structure (XANES) region of the X-ray absorption spectrum. XANES also contains information on the molecular structure of the transition metal ion complex.

In this study XAS was used to study copper histidine ($\text{Cu}^{2+}/\text{His}$) complexes in aqueous solutions as a function of the solution pH. There are only a few X-ray absorption studies on $\text{Cu}^{2+}/\text{His}$ complexes available in literature.^{1, 2} In these studies the focus is on the EXAFS part of the X-ray absorption spectrum. To our best knowledge the first X-ray absorption study on the copper histidine complex in aqueous solution was by Ozutsumi *et al.* They studied the properties of a number of mono- and bis(aminocarboxylato)copper(II) complexes in aqueous solution by EXAFS and spectrophotometry.¹ They assumed a glycine-glycine coordination mode for histidine in the copper histidine complex. Recently, Carrera *et al.* studied the EXAFS of 10 mM and 50 mM aqueous solutions of copper histidine at physiological pH = 7.3.² They propose a dominating histamine-histamine-like coordination mode for histidine in the equatorial plane at this pH value. The key to discriminate between the different proposed coordination modes of histidine in the complex is the determination of the number of imidazole rings within the equatorial plane of the complex. These imidazole rings give rise to an enhanced multiple scattering contribution, thus allowing the analysis of higher shells. These results confirm earlier results of Strange *et al.*, who simulated the EXAFS of a number of imidazole-containing copper complexes with a multiple scattering treatment in orders to study the metal-histidine coordination in metalloproteins.³

In this work the abundant information available in literature on the XANES of copper complexes will be used to obtain information on the molecular structure of $\text{Cu}^{2+}/\text{His}$

complexes in aqueous solutions as a function of the pH. This will be done by carefully fingerprinting the developments in the different features that are present in the XANES regions of the X-ray absorption spectra. The results will be compared with results obtained from IR, Raman, UV/Vis, EXAFS and ESR studies described in the previous chapter. It will be demonstrated that additional information on the molecular structure of the Cu²⁺/His complexes can be extracted from the XANES region.

5.2 Experimental

5.2.1 Chemicals and solutions

All chemicals were obtained from Acros Organics (Geel, Belgium). For each experiment aqueous solutions of Cu(NO₃)₂·3H₂O and L-histidine (His), histamine (Him) or glycine (Gly) (all *p.a.* grade), were freshly made. The copper nitrate precursor salt was used, combined with HNO₃ and NaOH to adjust the solution pH (instead of CuCl₂ and HCl, respectively), to minimize the reducing effect of the X-ray beam on the sample.⁴

Table 1. Overview of the X-ray absorption experiments performed with aqueous Cu²⁺ complex solutions at different pH levels. The ligands (L) present in the Cu²⁺ complex are indicated in the fourth column.

Photon Flux	Beamlines	[Cu] (M)	L	Cu : L	pH
LOW	Hasylab X1	0.33	His	1:5	2.9, 4.4, 7.3
	BM29	0.25	His	1:5	2.0, 3.4, 6.0, 8.0
	DUBBLE	0.01	His	1:3	3.8, 7.3
	DUBBLE	0.01	Him	1:3	3.8, 7.3
	DUBBLE	0.01	Gly	1:3	3.8, 7.3
	DUBBLE	0.01	-	1:3	3.8, 7.3
HIGH	ID24	0.02	His	1:3	1,2,3,4,5,6,7,8,9,10,11 and 12
	ID26	0.01	His	1:5	0, 2, 4, 6, 8, 10 and 12

All the samples were measured at room temperature, using a stainless steel sample cell (diameter of 2.5 mm) with kapton windows. The X-ray absorption spectra of aqueous Cu²⁺/His solutions at different pH levels were measured at different beamlines and at different

synchrotrons. For comparison X-ray absorption spectra of 0.01 M aqueous solutions of $\text{Cu}^{2+}/\text{His}$, $\text{Cu}^{2+}/\text{Gly}$ and $\text{Cu}(\text{NO}_3)_2 \cdot 3\text{H}_2\text{O}$ without ligand were collected at pH 3.8 and 7.3 at the DUBBLE beamline. An overview of all the experiments is presented in Table 1. Important to note is that the aqueous $\text{Cu}^{2+}/\text{His}$ solutions have been measured both at beamlines with a relative low photon flux ($10^{10} - 10^{11}$ photons $\text{s}^{-1} \text{mm}^{-2}$) and at beamlines with a relative high photon flux ($>10^{13}$ photons $\text{s}^{-1} \text{mm}^{-2}$).

5.2.2 X-ray absorption spectroscopy

The copper K-edge absorption spectra of 0.33 M aqueous $\text{Cu}^{2+}/\text{His}$ solutions were collected at Hasylab (Hamburg, Germany), Wiggler Station X1.1, using an Si(111) double crystal monochromator. The monochromator was detuned to 50% of the maximum intensity to avoid higher harmonics in the X-ray beam. The photon flux on the sample was 10^{10} photons $\text{s}^{-1} \text{mm}^{-2}$. At BM29 (ESRF, Grenoble, France) the X-ray absorption spectra were collected with 0.25 M copper histidine solutions, using a double crystal Si(311) monochromator. Higher harmonics rejection was carried out by detuning both crystals by 50%. The sample spectra were recorded in transmission mode. Several scans were averaged to improve the signal to noise ratio. The flux at the sample was 10^{10} photons $\text{s}^{-1} \text{mm}^{-2}$. At ID26 (ESRF, Grenoble, France) 0.01 M $\text{Cu}^{2+}/\text{His}$ solutions were studied, using a Si(220) double crystal monochromator. The samples were measured using both a multi-element germanium detector and a photo-diode detector. The spot size on the sample was $1.0 \times 0.5 \text{mm}^2$, with a photon flux of $>10^{13}$ photons $\text{s}^{-1} \text{mm}^{-2}$. The copper K-edge XAFS spectra on 0.01 M aqueous $\text{Cu}^{2+}/\text{His}$, His and Gly solutions at pH 3.8 and 7.3 were collected at the DUBBLE beamline (BM26A) of the ESRF. The measurements were performed using a Si(111) double crystal monochromator. The spot size on the sample was $0.5 \times 0.5 \text{mm}^2$ (H x V, FWHM), with a photon flux of 10^{11} photons s^{-1} . XAFS spectra were collected in the fluorescence mode, in a 90-degree orientation to the incident X-ray beam, using a nine-channel monolithic germanium detector. One X-ray absorption spectrum was collected in 45 min. and per sample three spectra were collected and averaged, in order to improve the signal to noise ratio. At the energy-dispersive beamline ID24 at the ESRF the X-ray absorption spectra of 0.02 M aqueous $\text{Cu}^{2+}/\text{His}$ solutions were studied. The set-up used for data

collection has been described in detail in chapter 2. The Cu²⁺/His solutions were measured in a cuvette with a path length of 5 mm and a total sample volume of 80 μ l. The transparent quartz windows in the X-ray direction have a thickness of 100 μ m to minimize X-ray absorption by the windows at the energy of the copper edge. The spot size of the X-ray beam in the focal spot in the sample is 0.03 x 0.2 mm² (H x V, FWHM). The XAFS data were collected in the transmission mode using a phosphorous masked Peltier cooled Princeton CCD camera. The X-rays (with a photon flux of 10¹² photons s⁻¹) were focused on the sample using a curved Si(111) Bragg polychromator crystal. One complete X-ray absorption spectrum was collected in 12 s. During all experiments a copper foil was measured for determining the edge position of copper (first maximum in the first derivative of the absorption spectrum) in order to calibrate the energy of the monochromator.

5.2.3 UV/Vis spectroscopy

UV/Vis spectra of the aqueous solutions were measured from 50000 cm⁻¹ to 10000 cm⁻¹ (200 to 1000 nm) at a spectral resolution of 0.15 nm with a Cary 50 spectrometer (Varian) equipped with a probe (Hellma) that was connected to the spectrometer *via* optical fibers. The effective optical path length in the probe head was 2 mm for the samples with a high concentration, whereas the path length was 10 mm for the more diluted samples.

5.3 Results

A lot of information can be obtained from the XANES of the X-ray absorption spectra of transition metal ion complexes. This is also the case for Cu²⁺ complexes. The X-ray absorption spectra of the aqueous Cu²⁺/His solutions as a function of the solution pH (collected at ID26) are presented in Figure 1. Different features are present in the XANES of the solutions and trends in the development of these features can be observed. These features are indicated in Figure 1 by the letters A through E. The physical background of the features will be discussed, although the main focus will be on the development of the features A and B as a function of the solution pH.

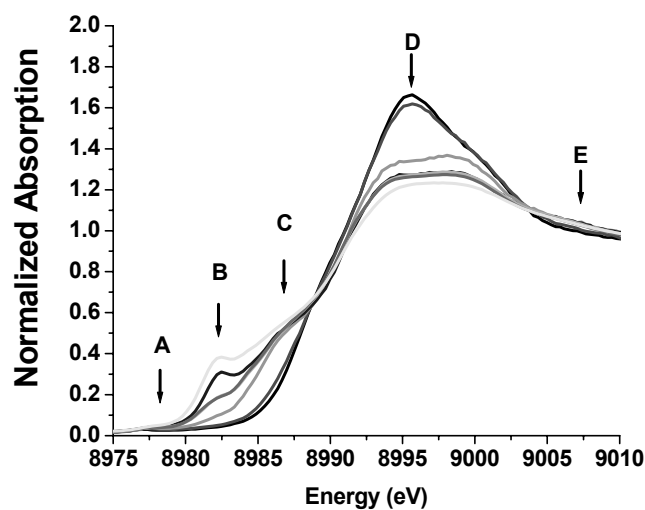


Figure 1: XANES of the Cu^{2+} /His solutions as a function of the solution pH, collected at ID26. The features that are present in the XANES are indicated by the letters A through E. The trends as a function of pH will be discussed further on.

In the XANES of the X-ray absorption spectra of Cu^{2+} complexes a very weak feature is present at 8978 eV (at position A in Figure 1). This feature can be assigned to a dipole forbidden, but quadrupole-allowed $1s \rightarrow 3d$ transition.⁵⁻⁷ Only Cu^{2+} complexes can give rise to this transition, as the 3d orbitals in Cu^+ complexes are completely filled. The energy position of this pre-edge feature is influenced by the properties of the ligands coordinating to copper and it is reported to shift to higher energies in the order of the spectrochemical series.⁸ This trend is also observed for the different Cu^{2+} complexes that were measured at DUBBLE. In the XANES the position of the maximum of the feature is shifting to higher energy by about 0.7 eV upon increasing the pH from 3.8 to 7.3 (see Figure 2). The shift is largest for the Cu^{2+} /His solution at pH 7.3. There is a linear relationship between this position shift and the shift in the position of the maximum of the d-d transition in the UV/Vis absorption spectrum of the same solution. This relationship is shown in figure 3. It indicates that the position of the maximum of the $1s \rightarrow 3d$ transition is shifting to higher energy when the ligand field of the complex is shifting to higher energy. This is as expected since the empty d-orbital to which the transition occurs, is shifted to a higher energy in the complex with the larger ligand field splitting. However, the shift (in eV) of the maximum of the $1s \rightarrow 3d$ transition is larger than the shift (also in eV) of the maximum of the d-d transition. An opposite trend is expected, as

an increase in ligand field strength increases the energy of the highest unoccupied d-orbital, but at the same time decreases the energy of the occupied d-orbitals, from which the d-d transition occurs.

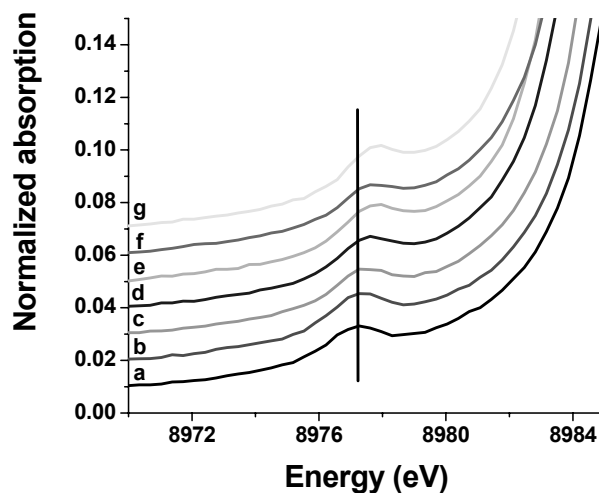


Figure 2: The $1s \rightarrow 3d$ transition in the XANES of the spectra of the Cu^{2+} complexes collected at the DUBBLE beamline: (a) Cu^{2+} nitrate, (b) Cu^{2+} /Him 3.8, (c) Cu^{2+} /Gly 3.8, (d) Cu^{2+} /His 3.8, (e) Cu^{2+} /Gly 7.3, (f) Cu^{2+} /His 7.3 and (g) Cu^{2+} /Him 7.3. The numbers (3.8 and 7.3) indicate the pH of the solution. The line is added to illustrate the shift to higher energy.

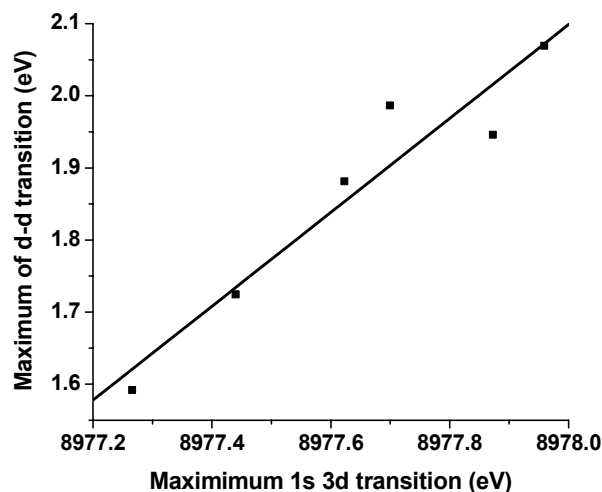


Figure 3: The linear relationship between the position of the maximum of the $1s \rightarrow 3d$ transition in the X-ray absorption spectra and the position of the maximum of the d-d transition (in eV) in the corresponding UV-Vis absorption spectra.

From the XANES also the oxidation state of copper can be determined.⁹ It has long been recognized that a pre-edge feature around 8982.5 eV (at position B in figure 1) is present in the absorption edge spectra of Cu(I) complexes, but not in those of Cu(II) complexes.⁹ This 8982.5 eV pre-edge feature in Cu(I) complexes has been assigned to a Cu 1s → 4s transition.¹⁰ The intensity of this feature is much higher for Cu(I) complexes than it is for Cu(II) complexes, as Cu(I) complexes have the tendency to form trigonal or distorted tetrahedral complexes, which allow s-p orbital mixing.

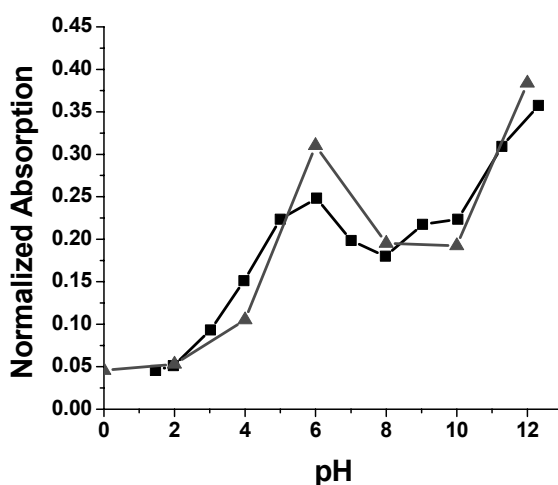


Figure 4: The development of the normalized intensity of the 8982.5 eV feature (feature B in Figure 1) as a function of the solution pH, measured at both ID24 (-■-) and ID26 (-▲-). These are the undulator beamlines with a high photon flux.

For the aqueous Cu²⁺/His complexes measured at the low intensity beamlines no absorption band is observed at 8982.5 eV. This is contrary the solutions that were studied at the beamlines with a high photon flux. The spectra of the aqueous Cu²⁺/His solutions measured at the high-flux beamline ID26 are presented in Figure 1. In these spectra a feature develops at 8982.5 eV, indicating the reduction of copper from Cu²⁺ to Cu⁺. The intensity of the peak is a function of the solution pH. The feature is not present at low pH, but its intensity increases up to a solution pH of 6, after which it is lower again at pH = 8 and 10, after which it increases again for a solution with pH = 12 (see figure 4). A similar trend in the development of the feature at 8982.5 eV is observed for the Cu²⁺/His solutions that were studied at the other beamline with a high photon flux, *viz.* the ED-XAFS undulator beamline ID24 (see figure 4).

The occurrence of reduction is confirmed by the development in the $1s \rightarrow 3d$ transition for a number of Cu^{2+} /His solutions with different pH. The development of this feature is presented in Figure 5. The maximum of the $1s \rightarrow 3d$ absorption is shifting to higher energy with increasing solution pH. However, the area of the absorption peak is decreasing with increasing solution pH, especially at pH = 6 and 12, where also the intensity of the Cu^+ feature is largest. This behavior is indicative for the formation of Cu^+ , as in Cu^+ the $1s \rightarrow 3d$ transition cannot occur.

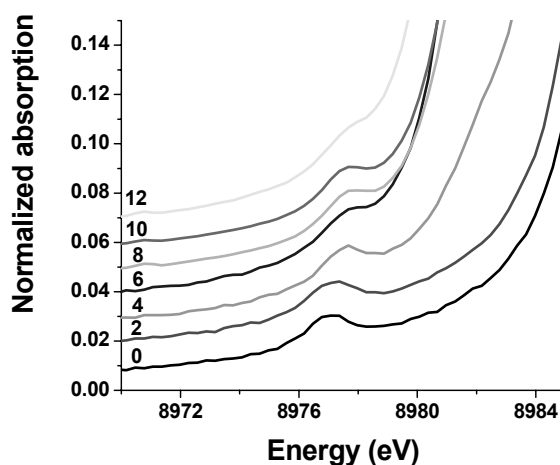


Figure 5: The development of the $1s \rightarrow 3d$ feature in the XANES of Cu^{2+} /His solutions (measured at ID26) as a function of the solution pH, indicated by the numbers 0-12.

To obtain X-ray absorption spectra with a good signal to noise ratio every solution was measured three times, after which the three resulting spectra were averaged. Thus it is possible to check whether there is a development in time of the intensity of the feature at 8982.5 eV at each pH value. However, the intensity of the feature was found to be independent on time.

The first intense transition in an X-ray absorption spectrum of a Cu(II) complex occurs at 8986 eV (position C, Figure 1). The assignment of this feature remains controversial and it could be either a vibronically allowed $1s \rightarrow 4s$ transition,^{10, 11} a $1s \rightarrow 4p$ transition or a $1s \rightarrow 4p$ with a simultaneous ligand-to-metal shakedown transition.^{9, 12} It was shown by Strange *et al.* that this feature primarily arises as a result of scattering by the axial ligands and that its intensity is related to the number and position of these ligands.⁶ Garcia *et al.* claim that the energy separation between the features at positions C and D gives a measure of the degree of

tetragonal distortion.¹³ At position C (in the area 8985-8987 eV) there are a number of differences in the spectra (measured at DUBBLE) of the solutions of the various Cu^{2+} complexes (see Figure 6).

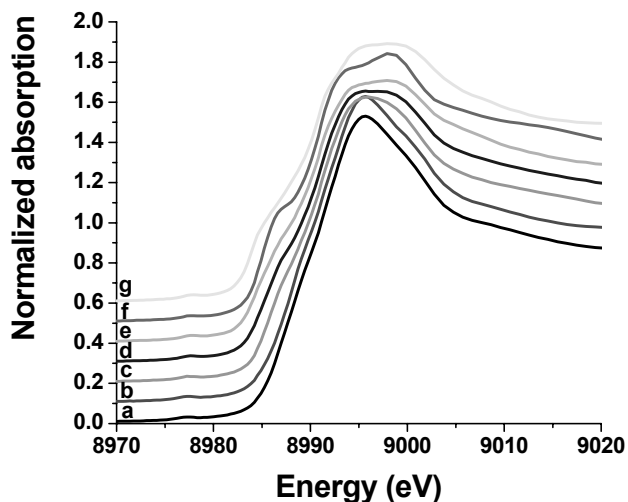


Figure 6: The XANES regions of the spectra of the Cu^{2+} complexes collected at the DUBBLE beamline: (a) Cu^{2+} nitrate, (b) Cu^{2+} Him 3.8, (c) Cu^{2+} Gly 3.8, (d) Cu^{2+} (His) 3.8, (e) Cu^{2+} (Gly) 7.3, (f) Cu^{2+} (His) 7.3 and Cu^{2+} (Him) 7.3. The numbers (3.8 and 7.3) indicate the pH of the solution.

The C feature has a higher energy and is located the same position in the absorption spectra of the copper nitrate and the Cu^{2+} /Him solutions at pH = 3.8. This strongly indicates that Him is not coordinating to copper at that specific pH value and that the coordination environment around the Cu^{2+} cation is the same as in the copper nitrate solution, *viz.* a copper hexa-aqua complex. However, for Cu^{2+} /His and Cu^{2+} /Gly the feature shifts to lower energy, a bit more for the Cu^{2+} /His solution compared to the Cu^{2+} /Gly solution. When the solution pH is 7.3 the feature is also present and quite broad with Cu^{2+} /Him. The feature in Cu^{2+} /Gly at pH = 7.3 is less broad, but higher in intensity. The intensity and the broadness of the feature in the Cu^{2+} /His solution are somewhere in-between and do not differ much from the situation at pH = 3.8, although the intensity is slightly higher at higher pH. It is difficult to observe a trend in the features at position C as a function of the solution pH. It can only be concluded that the position of the feature is related to the coordination of nitrogen atoms in the equatorial plane around the Cu^{2+} cation, since the feature is positioned at a slightly higher energy for the solutions containing the copper hexa-aqua complex.

The absorption edge maximum, labeled D in figure 1, corresponds to the allowed $1s \rightarrow np$ ($n \geq 4$) transitions, which merge into the continuum at higher energy.¹⁰ There are quite some differences between the samples measured at DUBBLE in the region between 8990 and 9000 eV (Figure 6). The copper nitrate and Cu^{2+} /Him solutions display the highest absorption at pH 3.8, whereas the histidine solution has the lowest absorption. The absorption intensity in region D is higher for solutions at pH 3.8 than in is for the solutions at pH = 7.3. At pH = 7.3 there is not much difference in absorption intensity in this region. From the absorption spectra at this pH it is obvious that two different absorption bands contribute to the absorption profile in region D. Nevertheless, there is a small difference in the relative contribution of the two absorption bands to the absorption in region D in the different solutions at pH = 7.3. For the Cu^{2+} /His solution the intensity of the second band is significantly stronger than the intensity of the first band, whereas the intensity of the two bands is about the same for the other two solutions.

At position E in Figure 1 features can be present that are supposed to originate from continuum resonances involving multiple scattering effects. It is reported that orientation of imidazole rings relative to the equatorial plane of the Cu^{2+} complex may give more or less intense absorptions at position E.⁶ Only the Cu^{2+} /Gly solution at pH = 7.3 has some increased intensity in this region. As the Gly ligand does not possess an imidazole moiety, the increased intensity can not be caused by continuum resonances involving multiple scattering effects in the imidazole ring. Therefore it is possible that coordination of the imidazole ring gives rise to a *lowering* of the intensity in this region.

5.4 Discussion

From the results it is clear that a distinction has to be made between Cu^{2+} /His solutions studied at beamlines with a low photon flux and Cu^{2+} /His solutions studied at beamlines with a high photon flux. This is again an illustration of the conclusions in chapter 2 that the synchrotron X-ray beam used for X-ray absorption measurements may influence the sample under study. The main difference in the X-ray absorption spectra for samples studied at a low-flux beamline and samples that are measured at high-flux beamlines is the presence of a feature at 8982.5 eV in the latter. The intensity of this feature depends on the solution pH and

does not increase in time at a specific pH value. Thus the change that is inflicted to the $\text{Cu}^{2+}/\text{His}$ system by the high-flux beamlines results in a stable situation, possibly an equilibrium. This situation is reached very quickly, as the spectra that are recorded at ID24 are collected within 12 s and they show no significant difference compared to the absorption spectra that are collected at the same pH during a much longer time at ID26. What is the physical background of the upcoming of the feature at 8982.5 eV? Based on the position of the pre-edge feature the formation of a Cu^+ species is suggested.⁹ This is supported by the fact that the area of the $1s \rightarrow 3d$ absorption peak decreases with increasing intensity of the 8982.5 eV feature. Since the d-orbitals of the Cu^+ species are completely filled, the $1s \rightarrow 3d$ transition cannot occur.

There are three different possible pathways *via* which the reduction of copper in the $\text{Cu}^{2+}/\text{His}$ complex can occur, two of which involve hydrated electrons. The first pathway is direct reduction of Cu^{2+} by a hydrated electron. The hydrated electron has a very negative reduction potential (-2.9 V vs. SHE).¹⁴ Hydrated electrons can be generated by the radiolysis of water under influence of (X-ray) radiation. The radiolysis process is, amongst others, a function of the flux of the incoming X-rays. The second reduction pathway follows *via* an indirect mechanism, in which the hydrated electron is taken up and transported to Cu^{2+} by the ligands that coordinate to the Cu^{2+} . The third pathway involves reduction of Cu^{2+} by a radical species that is generated under influence of the X-ray beam. This radical species may be a product from the radiolysis process, but may also be generated as a result of direct radiation damage to the histidine ligands that coordinate to the copper cation.

In all pathways the role of the ligands that coordinate to Cu^{2+} is very important. The ligands may physically block reactive species from approaching Cu^{2+} for direct interaction. Furthermore, the ligating species influence the redox potential of the copper cation, thus making it easier or more difficult for reduction of Cu^{2+} to occur. The ligands can also act as a mediator for the transport of an electron to Cu^{2+} . So, it is important to focus on the His ligand when trying to explain the observed phenomena and trends.

His coordination to transition metal ion complexes occurs in many metalloproteins that are active in redox processes. Most of the times coordination occurs *via* the imidazole group of histidine, as both the carboxyl group and the amino group are incorporated into the peptide backbone of the protein. Hence the combination of a transition metal ion and one or

more imidazole rings is an important theme in biochemical redox processes. Therefore it should not be surprising that there is a relationship between coordination of the imidazole groups of histidine to Cu²⁺ and the susceptibility of the Cu²⁺/His complexes towards reduction under influence of the X-ray beam.

The development of the intensity of the Cu⁺ pre-edge feature at 8982.5 eV as a function of the solution pH roughly follows the concomitant shift of the maximum of the d-d transition band in UV/Vis. This UV/Vis absorption band shifts to higher energy up to pH = 5, than shifts back to lower energy for intermediate pH levels and finally shifts again to higher energy for solutions with pH >10. This behavior indicates that the upcoming of the pre-edge as a function of the solution pH is related to the coordination mode of the His ligands to Cu²⁺.

In the previous chapter it was concluded that coordination of the imidazole group started at a pH of about 3.5 and that it was fully coordinating at a pH of about 5.5. The intensity of the Cu⁺ feature is at its maximum in this pH interval, so involvement of the imidazole ring in the reduction mechanism is very plausible. EXAFS analyses revealed that the distance of the equatorially coordinating atoms is larger for solutions in the pH range 6-8 than it is for solutions at lower pH. This observation can explain the decrease of the intensity of the Cu⁺ feature in this region, as the influence of the coordinating imidazole groups on the copper cation decreases with increasing distance. It was proposed in the previous chapter that the increase of the distance in the equatorial plane is caused by an increased axial coordination of the carboxyl moiety. The replacement of a very mobile water molecule at the axial position by a much more rigid oxygen from the carboxyl groups makes a direct approach of the copper cation by reducing species (like the hydrated electron or other radicals) much more difficult.

So, different factors contribute to the reducing influence of the synchrotron X-ray beam on Cu²⁺/His solutions. The first factor is coordination of the imidazole moiety to Cu²⁺. The second factor is the distance between this imidazole moiety and Cu²⁺. Directly related to this is the coordination of the carboxyl moiety in an axial position.

5.5 Conclusions

The XANES region of aqueous Cu^{2+} /His solutions provides information on the molecular structure of the Cu^{2+} /His complex as a function of the solution pH. The position and the area of feature A provide information on the ligand field splitting and on the oxidation state of the copper, respectively. Feature B also provides information on the oxidation state of the copper. This feature was present in the Cu^{2+} /His samples that were studied at beamlines with a high photon flux and its intensity was dependent on the pH. Next to the results of Chapter 4, the phenomena described in this Chapter, *viz.* X-ray-beam induced pH-dependent reduction, provide additional information on the structure of the Cu^{2+} /His system in solution, since the extent of the reduction is related to the coordination geometry of the Cu^{2+} /His complex. The reduction process was found to be dependent on imidazole coordination and on the distance of the imidazole towards the Cu^{2+} .

Acknowledgements

The European Synchrotron Radiation Facility (ESRF, Grenoble, France) and Hasylab (Hamburg, Germany) are acknowledged for the provision of synchrotron radiation facilities. We thank G. Guilera, S. Fiddy and S. Pascarelli (ID24, ESRF), L. Alvarez and T. Neisius (ID26, ESRF), M. Borowski (BM29, ESRF) and W. Bras and S. Nikitenko of DUBBLE (BM26A, ESRF) for their help and discussion during the experiments. Financial support from NWO/CW - Van der Leeuw, NRSC-C and NWO/CW-VICI is gratefully acknowledged.

References

- [1] K. Ozutsumi, Y. Miyata and T. Kawashima, *J. Inorg. Biochem.* **44** (1991) 97.
- [2] F. Carrera, E. S. Marcos, P. J. Merklings, J. Chaboy and A. Muñoz-Páez, *Inorg. Chem.* **43** (2004) 6674.
- [3] R. W. Strange, N. J. Blackburn, P. F. Knowles and S. S. Hasnain, *J. Am. Chem. Soc.* **109** (1987) 7157.

- [4] J. G. Mesu, A. M. J. van der Eerden, F. M. F. de Groot and B. M. Weckhuysen, *J. Phys. Chem. B* **109** (2005) 4042.
- [5] G. Onori, A. Santucci, A. Scafati, M. Belli, S. D. Longa, A. Bianconi and L. Palladino, *Chem. Phys. Lett.* **149** (1988) 289.
- [6] R. W. Strange, L. Alagna, P. Durham and S. S. Hasnain, *J. Am. Chem. Soc.* **112** (1990) 4265.
- [7] M. Sano, S. Komorita and H. Yamatera, *Inorg. Chem.* **31** (1992) 459.
- [8] K.-I. Shimizu, H. Maeshima, H. Yoshida, A. Satsuma and T. Hattori, *Phys. Chem. Chem. Phys.* **3** (2001) 862.
- [9] L.-S. Kau, D. J. Spira-Solomon, J. E. Penner-Hahn, K. O. Hodgson and E. I. Solomon, *J. Am. Chem. Soc.* **109** (1987) 6433.
- [10] J. M. Brown, L. Powers, B. Kincaid, J. A. Larrabee and T. G. Spiro, *J. Am. Chem. Soc.* **102** (1980) 4210.
- [11] W. E. Blumberg, J. Peisach, P. Eisenberger and J. A. Fee, *Biochemistry* **17** (1978) 1842.
- [12] P. D'Angelo, E. Bottari, M. R. Festa, H.-F. Nolting and N. V. Pavel, *J. Phys. Chem. B* **102** (1998) 3114.
- [13] J. Garcia, M. Benfatto, C. R. Natoli, A. Bianconi, A. Fontaine and H. Tolentino, *Chem. Phys.* **132** (1989) 295.
- [14] G. V. Buxton, G. L. Greenstock, W. P. Helman, A. B. Ross and W. Tsang, *J. Phys. Chem. Ref. Data* **17** (1988) 513.

Chapter 6

Host-Guest Chemistry of Zeolite-encaged Cu²⁺/Histidine Complexes

Abstract

Structural analysis has been carried out on copper(II) histidine (Cu²⁺/His) complexes after immobilization of the complexes in the pore system of the zeolites NaY and dealuminated Y (DAY) by means of ion exchange. The aim of this study was to determine the geometrical structure of Cu²⁺/His complexes after encaging, in order to obtain insight into both the effect of the zeolite matrix on the molecular structure and the properties of the immobilized complexes. Next to N₂ physisorption and XRF analyses, a combination of UV/Vis/NIR, ESR, X-ray absorption, IR and Raman spectroscopy has been used to obtain complementary information on both the first coordination shell of the copper ion and the orientation of the coordinating His ligands. Vibrational spectroscopy appeared to be insufficiently sensitive to obtain structural information on the complexes, but the data were useful to determine an intra-zeolitic “pH-value” of 5. With the UV/Vis/NIR, ESR and X-ray absorption data it was demonstrated that two complexes (**A** and **B**) are formed, in which two His ligands are coordinating to the central Cu²⁺ ion. The absolute and relative abundance of **A** and **B** depends on the Cu²⁺ concentration in the Cu²⁺/His solution used for ion exchange. A mechanism for the immobilization of both complexes is proposed. In complex **A** one ligand coordinates in a glycine-like fashion, *via* N_{am} and O_c, and the other one *via* the imidazole ring (N_{im}), while the complex is anchored to an oxygen atom of the support *via* the fourth position

in the equatorial plane. In complex **B** one His ligand is coordinated in a histamine-like fashion *via* N_{am} and N_{im} and the other one in a glycine-like fashion *via* N_{am} and O_c. The geometrical structure of both complexes differs from the preferred structure of Cu²⁺/His complexes in aqueous solution, which implies that the zeolite host material affects the coordination and orientation of the guest molecules. Therefore this type of support materials can be used to stabilize transition metal ion complexes which do not form the preferred species in aqueous environment. These results provide new perspectives for the design of catalyst materials with novel applications.

6.1 Introduction

Enzymes reflect in many respects the properties of an ideal catalyst. They operate at ambient conditions and combine high activity and selectivity with an unbeaten efficiency. A disadvantage, however, is their limited thermal stability and chemical resistance. For that reason the development of a more robust catalyst that matches the performance and properties of an enzyme is the ultimate dream of many catalyst researchers. A first step in realizing this dream is obtaining fundamental insight into the chemistry of enzymes, for instance by studying a compound that largely resembles (one of) the active sites of the enzymes. As outlined in the previous chapters, complexes of Cu²⁺ ions with histidine (His) moieties are commonly known to play a key-role in many metallo-enzymes,¹ and for that reason Cu²⁺/His species have been studied as model compounds to obtain knowledge on the working mechanism of redox-active enzymes.² As a logical next step towards the design of bio-inspired heterogeneous industrial catalysts, a lot of research has been conducted on the incorporation of Cu²⁺/His complexes in inorganic hosts such as zeolites and clay minerals.²⁻⁷ Immobilization of these complexes, in the micropores of a zeolite, for instance, provides a structural analogue for the active site of galactose oxidase.^{2, 4} Besides, the pore structure of the zeolite introduces shape selectivity in the reactions and allows *intra*-particle transport of reactants and products. Furthermore, the host material supplies additional stability to the incorporated active center, thereby expanding the physical and chemical resistance of the catalyst. The catalytic potential of zeolite Y encaged materials has already been demonstrated for the epoxidation of alkenes and for the oxidation of alcohols in the presence of *tert*-butyl hydroperoxide at 60 °C.⁷

Structural analysis to determine the coordination geometry of zeolite-encapsulated Cu²⁺/His complexes has been carried out with a number of different characterization techniques, *viz.* UV/Vis/NIR spectroscopy,^{6, 7} X-band Electron Spin Resonance (ESR) spectroscopy,^{3, 6, 7} Electron Spin Echo Envelop Modulation^{3, 6} (ESEEM) and high-field (W-band) pulsed electron-nuclear double resonance (ENDOR) analysis.^{3, 6} X-band ESR analysis revealed the presence of two different Cu²⁺/His species of which the relative amount appeared to be a function of the copper concentration in the ion exchange solution.^{6, 7} The ¹⁴N superhyperfine splitting pattern of one of the complexes indicated that three nitrogen atoms are coordinating to the copper cation,⁶ which was confirmed by UV/Vis measurements.^{6, 7} The other complex was concluded to be anchored to the zeolite framework *via* an oxygen atom, as ESEEM showed an intense ²⁷Al modulation. This technique also provided proof for the coordination of an imidazole nitrogen in both complexes.⁶ From advanced pulsed ESR and ENDOR analyses, the second complex was initially proposed to have only one His ligand coordinating to Cu²⁺ *via* two nitrogen atoms, while the other equatorial positions were occupied by oxygen atoms from a water molecule and from the support. Later on this proposal was adjusted by replacing the coordinating water molecule for the oxygen of a carboxyl group of a second His ligand.³

Despite the consensus in literature on most of the coordination chemistry of Cu²⁺/His in the supercages of zeolite Y, the precise effect the host material has on the coordinating preferences of Cu²⁺/His complexes is still not fully understood. However, knowledge of this effect is essential, as it may influence the catalytic properties of the transition metal ion complex after immobilization. As a logical continuation of the research on the Cu²⁺/His complexes in aqueous solution described in previous chapters, we decided to carry out a model study on a series of these solid samples in order to obtain insight into the host-guest chemistry of the Cu²⁺/His/zeolite system.

It has been shown that X-ray absorption, infrared (IR) and Raman spectroscopy can be valuable tools to obtain complementary information not only on the local structure around the central copper ion, but also on the state of protonation of the His ligand. For that reason we decided to use these techniques in addition to UV/Vis/NIR- and ESR-spectroscopy to study the structural behavior of Cu²⁺/His complexes upon immobilization in the zeolite pores. Four different Cu²⁺/His concentrations have been used for ion exchange on zeolite NaY to the

determine effects of the $\text{Cu}^{2+}/\text{His}$ loading on the structure and the relative abundance of the immobilized complexes. In addition, two samples of $\text{Cu}^{2+}/\text{His}$ immobilized on de-aluminated zeolite Y (DAY) have been prepared to study the influence of the Si/Al ratio of the support. As a result, a better understanding of the host-guest chemistry in this type of bio-inspired heterogeneous catalysts is obtained.

6.2 Experimental

6.2.1 Sample preparation

Two commercially available zeolite support materials have been ion exchanged with copper histidine ($\text{Cu}^{2+}/\text{His}$): NaY zeolite (AKZO Nobel, Si/Al ratio = 2.5, micropore volume = 0.34 ml/g) and DAY zeolite (Wessalith, Si/Al ratio = 100, micropore volume = 0.29 ml/g). The DAY zeolite material is a Y-type zeolite having a faujasite structure with a very high Si/Al ratio. The zeolite was prepared *via* a special SiCl_4 treatment that yields a Y zeolite in which almost all of the aluminum sites have been occupied by silicon. However, the properties of the framework have been fully retained, whereas medium-sized pores and defects are absent. Therefore this type of zeolite exhibits enhanced temperature stability and improved hydrophobic properties.

The NaY zeolite was exposed to solutions of $\text{Cu}^{2+}/\text{His}$ (1:5) with Cu^{2+} concentrations of $6.5 \cdot 10^{-5}$, $1.3 \cdot 10^{-4}$, $3.9 \cdot 10^{-4}$ and $1.2 \cdot 10^{-3}$ M, which corresponds to respectively 0.25, 0.5, 1.5 and 4.5 copper atoms per unit cell (Cu/UC) of the zeolite Y material. For DAY concentrations corresponding to 0.25 and 4.50 Cu/UC were used. First, equilibration of 5 g NaY in 1 l of demineralized water was performed for 3 h at pH = 7.3. The pH was adjusted using solutions of 0.1 M NaOH and/or 0.1 M HNO_3 . Next, an aqueous solution containing $\text{Cu}(\text{NO}_3)_2 \cdot 3\text{H}_2\text{O}$ (Merck, *p.a.*) and L-histidine (Acros Organics) in a 1:5 ratio at pH = 7.3 was added and the mixture was stirred for 48 h at room temperature. The pH of the solution was kept constant at pH = 7.3 by adding NaOH or 0.1 M HNO_3 when necessary. In the next step the exchanged zeolitic material was isolated by vacuum filtration, washed three times with demineralized water and dried at 60°C for 24 h. The same procedure, only without the addition of $\text{Cu}(\text{NO}_3)_2 \cdot 3\text{H}_2\text{O}$, was followed to obtain His/NaY and His/DAY as reference materials. Additional ion exchange experiments were carried out to determine the effect of the ion

exchange time on the amount of Cu²⁺ complexes exchanged into the zeolitic material, but no significant increase was observed for longer exchange times (data are not presented).

6.2.2 Characterization

Prior to spectroscopic characterization nitrogen physisorption experiments were carried out to determine changes in the zeolite pore volume as result of ion exchange with Cu²⁺/His. After degassing the solid samples for 24 hours at 100°C in vacuum, analyses were performed at 77 K with a Micromeritics ASAP 2400 apparatus. The micropore volumes were determined using the t-plot method.

X-ray fluorescence (XRF) analysis was carried out to establish the exact copper contents of the samples after immobilization of Cu²⁺/His. Measurements were performed using a Spectro X-lab 2000 spectrometer. From the data the numbers of Cu²⁺ atoms per unit cell of zeolite Y were calculated.

UV/Vis/NIR measurements were carried out in diffuse reflectance mode with a Cary-500 spectrophotometer (Varian), equipped with an integrating sphere. Bare NaY zeolite powder was used as a white background. The spectra were recorded in the range 50000 to 10000 cm⁻¹.

X-band ESR spectra were recorded on a Bruker ESP300 apparatus and on a Bruker ESP300E apparatus, both operating near 9.5 GHz. The samples were recorded at 120 K in a quartz tube. Data acquisition and spectral manipulation were performed using the instrument software. Spectral simulation was carried out using the commercially available Symphonia software. The shape of each sub-spectrum was chosen as a molecule with an axial Zeeman interaction plus an axial hyperfine interaction to the copper nucleus ($I = 3/2$). The experimental accuracy did not require simulation as a mixture of ⁶³Cu/⁶⁵Cu isotopes.

X-ray absorption measurements on the Cu²⁺/His/NaY samples with the lowest copper concentrations (samples **a** and **b**, Table 1) were collected in the fluorescence mode at wiggler station X1.1 of Hasylab (Hamburg, Germany), using a Si(111) double crystal monochromator. The monochromator was detuned to 50% of the maximum intensity to avoid higher harmonics in the X-ray beam. The Cu²⁺/His/NaY samples with higher copper concentrations (samples **c** and **d** in Table 1) were measured in transmission mode at beamline BM29 of the ESRF (Grenoble, France), using a Si(111) double crystal monochromator. Higher harmonic

rejection was performed by detuning both monochromator crystals by 50%. Additional X-ray absorption spectra of all Cu²⁺/His/NaY samples were measured at beamline BM26a at ESRF/DUBBLE (Grenoble, France). These spectra were collected in the fluorescence mode at a 90-degree orientation with respect to the incident X-ray beam, using a nine-channel monolithic germanium detector. A Si(111) monochromator crystal was used. For all experiments the samples were pressed into self-supporting wafers and placed in a controlled-atmosphere cell, which was flushed with Ar at room temperature prior to measurements. The spectra were collected at 77 K and several scans were averaged to improve the signal to noise ratio of the data. A description of the methods used for EXAFS analysis can be found in the experimental section of Chapter 4.

IR spectra were recorded at room temperature on a Perkin-Elmer 2000 FTIR spectrometer equipped with a DTGS detector. Samples were prepared as KBr-pellets and for each spectrum 256 scans were accumulated at a data point resolution of 2 cm⁻¹ (optical resolution = 4 cm⁻¹). The spectrum of dried air was used as background.

Raman measurements were carried out on a Perkin-Elmer 2000 FT-Raman system equipped with an InGaAs detector and a 1064 nm NdYag laser for excitation. Scanning was performed in backscattering mode at an laser output power of 100 mW and a data point resolution of 4 cm⁻¹ (optical resolution 8 = cm⁻¹). For each spectrum 500 scans were accumulated and averaged. Spectral subtraction procedures were applied for both IR and Raman in order to compensate for bands of the support material.

6.3 Results

6.3.1 N₂ physisorption

The N₂ physisorption isotherms were found to be Langmuir type I. Table 1 summarizes the micropore volumes of the different Cu²⁺/His/Y samples. The micropore volume decreases from 0.34 ml/g for sample **a** (with the lowest loading, 0.183 Cu/UC) to 0.29 ml/g for sample **d** with the highest copper loading (0.820 Cu/UC). For the Cu²⁺/His/DAY samples **e** and **f** no significant decrease in micropore volume was observed with increasing Cu²⁺ loading.

6.3.2 XRF analysis

As appears from Figure 1 and Table 1, the copper content in the zeolite material, as determined by XRF spectroscopy, increases proportionally to the Cu²⁺/His concentration in the ion exchange solution up till a value of 1.5 Cu/UC (0.683 Cu/UC after immobilization). At a solution concentration of 4.5 Cu/UC the limit in the number of available sites in the zeolite cages seems to be reached. This number is approximately 0.8 Cu²⁺ ions per unit cell.

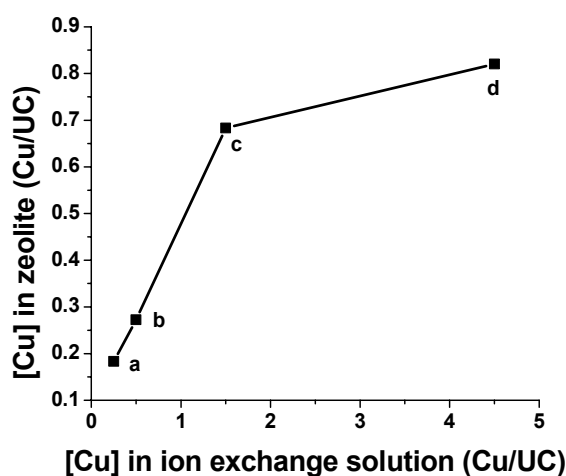


Figure 1. Copper loadings in zeolite Y as a function of the Cu²⁺ concentration in the ion exchange solution: (a) 0.183, (b) 0.272, (c) 0.683 and (d) 0.820 Cu/UC. X-axis: hypothetical value, if all available Cu²⁺ were to be exchanged into the zeolite, Y-axis: actual Cu²⁺ concentration in the zeolite after ion exchange.

6.3.3 UV/Vis/NIR spectroscopy

The UV/Vis/NIR spectra of the zeolite Y samples are presented in Figure 2. The spectra display strong absorption bands in the UV part of the spectrum, at 46000 and 36000 cm⁻¹ and a weaker one in the visible part of the spectrum at 15000 cm⁻¹. On increasing the Cu²⁺ loading the band at 46000 cm⁻¹ remains fixed in position and increases in intensity. Furthermore, the band at 36000 cm⁻¹ also gains intensity but additionally shifts to higher energy (40000 cm⁻¹). The band at 15000 cm⁻¹ can be assigned to the Cu²⁺ d-d transition band and is shown in expanded view as an insert in Figure 2. For obvious reasons the intensity of this band increases with Cu²⁺ loading, but it should be noted that this intensity increase cannot be used straightforwardly for quantification, as the intensity of the d-d transition is also a

function of the molecular structure and geometry of the $\text{Cu}^{2+}/\text{His}$ complex. The position of the d-d transition band shifts from 14500 cm^{-1} to 15300 cm^{-1} when the $\text{Cu}^{2+}/\text{His}$ content in the zeolite increases.

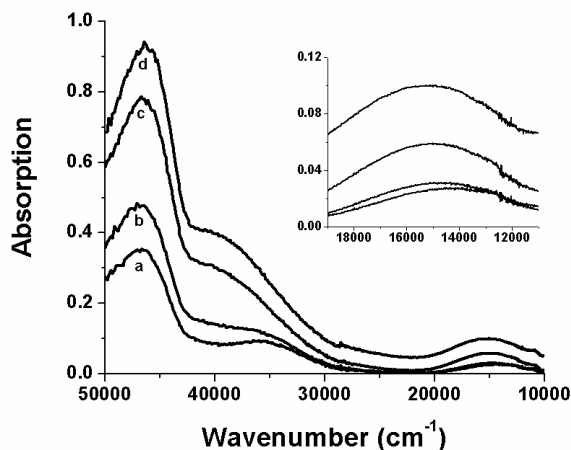


Figure 2. UV/Vis/NIR absorption spectra of $\text{Cu}^{2+}/\text{His}$ immobilized in zeolite Y at actual Cu^{2+} loadings of (a) 0.183, (b) 0.272, (c) 0.683 and (d) 0.820 Cu/UC . The insert shows the Cu^{2+} d-d transition band.

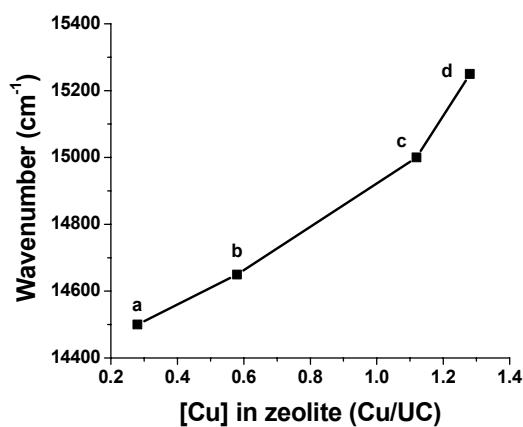


Figure 3. Development of the maximum of the d-d transition band of $\text{Cu}^{2+}/\text{His}/\text{Y}$ as a function of the Cu^{2+} loading: (a) 0.183, (b) 0.272, (c) 0.683 and (d) 0.820 Cu/UC .

A plot of the peak position of the d-d transition vs. the Cu^{2+} loading, as shown in Figure 3, reveals that this relation is not linear. This points to the presence of at least two different Cu^{2+} species in the zeolite, of which the ratio changes with Cu^{2+} loading. Finally, it should be noted that the precise position of the d-d transition band is sensitive to the state of hydration of the

zeolite matrix. Upon drying in a desiccator a red-shift of the band was observed, whereas rehydration of the samples resulted in a back-shift to the original position.

6.3.4 ESR analysis

The first derivatives of the X-band CW-ESR absorption spectra of the Cu²⁺/His/Y samples are shown in Figure 4.

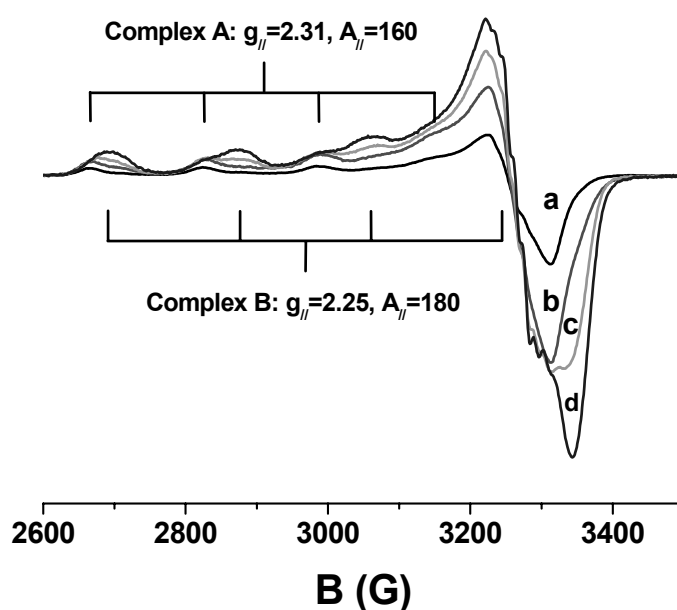


Figure 4. First derivative CW-ESR spectra of Cu²⁺/His immobilized in zeolite Y at different copper loadings: (a) 0.183, (b) 0.272, (c) 0.683 and (d) 0.820 Cu/UC.

It is evident from the spectra that free Cu²⁺ is absent, since a species with the ESR parameters for Cu²⁺ on zeolite Y ($g_{||} = 2.39$, $A_{||} = 129$) is not observed. Thus all copper must be coordinated to His. The spectra reveal the contribution of two distinct ESR sub-spectra, which implies that at least two different Cu²⁺/His complexes, **A** and **B**, must be present in the zeolite support. The absolute abundances of the two complexes were determined from the ESR spectra and the results are presented in Figure 5 as a function of Cu²⁺ loading in the zeolite. Obviously, the total number of complexes (**A+B**) increases with the Cu²⁺ concentration, but it is apparent that the ratio (**A:B**) changes too. At low loadings complex **A**

is the major species, whereas **B** becomes the prevailing complex at a high copper content. The optimized values for both complexes are presented in Table 1 and complex **A** is shown to have a higher $g_{//}$ and a lower $A_{//}$ value than complex **B**. The same complexes **A** and **B** were also found to be present in the $\text{Cu}^{2+}/\text{His}/\text{DAY}$ samples. The corresponding ESR parameters and the relative abundances of the two complexes in all samples are summarized in Table 1.

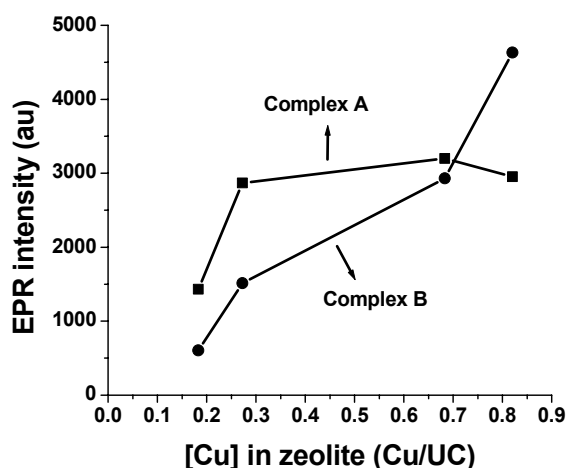


Figure 5. The absolute distribution of complex **A** (-■-) and complex **B** (-●-) in $\text{Cu}^{2+}/\text{His}/\text{Y}$ (based on ESR results) as a function of the copper concentration in the zeolite.

Table 1. Results of chemical and spectroscopic characterizations and ESR simulation data of $\text{Cu}^{2+}/\text{His}$ -loaded zeolite samples.

Sample	[Cu] (M)	Si/Al	XRF [Cu] zeolite (Cu/UC)	N ₂ physisorption Micropore volume (ml/g)	UV/Vis d-d band maximim (cm ⁻¹)	Complex A			Complex B		
						Rel. Abund (%)	$g_{//}$	$A_{//}$ (G)	Rel. Abund. (%)	$g_{//}$	$A_{//}$ (G)
a	0.25	2.5	0.183	0.34	14500	80			20		
b	0.50	2.5	0.272	0.32	14650	65	2.31	160	35	2.25	180
c	1.50	2.5	0.683	0.32	15000	50			50		
d	4.50	2.5	0.820	0.29	15250	40			60		
e	0.25	100	0.046	0.28	15675	60	2.31	160	40	2.25	180
f	4.50	100	0.112	0.28	16100	30			70		

The exact number of nitrogen atoms in the first coordination sphere around the Cu^{2+} cation was established for each of the samples **a-f** by investigating the splitting pattern in the

hyperfine region of the ESR spectra. As an example the hyperfine region of the Cu²⁺/His/Y samples with the lowest (**a**) and the highest (**d**) copper loading are shown in Figure 6.

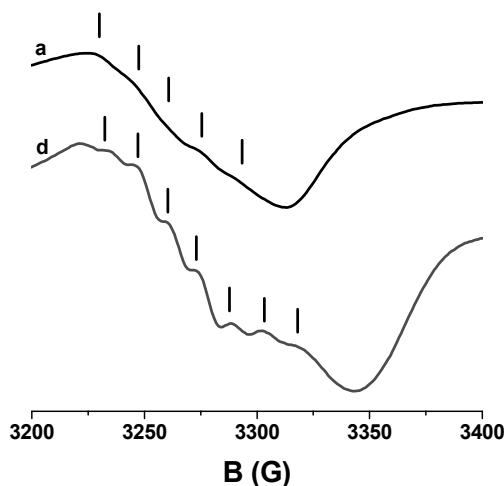


Figure 6. The superhyperfine region of the first derivative CW-ESR spectra of Cu²⁺/His immobilized in zeolite Y at two different loadings: (a) 0.183 Cu/UC and (d) 0.820 Cu/UC.

For sample **a** a five fold hyperfine splitting pattern is observed, which points to the presence of two nitrogen atoms in the vicinity of the Cu²⁺ cation. In contrast, for sample **d** a seven-fold splitting pattern is established, which indicates the presence of three nitrogen atoms in the first coordination sphere. The same seven-fold superhyperfine splitting pattern was observed in the spectrum of the Cu²⁺/His/DAY sample **f**. The copper concentration in sample **e** was too low to obtain reliable conclusions.

6.3.5 EXAFS analysis

The EXAFS analyses on the Cu²⁺/His/Y and Cu²⁺/His/DAY samples revealed an average distance between the Cu²⁺ cation and the first coordination sphere of 1.96 Å for all samples. Additional information is obtained from the XANES regions of the normalized X-ray absorption spectra of the Cu²⁺/His/Y samples (**a-d**) as shown in Figure 7. There are small differences between the spectra, especially in the XANES regions B, C and D (see Chapter 5 for an explanation on the interpretation of these features). Samples **a** and **b** exhibit a slight increase in intensity at 8983 eV (region B) compared to samples **c** and **d**, whereas a pre-edge

feature in region C is more pronounced in the highly concentrated samples **c** and **d**. In order to determine the origin of these differences all samples were also measured in the fluorescence mode. The feature in the XANES B-region showed up again in the spectra of all samples and increased in intensity with exposure time to X-rays.

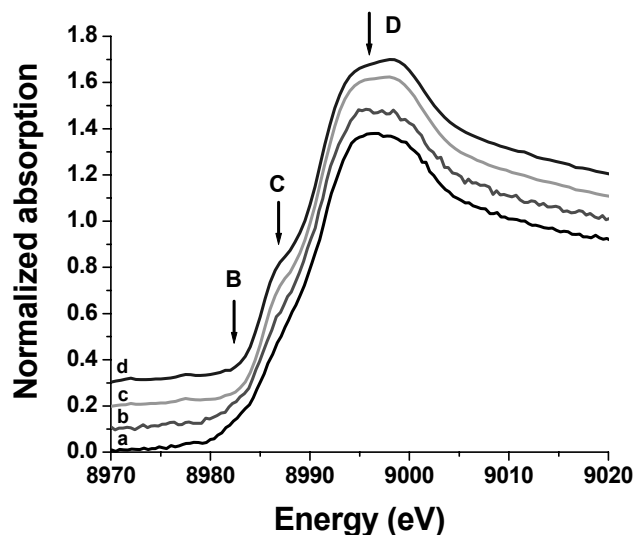


Figure 7. XANES region of the X-ray absorption spectra of $\text{Cu}^{2+}/\text{His}$ immobilized in zeolite Y at different copper loadings: (a) 0.183, (b) 0.272, (c) 0.683 and (d) 0.820 Cu/UC. An offset of 0.1 is used between the different spectra.

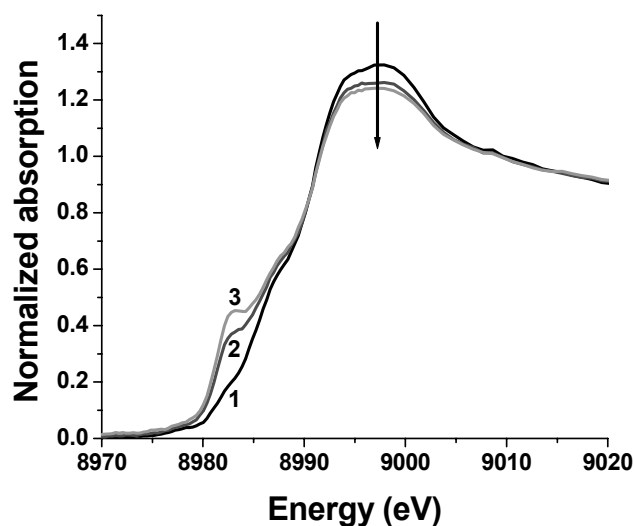


Figure 8. The development in time of the X-ray absorption near edge structure of the $\text{Cu}^{2+}/\text{His}/\text{Y}$ sample with the lowest copper concentration (sample **a**). The numbers 1, 2 and 3 indicate the successive measurements with a 45 min. time interval.

This is illustrated in Figure 8 with the spectra of sample **a**, obtained at three different points in time (with a 45 min. Time interval). As discussed in Chapter 2, the upcoming of this pre-edge feature can be assigned to the reduction of Cu²⁺ to Cu¹⁺ under influence of the X-ray beam. The observed phenomenon is most prominent in the low Cu²⁺-loaded samples **a** and **b**. In order to gain insight into the origin of this effect the normalized intensity of the Cu¹⁺ feature at 8983 eV has been plotted as a function of the X-ray exposure time in Figure 9 for all samples. Indeed, the reduction process proceeds faster for the sample with the lowest Cu²⁺/His loading. This confirms that the beam damage effect on complex **A**, predominantly at low concentration, is larger than on form **B**, which is the prevailing structure at high concentration. The deviating behavior of sample **c** in Figure 9 is not an artifact, but was due to a refill of the beamline between the successive measurements 1 and 2 on this sample. This observation endorses the fact that the damage is related to the flux of incoming X-rays. This finding is in agreement with the conclusions of Chapter 2 on the same phenomenon.

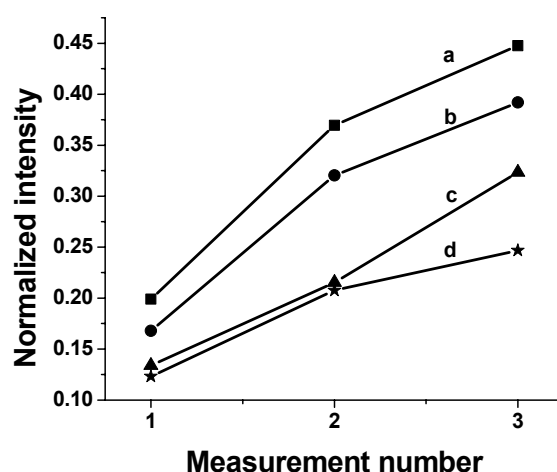


Figure 9. Effect of the X-ray exposure time on the development of the Cu¹⁺ pre-edge feature at 8983 eV in the X-ray absorption spectra of the Cu²⁺/His/Y samples with different copper loadings: (a) 0.183, (b) 0.272, (c) 0.683 and (d) 0.820 Cu/UC.

6.3.6 IR spectroscopy

The IR spectra of the Cu²⁺/His/Y and His/Y samples are dominated by the strong absorption characteristics of the zeolite Y support material. After subtraction of the spectrum of the bare NaY material the difference spectra of the samples **a** and **b** were too weak to be

useful for interpretation. A better signal to noise ratio was obtained particularly for sample **d** with the highest Cu^{2+} /His concentration but this spectrum appeared to be virtually identical to that of the reference compound His/Y. To illustrate this, the spectrum of sample **d** is presented in Figure 10 together with the spectra of the reference compound His/NaY and His in aqueous solution recorded at pH = 5. Because of interfering bands of the zeolite support only the range 1800-1200 cm^{-1} is shown. The same procedure was followed for the Cu^{2+} /His/DAY compounds, but interpretable spectra were not obtained because of the low Cu^{2+} /His concentrations in these samples.

6.3.7 Raman spectroscopy

As with IR, useful Raman spectra were only obtained for the Cu^{2+} /His/Y sample **d** with the highest Cu^{2+} /His loading (0.820 Cu/UC) and the reference compound His/NaY.

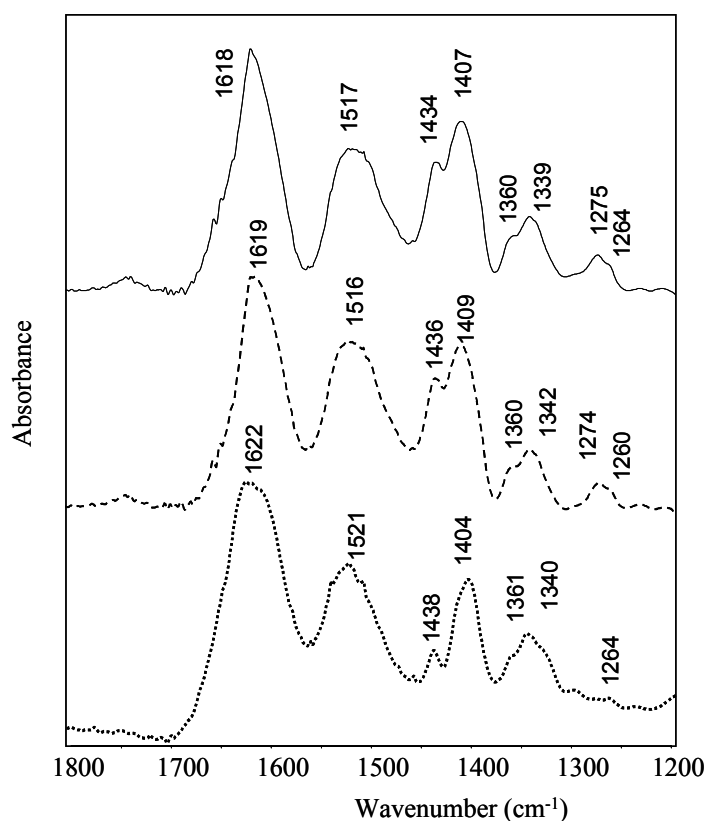


Figure 10. IR spectra of Cu^{2+} /His/Y (copper loading = 0.820 Cu/UC, top), His/NaY (middle) and His in aqueous solution at pH = 5 (bottom).

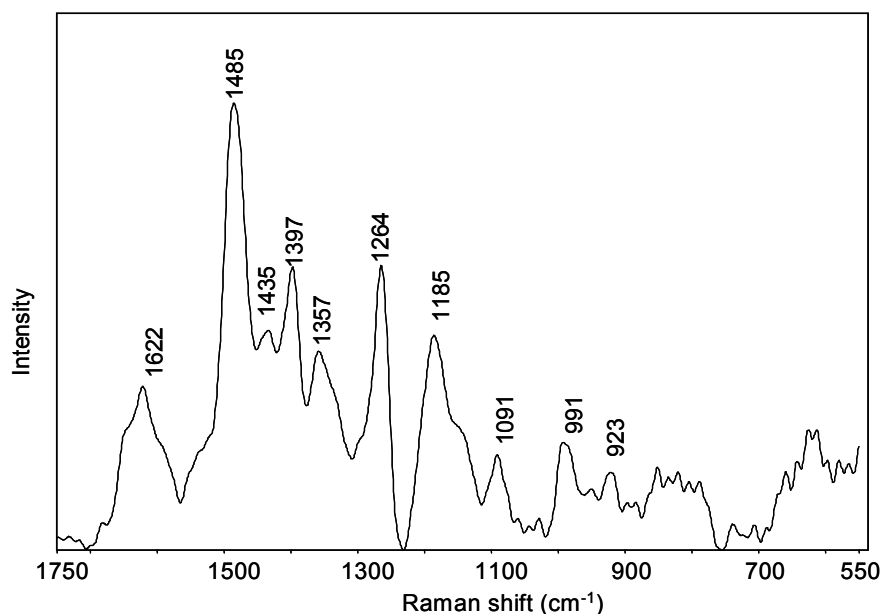


Figure 11. Raman spectrum of Cu²⁺/His immobilized in zeolite Y at a copper loading of 0.820 Cu/UC, after subtraction of the support spectrum.

The Raman spectrum of sample **d**, obtained after subtraction of the spectrum of pure NaY, is presented in Figure 11. Apart from minor intensity differences the spectrum is virtually the same as that of the His/NaY reference material after correction for the peaks of the support. Moreover, it largely resembles the Raman spectrum of His in aqueous solution recorded at pH = 5.

6.4 Discussion

The XRF results suggest a congestion of the zeolite pores by Cu²⁺/His complexes: According to the established Cu²⁺ loadings as determined with this technique, a maximum in the number of available sites in the zeolite cages seems to be reached around 0.8 Cu/CU. However, since there is an excess in the number of available unit cells in the support material, this must be the result of pore-blocking in the outer shells of the zeolite. A plausible mechanism is that most of the Cu²⁺/His complexes are immobilized in the outer pores of the zeolite crystals, thus hampering other ‘free’ Cu²⁺/His complexes to enter the micropore channels. This process continues until the outer coordination sphere of the zeolite particles is

completely filled. However, as will be discussed later on, we assume that the effect of pore blocking does not prevent the smaller free His ions from entering the zeolite cages.

6.4.1 Effects of the zeolite matrix

As already mentioned, the IR and Raman spectra of the $\text{Cu}^{2+}/\text{His}/\text{Y}$ samples **c** and **d** are very similar to the ones of the reference compound, in which only free His was ion exchanged onto the support. This is not surprising regarding the excess of His in the solutions that were used to prepare the samples. Referring to literature, it can be calculated that 80% of the His molecules are not complexed to Cu^{2+} , but are ion exchanged onto the support⁶. Consequently, the IR and Raman spectra represent mainly these non-complexed His species. However, as demonstrated in Chapters 3 and 4, IR and Raman can be used to determine the protonation state of the His molecules. This is dependent on the acidity of the local environment and thus, the vibrational spectra can be used to establish the “pH” within the zeolite matrix. The “pH” within the pore system of the zeolite material cannot be compared straightforwardly with the pH in an aqueous solution, as the environment in the two systems is different. But to get at least an idea of what is going on in the pores of the zeolite material we compared the IR and Raman spectra of Figures 8 and 9 with the data of His in aqueous solutions at different pH's. Referring to Chapter 3, the strong IR band at 1513 cm^{-1} proves that the primary amino group (N_{am}) is protonated, while the absence of a $\text{C}=\text{O}$ stretching band around 1735 cm^{-1} shows that the carboxyl group is the only site that is deprotonated. Regarding the pK_{a} value of both groups of 9.1 and 1.8, respectively, it follows that the pH must be between these two values. Furthermore, the strong bands at 1485, 1264, 1185 and 991 cm^{-1} in the Raman spectrum of Figure 9 can be attributed to the fully protonated form of the imidazole ring, which implies that this structural element is not involved in bonding of His to the support. The pK_{a} value of this group is 6.0 and so, the “pH” inside the zeolite must be below $\text{pH} = 6$. Further comparison of the spectral fingerprints of sample **d** with the spectra of His recorded in aqueous solution as a function of the pH (Chapter 3) reveals a striking similarity with the IR and Raman spectra obtained at $\text{pH} = 5$, which is well illustrated in Figure 8. Hence, it can be concluded that the “pH” inside the zeolite is also approximately 5. At this pH His is mainly

present in the ionic state [H₃His]⁺ and it is obvious to conclude that ion exchange of this species with Na⁺ will take place during the preparation of the samples.

Information on the chemical state of the host matrix can also be derived from the UV/Vis/NIR spectra. Comparison of the spectra of the Cu²⁺/His complexes immobilized in the zeolites with the ones of the Cu²⁺/His complexes in aqueous solution shows a difference in the position of the Cu²⁺ d-d transition band of about 1600 cm⁻¹. As described in Chapter 4, the complex with NNOO coordination has a maximum at 16100 cm⁻¹ (620 nm) in solution, whereas for the solid NNOO analogue (complex **A**, sample **a**), this maximum is found around 14250 cm⁻¹ (640 nm). In theory, the position of the band depends on the nature of the chelating atoms and their distances towards the central copper cation, but it is obvious that the matrix, *i.e.*, the solvent or the support, can affect this parameter. Apparently, the presence of the zeolite support results in a red shift of the d-d transition band of the Cu²⁺ complex. The effect of the matrix also explains the difference in peak position in the UV/Vis/NIR spectra that we measured before and after thorough drying of the Cu²⁺/His/Y samples. Since a zeolite matrix can adopt different states of hydration, this finding implies that it is, in principle, possible to change the properties of the guest complex (Cu²⁺/His) by adjusting the state of hydration of the host material.

Another effect of the support on the complexes can be derived from the EXAFS results. As we already noted, the reduction of Cu²⁺ upon exposure to the synchrotron beam is most prominent for the samples with low Cu²⁺ loadings, *i.e.* the samples with relatively the largest amount of complex **A**. However, normalizing the data for the relative abundance of complex **A** reveals that the reduction process proceeds in the same way in all samples, which indicates that only complex **A** is susceptible to the influence of the X-ray beam. This observation illustrates once more that the zeolite host material affects the chemistry of the guest complex: it increases the redox potential of the Cu²⁺/His complex **A**, thus facilitating the reduction of the Cu²⁺ cation by solvated electrons (with a reduction potential of -2.9 V vs. SHE) that are generated by the radiolysis of water in the pores of the zeolite material. The redox potential is higher for metal ions that are surrounded by more electronegative ligands. Therefore, it is also expected that complex **A** is more easily reduced than complex **B**, since there are more oxygen atoms (with a higher electronegativity) in the first coordination sphere around the Cu²⁺ cation in complex **A**. This hypothesis also explains the observed activity

trend in the catalytic experiments with zeolite-encaged $\text{Cu}^{2+}/\text{His}$ systems described in literature:^{2, 7} in systems with the highest relative amount of complex **A** higher TOF numbers were obtained for the oxidation reactions. At higher $\text{Cu}^{2+}/\text{His}$ loadings pore-blocking and the co-formation of complex **B** will result in a lower TOF, but nevertheless it is evident from the data presented here, that the TOF will increase when Cu^{2+} can be reduced more easily in the catalytic cycle.

6.4.2 Structure of the complexes

Structural information on the $\text{Cu}^{2+}/\text{His}$ complexes that are encaged in the zeolite pores is primarily extracted from the UV/Vis/NIR, ESR and EXAFS spectra. All techniques show changes in the spectral data upon increasing the $\text{Cu}^{2+}/\text{His}$ concentration of the ion exchange solution. This implies that the coordination around the central Cu^{2+} ion changes and hence more than one type of $\text{Cu}^{2+}/\text{His}$ complex is immobilized. As shown in Figures 4 and 5, the ESR spectra clearly reveal the presence of two $\text{Cu}^{2+}/\text{His}$ complexes, **A** and **B**, of which **A** is the dominant one at low $\text{Cu}^{2+}/\text{His}$ concentrations and **B** is the major species with high $\text{Cu}^{2+}/\text{His}$ concentrations. Furthermore, the hyperfine splitting patterns point to two nitrogen atoms in the first coordination sphere in complex **A** and three in complex **B**. These observations are identical to the results of Goldfarb *et al.*,^{3, 6} who proposed the geometrical structures of **A** and **B** depicted in Figure 12.

In line with these results, the combined interpretation of our UV/Vis/NIR and EXAFS data confirm the larger number of coordinating nitrogen atoms upon increasing the $\text{Cu}^{2+}/\text{His}$ concentration. Figure 2 shows that the d-d transition band shifts to higher energy on going from sample **a** to **d**, *i.e.* from mainly complex **A** to mainly complex **B**. As EXAFS analysis reveals that the distance of the atoms in the first coordination sphere around the Cu^{2+} cation is the same for all samples, the UV/Vis d-d band shift must be due to a larger ligand field splitting between the d-orbitals of the Cu^{2+} complex and this finding can only be attributed to an increase in the amount of nitrogen atoms coordinating to the Cu^{2+} cation.

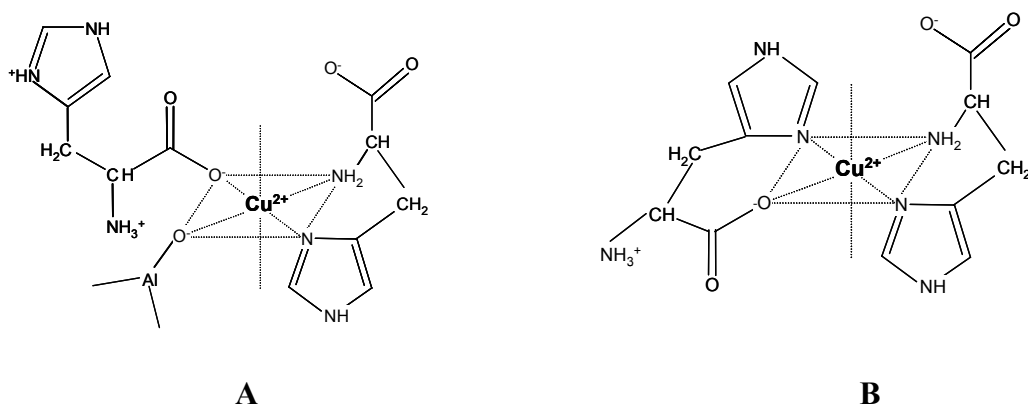


Figure 12. Structures of Cu²⁺/His complexes **A** and **B** immobilized in zeolite Y, proposed by Goldfarb *et al.*^{3,6}

The UV/Vis/NIR, ESR and EXAFS results of the Cu²⁺/His/DAY samples **e** and **f** confirm the observation by Grommen *et al.*,⁶ that the formation of complex **A** is related to the presence of aluminum in the zeolite matrix. The ESR parameters $g_{//}$ and $A_{//}$ of these samples are identical to the values of the Cu²⁺/His/Y samples (see Table 1) and in sample **e** complex **A** is the dominating species (see Table 1). Nevertheless, despite the high Cu²⁺/His concentration in the ion exchange solution for sample **f**, only a small fraction of the Cu²⁺/His complexes is exchanged on the zeolite material. Complex **B** is the major component in this material, probably due to the lack of aluminum atoms in the support (Note that the Cu²⁺ concentration in this sample is even lower than that of the Cu²⁺/His/Y sample **a**, in which complex **A** is the most abundant structure). This implies that the relative amount of the guest species **A** and **B** can also be varied by changing the aluminum content of the zeolite host material.

Additional structural information about the complexes can be derived from the UV/Vis/NIR spectrum, as coordination of an imidazole group to Cu²⁺ is known to give rise to a characteristic band pattern.⁸⁻¹² This type of absorption originates from ligand-to-metal charge transfer (LMCT) transitions of the higher lying orbitals of the imidazole ring to the Cu²⁺ cation. Next to a σ -lone pair there are two filled π -type orbitals on the imidazole ring that are high in energy¹² and as a consequence, three LMCT transitions from these orbitals to the empty $\sigma^*(x^2-y^2)$ orbital on the Cu²⁺ cation can occur. The transition from the lone pair is the highest in energy and its intensity is independent on the orientation of the imidazole ring with respect to the Cu²⁺ cation.⁸ This LMCT transition is known to absorb around 46000 cm⁻¹ and, as can be seen from Figure 2, a band at this position is indeed present in the spectra of all

samples. It follows that at least one imidazole group coordinates to Cu^{2+} both in complex **A** and in complex **B**. The other two LMCT transitions are lower in energy¹² and the position and intensity of the corresponding bands are less well-defined, as they depend on the orientation of the imidazole ring to the Cu^{2+} cation.⁸ These transitions can be assigned to the bands at 40000 cm^{-1} and 36000 cm^{-1} respectively. As can be seen from Figure 2, the spectral pattern changes with the Cu^{2+} /His loading. The band at 36000 cm^{-1} is strongest for the low-loaded sample **a**, whereas the band at 40000 cm^{-1} is most intense for the high-loaded sample **d**. This confirms not only the presence of two different complexes, **A** and **B**, but it also implicitly proves that the structure of these complexes differs in the orientation to Cu^{2+} via the imidazole ring of at least one of the two His ligands.

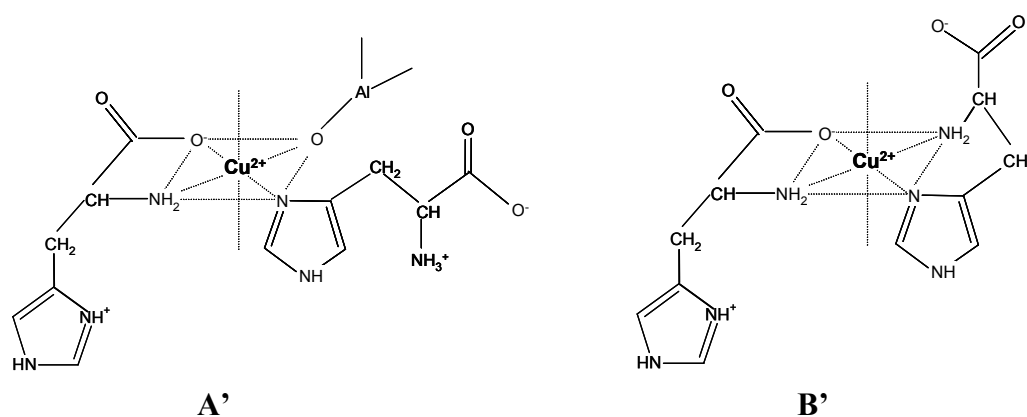


Figure 13. Proposed refined structures of Cu^{2+} /His complexes **A'** and **B'** immobilized in zeolite Y.

Summarizing these results, we conclude that the coordination around Cu^{2+} is NONO in complex **A** and NNNO in complex **B**, which is in accordance with the results of Goldfarb *et al.*^{3, 6} Although the authors have indications from ESEEM measurements that the two His ligands in complex **B** coordinate via N_{im} , it can be argued that their proposed geometrical orientations are not fully correct. Firstly, as follows from the IR and Raman spectra, the “pH” inside the zeolite is around 5 and, as we demonstrated in Chapter 4, a bis-glycine-like NONO coordination and a combined glycine/histamine-like NNNO chelation is much more likely under these circumstances. Secondly, the 7-membered ring coordination ($\text{N}_{\text{im}}, \text{O}_{\text{c}}$) of structure **B** (Figure 12) is not very plausible as it is associated with a considerable ring tension regarding the $\text{N}\dots\text{O}$ distance in this structure. The presence of a 7-membered ring should have affected the EXAFS data in a similar way as observed for the Cu^{2+} /His complexes in aqueous

solution, with axial coordination of the carboxyl groups, as presented in Chapter 4. However, the EXAFS data show no differences and for that reason we propose structures **A'** and **B'** in Figure 13 as refined alternatives for the complexes **A** and **B** presented by Goldfarb *et al.*^{3,6}

6.4.3 Formation of the complexes

Based on the preceding results we developed the following mechanism for the formation of the Cu²⁺/His complexes **A'** and **B'**. At the start of the ion exchange process the pH is 7.3 and Cu²⁺ will be mainly present as a complex with two His ligands that both coordinate histamine-like (NNNN), as described in Chapter 4. The charge of this complex will be neutral, whereas the excess of free His ligands will be charged partly neutral (H₂His⁰) and partly positive H₃His⁺. First, the H₃His⁺ ions will exchange with protons and sodium atoms in the zeolite framework, thus compensating for the charge deficiency on the aluminum atoms in the zeolite framework. This process is accompanied by a decrease of the “pH” in the zeolite and as a result not only the amount of H₃His⁺ will increase, but also the NNNN coordination of Cu²⁺/His inside the zeolite will convert to NNNO while the charge becomes 1⁺. Consequently, this complex can exchange with the sodium atoms too, which results in the possibility of anchoring the complex on Brønsted acid sites in the zeolite material. In our opinion, this is the principle of the formation of complex **A'**, although we do not yet understand the driving forces behind this process. Probably, the anchoring of the complex induces changes in the pK_a values of the different functional groups, similar to what we observed for the Cu²⁺/His complexes in Chapter 4.

By the time most Brønsted acid sites in the outer supercages of the support are occupied the only place left to accommodate Cu²⁺/His complexes is in the middle of the supercages. Meanwhile, the intra-zeolitic “pH” has decreased to a value of about 5 and most of the Cu²⁺/His complexes will be converted to the Him/Gly structure of complex **B'**. Occupation of this complex in the middle of the supercages is then very likely and this explains why no copper-aluminum interaction is found for this complex. In principle, a position between two supercages is also possible, but this is rejected for the same reason, since this would result in the observation of an Cu/Al interaction. The lack of available occupation sites in the vicinity

of Al atoms also explains why the absolute amount of complex **A'** is constant at high concentrations, whereas the amount of complex **B'** is still increasing.

6.5 Conclusions

The combined use of UV/Vis/NIR, ESR and X-ray absorption analysis has proven to be a powerful method to obtain complementary information on the structure of Cu^{2+} /His complexes immobilized in the supercages of the zeolitic supports Y and DAY. It is concluded that two complexes (**A'** and **B'**) are formed, with two His ligands coordinating to the central Cu^{2+} ion. The molecular structure of these two zeolite-immobilized Cu^{2+} /His complexes is different from the molecular structure of the Cu^{2+} /His complexes that are present in the aqueous ion exchange solution at pH = 7.3 (species **g** and **h**, Chapter 4). In complex **A'** one His molecule coordinates in a glycine-like chelation *via* N_{am} and O_{c} and the other one *via* the imidazole ring (N_{im}) only. The remaining equatorial position anchors the complex to the support *via* an oxygen atom that is connected to an aluminum atom in the framework. In complex **B'** one His ligand coordinates in a histamine-like chelation (N_{am} , N_{im}) and the other one in a glycine-like coordination (N_{am} , O_{c}). It resembles mostly species **f** of Chapter 4. The absolute and relative abundance of both complexes depends on the Cu^{2+} /His concentration of the ion exchange solution and on the amount of available Brønsted acid sites in the zeolite support. Complex **A'** is the major species being formed as long as Brønsted acid sites are available for ion exchange. As a consequence, complex **B'** becomes the prevailing component at high Cu^{2+} /His concentrations and in case the Si/Al ratio of the zeolite is high. XRF analysis indicates that pore blocking occurs at high concentrations. As a result, the number of immobilized complexes is not proportional to the Cu^{2+} /His concentration in the ion exchange solutions. IR and Raman spectroscopy are not sensitive enough to obtain structural information on the complexes. Yet, the data are useful to determine a “pH” value of 5 within the pore system of the zeolite matrix.

The geometrical structure of complex **A'** differs from the preferred Cu^{2+} /His complex geometry in aqueous solution at pH = 5. It implies that the zeolite host material is able to affect the coordination and orientation of guest molecules and illustrates that zeolite supports are not just inorganic supports that can be used for site isolation and shape selectivity. On the contrary, the zeolite host material actively participates in the coordination chemistry of the

guest complex and affects the chemistry of the guest complexes by imposing a different chemical environment than in *e.g.* aqueous solution. This is illustrated by the increased reducibility of the Cu²⁺/His complexes in the zeolite material upon exposure to X-ray radiation. Apparently, the zeolite host material increases the reduction potential of the anchored guest complex **A'**. Complex **B'**, which has a counterpart in aqueous solution, is not reduced. For aqueous Cu²⁺/His solutions no reduction was observed under the same X-ray photon flux.

These results illustrate how the immobilization of transition metal ion complexes in inorganic support materials may open new perspectives for the design of new catalyst materials with novel applications.

Acknowledgements

John Raaymakers[†] and Ad Mens are thanked for performing N₂ physisorption measurements and Ad van der Eerden is thanked for XRF measurements. Ernst van Faassen is thanked for the use of the ESR spectrometer and for help during the interpretation of the ESR results. Robert Schoonheydt is thanked for the use of the ESR spectrometer in Leuven. The European Synchrotron Radiation Facility (ESRF, Grenoble, France) and Hasylab (Hamburg, Germany) are acknowledged for the provision of synchrotron radiation facilities. We thank M. Borowski (BM29) and W. Bras and S. Nikitenko of DUBBLE (BM26A, ESRF) for their help and discussion during the experiments. NWO/CW - Van der Leeuw and the National Research School Combination – Catalysis (NRSC-C) are acknowledged for financial support.

References

- [1] R. J. Sundberg and R. B. Martin, *Chem. Rev.* **74** (1974)
- [2] B. M. Weckhuysen, A. A. Verberckmoes, I. P. Vannijvel, J. A. Pelgrims, P. L. Buskens, P. A. Jacobs and R. A. Schoonheydt, *Angew. Chem. Int. Ed. Engl.* **34** (1995) 2652.
- [3] D. Baute, D. Arieli, F. Neesse, H. Zimmermann, B. M. Weckhuysen and D. Goldfarb, *J. Am. Chem. Soc.* **126** (2004) 11733.
- [4] D. E. de Vos, P. P. Knops-Gerrits, R. F. Parton, B. M. Weckhuysen, P. A. Jacobs and R. A. Schoonheydt, *J. Inclus. Phen. Molec. Recogn. Chem.* **21** (1995) 185.

- [5] L. Fu, B. M. Weckhuysen, A. A. Verberckmoes and R. A. Schoonheydt, *Clay Minerals* **31** (1996) 491.
- [6] R. Grommen, P. Manikandan, Y. Gao, T. Shane, J. J. Shane, R. A. Schoonheydt, B. M. Weckhuysen and D. Goldfarb, *J. Am. Chem. Soc.* **122** (2000) 11488.
- [7] B. M. Weckhuysen, A. A. Verberckmoes, L. Fu and R. A. Schoonheydt, *J. Phys. Chem.* **100** (1996) 9456.
- [8] A. B. P. Lever, *Inorganic Electronic Spectroscopy*, Elsevier Science BV, Amsterdam, 1984.
- [9] E. W. Wilson, M. H. Kasperian and R. B. Martin, *J. Am. Chem. Soc.* **92** (1970) 5364.
- [10] E. Bernarducci, W. F. Schwindinger, J. L. Hughey, K. Krogh-Jespersen and H. J. Schugar, *J. Am. Chem. Soc.* **103** (1981) 1668.
- [11] E. Bernarducci, P. K. Bharadwaj, K. Krogh-Jespersen and H. J. Schugar, *J. Am. Chem. Soc.* **105** (1983) 3860.
- [12] T. G. Fawcett, E. E. Bernarducci, K. Krogh-Jespersen and H. J. Schugar, *J. Am. Chem. Soc.* **102** (1980) 2598.

Chapter 7

Summary and Concluding Remarks

The high activity and selectivity of enzymes have inspired many scientists to study the structure and working mechanism of bio-molecular complexes. Also in the catalysis community this subject is of topical interest, as it may provide inspiration for the development of a new generation of bio-inspired catalyst materials. Functionalization of inorganic substrates, such as zeolites, with transition metal ion (TMI) complexes offers the possibility to design new materials with a high potential to serve as working enzyme mimics. An essential step for the further development of these kinds of materials is obtaining fundamental knowledge of the chemistry involved in the making of these mimics and an understanding of the factors that influence the molecular structure of the resulting materials.

These challenging objectives have been the main goal of the research described in this thesis. To this end complexes of Histidine (His) coordinated to Cu^{2+} have been selected as model TMI-complexes for introduction into the pore system of zeolite Y and to serve as a mimic for the active site of the enzyme galactose oxidase. In order to understand and describe the host-guest chemistry of these complexes in the pores of zeolite Y and to make the analogy with enzymatic systems a detailed study of the His ligand was conducted first. As a logical next step the coordination and geometrical structure of the

Cu²⁺/His complexes in aqueous environment was studied, followed by the characterization of the complexes after immobilization in the inorganic zeolite matrix.

A large set of accurate chemical and physical data is inevitable to (1) establish the coordination geometry of the TMI-complexes before and after immobilization and (2) to understand the chemistry of the guest complexes within the pores of the zeolite host material. For the collection of these data a diversity of characterization methods has been used, either as stand-alone techniques or in an integrated set-up. Next to X-ray fluorescence spectroscopy (to determine the metal content of the samples) and N₂-physisorption (to establish the micropore volume of the zeolite), before and after encaging the TMI-complexes, IR, Raman, UV/Vis, ESR and EXAFS spectroscopy have been successfully applied to obtain the desired information. The advantages of combining different characterization techniques in one reaction set-up are well illustrated in **Chapter 2**. This chapter describes the results of the simultaneous *in-situ* monitoring of two Cu²⁺ complex catalyzed oxidation reactions, using UV-Vis and ED-XAFS spectroscopy as the analytical tools. Two complexes have been studied, *viz.* Cu²⁺/bipyridine and a Cu²⁺/1,10-phenantroline and combined interpretation of the data revealed unambiguously that the X-ray beam can reduce the Cu²⁺ ion during the reaction. It was concluded that the degree of radiation damage not only depends on the intensity of the radiation and the exposure time, but also on the type of counter anion that is present in the solution. It follows that, next to complementary and confirmational purposes, the use of a second technique can be a valuable tool to quantify detrimental side-effects of the first technique on the sample. Furthermore, it was found that exposure to an X-ray beam can result in a considerable increase of the temperature of the reaction mixture, which speeds up the occurrence of catalytic reactions in the cell during data acquisition. Although these results do not imply that X-ray absorption measurements are always prone to radiation damage, we have strong indications that it is an often underestimated phenomenon in literature. Especially when aqueous solutions are involved these phenomena may start to play a role. As a consequence, interpretations of *in-situ* XAFS data and related conclusions on the catalytic reaction cycle in aqueous solutions should be referred to only after critical evaluation.

Knowledge of the structural behavior of a ligand prior to coordination to a TMI-complex is very important to understand the coordination chemistry and to determine the

geometrical orientation of the ligands after complexation. These aspects have been described in **Chapter 3**. The complementary techniques IR and Raman spectroscopy have been used in parallel to study aqueous solutions of His over the pH range 0-14 with increments of 1 pH unit. This study provided a complete and complementary set of vibrational data that enabled us to determine all possible states of protonation of His, *i.e.* $\text{H}_4\text{His}^{2+}$, H_3His^+ , H_2His^0 , HHis^- and His^{2-} . Besides, series of IR and Raman bands have been established that are useful as markers to distinguish the N^π - and N^τ -protonated forms of H_2His^0 and HHis^- .

This information turned out to be crucial for the next step, which was the elucidation of the formation, coordination and geometrical orientation of $\text{Cu}^{2+}/\text{His}$ complexes in aqueous environment. This topic is described in **Chapter 4**. A multi-technique approach, combining IR, Raman, UV/Vis, EPR and EXAFS spectroscopy, was used to study pH-induced structural changes of the $\text{Cu}^{2+}/\text{His}$ complexes in aqueous solutions over the pH range 0 to 10. Integrated interpretation of the spectroscopic data revealed the formation of seven different complexes for which detailed geometrical structures have been established. At highly acidic conditions, Cu^{2+} and His are present as separated solvated ions, but at pH = 2 the carboxylic group deprotonates and starts to coordinate. Next, the bidentates $\text{Cu}^{2+}[\text{H}_2\text{His}^0(\text{O}_c, \text{N}_{\text{am}})]$ and $\text{Cu}^{2+}[\text{H}_2\text{His}^0(\text{O}_c, \text{N}_{\text{am}})]_2$ are formed, of which the latter is the main component at pH = 3.5. Concomitantly, the formation of the mixed bi- and tridentate complexes $\text{Cu}^{2+}[\text{H}_2\text{His}^0(\text{O}_c, \text{N}_{\text{am}})] [\text{HHis}^-(\text{O}_c, \text{N}_{\text{am}}, \text{N}_{\text{im}})]$ and $\text{Cu}^{2+}[\text{HHis}^-(\text{N}_{\text{am}}, \text{N}_{\text{im}})][\text{HHis}^-(\text{O}_c, \text{N}_{\text{am}}, \text{N}_{\text{im}})]$ begins at pH = 3 and it is concluded that in these complexes coordination of the imidazole ring occurs mainly *via* the N^τ atom. These species become the major components at pH = 5, but at pH > 7 they rapidly convert to the bi-ligand tridentate complex $\text{Cu}^{2+}[\text{HHis}^-(\text{O}_c, \text{N}_{\text{am}}, \text{N}_{\text{im}})]_2$ with four nitrogen atoms coordinated in the equatorial plane and the carboxylic oxygen atoms in axial position. This complex decomposes at pH > 10. As a result of this study the mechanism that drives the coordination and complex formation of the $\text{Cu}^{2+}/\text{His}$ system has been largely unravelled. Furthermore, it enabled us to confirm, clarify or correct several structural proposals in literature.

In continuation to this study, the molecular structure of the $\text{Cu}^{2+}/\text{His}$ complexes in aqueous solution was studied by detailed analysis of the X-ray absorption near edge structure (XANES) of the X-ray absorption spectra in combination with simultaneously

recorded UV/Vis data. The results of this research have been outlined in **Chapter 5**. By monitoring the changes in the XANES as a function of the pH information on the coordination geometry of the Cu^{2+} /His complexes was obtained. This was in line with the conclusions from Chapter 4. The results also confirmed the reducing effect of the X-ray beam, as already described in Chapter 2. Reduction appeared to be dependent on the pH of the solution. Combining these observations with the geometrical structures of the Cu^{2+} /His complexes at various pH values, as determined in Chapter 4, lead to the conclusion that coordination of the imidazole ring of histidine in the equatorial plane promotes the reduction of Cu^{2+} to Cu^{1+} .

The characterization of Cu^{2+} /His complexes after immobilization in the pore system of zeolite Y was the last step in our three-step approach. **Chapter 6** elaborates on the molecular structure of Cu^{2+} /His complexes after encaging in zeolite Y and dealuminated zeolite Y (DAY). Multi-technique analyses of the Cu^{2+} /His/Y and Cu^{2+} /His/DAY samples by means of UV/Vis/NIR, ESR and EXAFS spectroscopy reveal the presence of two complexes **A'** and **B'**, of which the absolute and relative abundance depends on the concentration of the Cu^{2+} /His complex in the solution used for ion exchange. IR and Raman spectroscopy showed too less sensitivity to yield structural information on the complexes, but the spectral patterns revealed that the “pH” within the zeolite pores is around 5. This finding reveals that the glycine- (N_{am} , O_{c}) and histamine (N_{am} , N_{im})-like chelation, as determined for complex **B'**, is identical to the structure of the free Cu^{2+} /His complex in aqueous solution at the same pH. Complex **A'** is found to be anchored to an oxygen atom of the support and its geometrical structure differs from any of the preferred structures of Cu^{2+} /His complexes in aqueous solution. For that reason, it is concluded that the zeolite host material is able to affect the coordination and orientation of guest molecules.

Summarizing the results of this thesis, the following conclusions can be drawn:

- The multiple spectroscopic techniques approach is highly beneficial for unambiguously elucidating the molecular structure of TMI-complexes in great detail, in solution as well as inside a zeolite support. Moreover, it offers valuable

complementary information when applied in parallel to the same chemical system. An additional advantage is that it may reveal unexpected side-effects caused by one of the characterization techniques involved. As such, the application of a combination of spectroscopic techniques is inevitable to determine and develop essential structural similarities between man-made catalysts and natural enzymes.

- Inorganic microporous substrates, such as zeolite Y, can be functionalized successfully by encaging complexes of transition metal ions with organic ligands *via* the method of ion exchange. The immobilization process is not only driven by the chemical properties of the guest complex, but the zeolite host material also actively participates in the coordination chemistry of the complex. As a side-effect guest molecules are able to influence the chemical environment within the pores of the zeolite host material.
- Zeolite supports can be used to stabilize Cu^{2+} /His complexes in two different coordination geometries, neither one of them identical to the complexes present in the initial exchange solution. The first one is very similar to the complex in aqueous environment at $\text{pH} = 5$. In the second one the zeolite support is involved in the coordination, *i.e.* the zeolite material acts as a monodentate ligand. This complex can be envisaged as a structural mimic of galactose oxidase, since it has a very similar first coordination environment around the Cu^{2+} cation. The parameters that can be used to favor entrapment of one of these structures inside the zeolite are the concentration of the TMI-complex in the ion exchange solution and the silica/alumina ratio of the support.
- Synchrotron radiation effects can be used to evaluate the redox potential of metal complexes in solutions and solids if water is present. More specifically, from X-ray absorption characterization it was found that the redox potential of the Cu^{2+} /His-complex, in which the zeolite is serving as a monodentate ligand, is increased. Therefore, it is anticipated that the redox properties of TMI-complexes can be tuned by a deliberate choice of the support material. The chemical composition of the support oxide will affect the redox properties of the encaged metal complexes.

Based on the information on host-guest chemistry of TMI-complexes in microporous materials, presented in this thesis, we believe that the development of new hybrid materials with potential applications in both catalysis and sensing is within reach. Future efforts should be directed at the immobilization of di-nuclear metal complexes as well as the use of biologically relevant ligands containing different coordinating atoms, such as S. Moreover, the influence the support composition and porosity on the resulting hybrid materials should be evaluated as well.

Samenvatting

Enzymen zijn de katalysatoren van de natuur. Ze staan bekend om hun hoge activiteit, efficiëntie en selectiviteit. Dit maakt het interessant om ze te gebruiken voor industriële toepassingen. Het is echter erg moeilijk om enzymen op grote schaal toe te passen in de industrie, aangezien het fragiele moleculen zijn die vaak niet bestand zijn tegen de extreme omstandigheden die toegepast worden in de industrie. Een manier om dit probleem op te lossen is door het maken van een meer robuuste, synthetisch analoog van het enzym (een zgn. “mimic”), waarbij alleen het belangrijkste onderdeel van het enzym (het actieve centrum) wordt nagebouwd. Bij dit nabootsen wordt zoveel mogelijk gebruik gemaakt van dezelfde bouwstenen als in het actieve centrum van het enzym en wordt getracht een omgeving te creëren die vergelijkbaar is aan die van het enzym.

Tijdens het onderzoek, beschreven in dit proefschrift, werd een structurele mimic gemaakt van het actieve centrum van het enzym Galactose Oxidase. Dit enzym is actief in de oxidatie van organische moleculen met moleculaire zuurstof. Het actieve centrum bestaat uit een koperion dat is omringd door o.a. twee histidine moleculen (die aan het koperion coördineren via een stikstofatoom). Voor het maken van de enzym-mimic werden ook koper en histidine als bouwstenen gebruikt. Koper-histidine complexen werden geïmmobiliseerd in de poriën van zeoliet Y via een ionenuitwisselingsreactie. De zeolietmatrix wordt gebruikt om bepaalde vormen van het koper-histidine complex te stabiliseren en om vorm-selectiviteit in de enzym-mimic te introduceren. Om de moleculaire structuur van de mimic te bepalen en om de invloed van de zeolietmatrix op de moleculaire structuur van het koper-histidine complex te kunnen definiëren, werd er gebruik gemaakt van een combinatie van verschillende spectroscopische karakteriseringstechnieken. Complicerende factor hierbij was dat elke techniek andere condities vereist om optimale resultaten te behalen.

Een belangrijk uitgangspunt van het onderzoek was uit te vinden wat de invloed van de zeoliet op de moleculaire structuur van het koper-histidine complex was en hoe deze invloed zich vertaalt in uiteindelijke toepassing van de mimic. Om een goede beschrijving van de moleculaire structuur van de enzym-mimic te kunnen geven, werd het probleem in een aantal deelstappen benaderd. Allereerst werd de structuurverandering van het histidine molecuul bestudeerd in oplossingen met een verschillende zuurgraad. De kennis die hiermee werd opgedaan, werd vervolgens toegepast in de volgende stap: het ophelderen van de moleculaire structuur van een met koper gecomplexeerd histidine complex als functie van de pH in waterige oplossingen. In de laatste stap werd het koper-histidine complex geïmmobiliseerd in zeoliet Y, waarna de moleculaire structuur van de uiteindelijke mimic werd bestudeerd.

In hoofdstuk 2 is beschreven hoe twee verschillende spectroscopische karakteriseringstechnieken (UV-Vis en ED-XAFS), gecombineerd in één experimentele opstelling, kunnen worden gebruikt om de koper-bipyridine gekatalyzeerde oxidatie van benzylalcohol te bestuderen. Naast complementaire chemische informatie over het mechanisme van de reactie werd met de ene techniek (UV-Vis) aangetoond dat de andere techniek (ED-XAFS) onder meer een reducerende invloed heeft op het systeem dat wordt bestudeerd. Dit resultaat is van belang voor het onderzoek dat beschreven wordt in de verdere hoofdstukken van dit proefschrift.

Hoofdstuk 3 beschrijft de resultaten van het onderzoek naar de structuur van één van de bouwstenen van de mimic, het histidine molecuul, als functie van de zuurgraad van een waterige oplossing. Daarvoor werd een combinatie van infrarood- (IR) en Raman-spectroscopie gebruikt. De (absorptie)banden, karakteristiek voor het histidine ligand, werden in kaart gebracht om de karakterisering van het koper-histidine complex in de volgende stappen te vereenvoudigen.

Vervolgens werd in de hoofdstukken 4 en 5 de moleculaire structuur van het koper-histidine complex (dat resulteert bij een combinatie in waterig milieu van histidine moleculen met een tweede bouwsteen van de mimic, een koper ion) in water bestudeerd en opgehelderd met een combinatie van verschillende karakteriseringstechnieken (UV-Vis, ESR, ED-XAFS, IR en Raman spectroscopie). De structuur van het complex is sterk afhankelijk van de pH van de oplossing waarin het complex zich bevindt. Aangezien histidine met vier verschillende

functionele groepen aan het koperion kan coördineren en in elk koper-histidine complex twee histidine liganden tegelijkertijd kunnen coördineren, zijn er veel verschillende conformaties van het koper-histidine complex mogelijk. In totaal werd de structuur van 7 verschillende koper complexen opgehelderd, afhankelijk van de pH van de oplossing. Ook in deze stap van het onderzoek werd een reducerende invloed van de XAFS-techniek op het systeem geconstateerd, hoewel alleen bij gebruik van hoge intensiteit Röntgenstraling. De mate van reductie is afhankelijk van zowel de pH van de oplossing als van de moleculaire structuur van het koper-histidine complex.

In hoofdstuk 6 werd de moleculaire structuur van het koper-histidine complex na immobilisatie in de poriestructuur van zeoliet Y bestudeerd. De aanwezigheid van twee verschillende koper-histidine in de zeoliet werd aangetoond, waarbij de relatieve verhouding van de twee complexen een functie blijkt te zijn van de koperconcentratie in de ionen uitwisselingsoplossing en de silicium/aluminium (Si/Al) verhouding van de zeoliet. Het eerste complex (complex A) is voornamelijk aanwezig bij lage koper concentraties en bij een lage Si/Al ratio, terwijl de relatieve hoeveelheid van het tweede complex (complex B) groter wordt bij hogere koper concentraties en een hogere Si/Al ratio. In complex A is er een directe interactie tussen de structuur van de zeoliet en het koper-histidine complex. In complex B is deze interactie niet aanwezig. De moleculaire structuur van dit complex komt overeen met de moleculaire structuur van het koper-histidine complex dat aanwezig is in waterig milieu bij pH = 5. Tijdens het bestuderen van de mimic met behulp van XAFS-spectroscopie trad alleen bij complex A een reductie op, hetgeen aangeeft dat complex A een hogere reductiepotentiaal (vs. SHE) heeft dan complex B. De structuur van complex A vertoont ook de meeste overeenkomst met de structuur van het actieve centrum van het enzym Galactose Oxidase. Aangezien de zeolietstructuur actief deelneemt aan de coördinatiechemie van complex A, zou de reductiegevoeligheid van complex A beïnvloed kunnen worden door de elektronische eigenschappen van het dragermateriaal te wijzigen en op deze manier de eigenschappen van de katalysator te beïnvloeden.

In het werk beschreven in dit proefschrift wordt aangetoond dat het mogelijk is om een structurele mimic te maken van het enzym Galactose Oxidase. Door in verschillende stappen diverse complementaire spectroscopische karakteriseringstechnieken toe te passen, was het mogelijk om de processen die een rol spelen in het vormingsmechanisme van de

mimic te beschrijven. Tevens leverden deze technieken een schat aan informatie op over de vele verschillende structuren die koper-histidine complexen kunnen aannemen, zowel in waterige oplossing als geïmmobiliseerd in zeoliet Y. Een voordeel van het gelijktijdig toepassen van meerdere technieken was dat één techniek kon worden gebruikt om de invloed van een andere techniek op het systeem te bestuderen. De resultaten laten zien dat het mogelijk is om natuurlijke de katalysatoren na te bootsen voor allerlei (nieuwe) toepassingen.

List of publications

D.J. Lensveld, J.G. Mesu, A.J. van Dillen and K.P. de Jong, *Synthesis and characterisation of MCM-41 supported nickel oxide catalysts*, *Microporous and Mesoporous Materials* **44-45** (2001) 401-407.

J.G. Mesu, A.M.J. van der Eerden, F.M.F. de Groot and B.M. Weckhuysen, *Synchrotron radiation effects on catalytic systems as probed with a combined UV-Vis/XAFS spectroscopic set-up*, *Journal of Physical Chemistry B* **109** (2005) 4042-4047.

J.G. Mesu, T. Visser, F. Soulimani en B.M. Weckhuysen, *Infrared and Raman spectroscopic study of pH-induced structural changes of copper histidine complexes in aqueous environment*, *Vibrational Spectroscopy*, in press.

K. Kervinen, H. Korpi, J.G. Mesu, F. Soulimani, T. Repo, B. Rieger, M. Leskelä and B.M. Weckhuysen, *Mechanistic insights into the oxidation of veratryl alcohol with Co(salen) and oxygen in aqueous media: an in-situ spectroscopic study*, *European Journal of Inorganic Chemistry*, in press.

S.J. Tinnemans, J.G. Mesu, K. Kervinen, T. Visser, T.A. Nijhuis, A. Beale, A.M.J. van der Eerden and B.M. Weckhuysen, *Combining operando techniques in one spectroscopic-reaction cell: new opportunities for elucidating the active site and related reaction mechanism in catalysis*, submitted.

J.G. Mesu, A.F. Vanin, B.M. Weckhuysen and E.E. van Faassen, *Zeolite-based sensor for nitric oxide dosimetry in biological systems*, submitted.

J.G. Mesu, T. Visser, F. Soulimani, A.M. Beale, E.E. van Faassen and B.M. Weckhuysen, *On the coordination chemistry and molecular structure of copper(II) histidine complexes in aqueous solutions*, in preparation.

J.G. Mesu, T. Visser, F. Soulimani, A.M. Beale and B.M. Weckhuysen, *Zeolite-encaged copper(II)-histidine complexes as structural mimic of Galactose Oxidase*, in preparation

Conference proceedings

J.G. Mesu, D. Baute, H.J. Tromp, E.E. van Faassen and B.M. Weckhuysen, *Synthesis and characterization of zeolite encaged enzyme-mimetic copper histidine complexes*, *Studies in Surface Science and Catalysis* **143** (2002) 287-293.

D.J. Lensveld, J.G. Mesu, A.J. van Dillen and K.P. de Jong, *The application of well-dispersed nickel nanoparticles inside the mesopores of MCM-41 by use of a nickel citrate chelate as precursor*, *Studies in Surface Science and Catalysis* **143** (2002) 647-657.

J.G. Mesu, D. Baute, H.J. Tromp, E.E. van Faassen and B.M. Weckhuysen, *Incorporation of copper histidine complexes into a zeolite Y matrix*, *Series Chemistry* **12** (2003) 417-422.

Dankwoord

Promoveren doe je niet alleen. Newton heeft eens gezegd: “Dat ik zo ver heb kunnen zien komt, omdat ik op de rug van reuzen heb gestaan”. Met het aanhalen van dit citaat wil ik absoluut niet pretenderen dat ik de visie van Newton heb. Ik wil alleen aangeven dat ik in de afgelopen jaren heb mogen steunen op de sterke schouders van een aantal onmisbare helpers, die ik bij deze wil bedanken.

Ik wil beginnen bij mijn promotor, Prof. Bert Weckhuysen. Bert, ik wil je van harte bedanken voor je enthousiasme en het in mij gestelde vertrouwen, door één van je “wetenschappelijke baby’s” aan mij toe te vertrouwen. Ik ben je zeer erkentelijk voor de vrijheden die je mij hebt gegeven bij de uitvoering van het onderzoek. Ik heb daar uiteindelijk, op verschillende gebieden, heel veel van geleerd. We hebben allebei de afgelopen jaren een hoop leuke, maar ook een aantal heel verdrietige dingen meegemaakt. Ik kon altijd bij je binnen lopen voor een gesprek. Je maakte altijd tijd voor me, ook toen de groep in de loop van de tijd steeds groter en groter werd. Bedankt daarvoor! Op deze plek wil ik ook Marjolein bedanken voor het feit dat zij de afgelopen maanden Bert met mij heeft willen delen. Ik hoop dat jullie samen heel gelukkig worden!

Dan kom ik bij een andere reus, mijn co-promotor Tom. Zonder jouw sterke schouders zou er op 30 mei geen promotie zijn geweest. Je bent met name in het afgelopen half jaar mijn rots in de branding geweest (en die branding was voor mij op sommige momenten zéér heftig!). Heel veel bedankt voor je steun en je relativiserende woorden. Het is er in de afgelopen maanden niet van gekomen, maar als het seizoen er weer is, zal ik je een keer opbellen om naar de Oosterschelde te gaan!

Mijn speciale dank gaat ook uit naar reus Fouad. Bedankt voor je hulp met het doen van de vele IR en Raman metingen. Ik moet toch eerlijk toegeven dat jij een stuk aangenamer gezelschap bent in de meetkamer dan de Ethiopische en Soedanese hitlijsten! Ik hoop dat je nog een laatste jump kunt maken in de Topcoach!

De afgelopen jaren heb ik met heel veel plezier doorgebracht op de vakgroep Anorganische Chemie en Katalyse. Ik wil de mensen van de staf, vooral Diek, Krijn, Frank, Harry en Jos, bedanken voor hun steun in de afgelopen jaren. Ik kon altijd bij jullie terecht voor discussie en met allerlei vragen. Alle (oud) collega's wil ik bedanken voor al de gezelligheid tijdens de koffiepauzes, BBQ's, LIIT's (bestaan ze nog?), (kerst)diners, squashwedstrijden, borrels en alle andere activiteiten. Dymph, Monique, Thea, Fred, Ad M, Ad E, Vincent, Marjan en Hans wil ik bedanken voor hun ondersteuning en voor het doen van metingen. Ook de studenten Henk Jan, Ruud, Dick, Hanneke en Timmo wil ik bedanken voor hun bijdrage in de vorm van praktisch werk, discussies en scripties.

Ook XAFS-metingen doe je niet alleen. In het bijzonder wil ik reus Adje bedanken voor alle steun, de afgelopen jaren door. Ik zal nooit vergeten hoe we binnen een uur de Chamrousse zijn opgerend; ik zal onze nachtelijke conversaties bij het guesthouse nog gaan missen! I also want to thank Kaisa and Andy for their help and discussion during the experiments. I wish you both all the luck with your challenging projects! Ook Moniek, Michiel, Andrea, Laurens, Willem, Frank, Marije, Daphne, Yihua, Didier, Sylvia en Pieter wil ik heel hartelijk bedanken voor hun hulp en gezelligheid tijdens al de experimenten.

Ernst van Faassen ("the man with the hat", zoals Fernando hem altijd noemde) wil ik bedanken voor zijn bijdrage in het ESR-werk en voor het mij bekend maken met de wereld van de NO-chemie. I also want to thank Albert, Anatoly, Natasha and Liliana for the nice cooperation. Ook de mensen van de werkplaats (met name Evert), van de glasblazerij en van de AV-dienst wil ik bedanken voor hun onmisbare steun.

In het bijzonder wil ik mijn kamergenoten, Ferry en Fernando bedanken voor een heel erg leuke tijd. Met een grote glimlach denk ik terug aan de FIFA Z221 competitie: dat waren nog eens tijden! Ook jou Ferry, ouwe reus, wil ik bedanken voor je steun en vriendschap in de afgelopen jaren. Ik wens je veel succes bij het afronden van je eigen project en hoop dat we in de toekomst contact kunnen blijven houden. Ik ben blij dat je op 30 mei één van mijn paranimfen wilt zijn!

Aangezien ik voorlopig (wanneer ga jij promoveren, Karen?) de laatste schakel ben in de rij, wil ik de mede-Labtops (Ries, Jules, Karen, Dennis en Marjolein) laten weten dat ik al aan het uitkijken ben naar grotere behuizing om al de trofeeën op te kunnen slaan. Bedankt voor de leuke avonden, ik hoop dat we binnenkort weer eens wat kunnen organiseren!

Dan reus Dennis. Het begon allemaal zo'n 5½ jaar geleden met nikkel en MCM-41. Heel veel bedankt voor je steun en vriendschap in de afgelopen jaren. Ik bewaar goede herinneringen aan onze rondtrip door de USA. De foto op de cover is er daar één van. Ook bedankt voor al de tijd die je hebt gestoken in het doorlezen van dit manuscript!

Dirk, Gerdien, Daan, Jasper en nu ook Bas: Ik wil jullie heel hartelijk bedanken voor al de liefde en vriendschap die ik de afgelopen jaren van jullie heb mogen ontvangen! Ik ben erg blij dat jij, Dirk, als paranimf achter mij wilt staan op 30 mei!

Als laatste wil ik mijn naaste familie bedanken. Pa en Ma, Ricardo, Anja, Romy, Annerike en (bijna) Jan: bedankt voor jullie onvoorwaardelijke steun de afgelopen jaren door. Het is elke keer weer heerlijk om af te reizen naar het Zeeuwse. Ik hou van jullie!

Curriculum Vitae

Gerbrand Mesu werd geboren op 23 mei 1975 te Spakenburg. In 1993 behaalde hij het VWO diploma aan de Voetius Scholengemeenschap te Goes. In september van datzelfde jaar begon hij met de studie informatica aan de Universiteit Utrecht. Eind 1994 stapte hij over naar de studie scheikunde aan de Universiteit Utrecht. In maart 2001 studeerde hij af *met genoegen* met bijvakken bij de secties Anorganische Chemie en Katalyse en Theoretische Chemie en hoofdvak bij de sectie Anorganische Chemie en Katalyse in de groep van Prof. K.P. de Jong. Vanaf april 2001 was hij werkzaam als Assistent in Opleiding (AIO) bij de sectie Anorganische Chemie en Katalyse van de Universiteit Utrecht. Het onderzoek dat sinds die tijd werd uitgevoerd onder supervisie van Dr. T. Visser en Prof. B.M. Weckhuysen heeft geleid tot dit proefschrift.

